A Reduced-order Nonlinear Aeroelastic Framework for Wings Undergoing Large Deflections

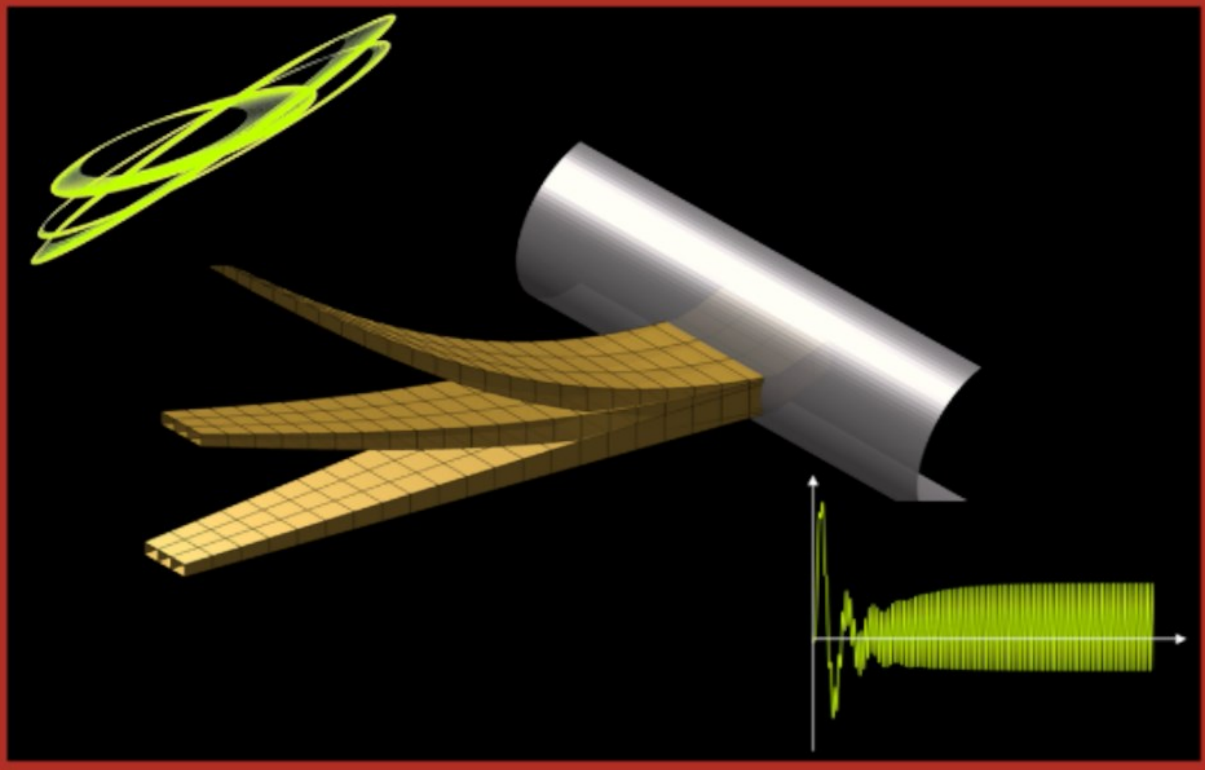

Kautuk Sinha

A REDUCED-ORDER NONLINEAR AEROELASTIC FRAMEWORK FOR WINGS UNDERGOING LARGE DEFLECTIONS

Kautuk SINHA

A REDUCED-ORDER NONLINEAR AEROELASTIC FRAMEWORK FOR WINGS UNDERGOING LARGE DEFLECTIONS

Dissertation

for the purpose of obtaining the degree of doctor
at Delft University of Technology
by the authority of the Rector Magnificus,
Prof. dr. ir. H. Bijl,
chair of the Board for Doctorates
to be defended publicly on
Thursday, 28 May 2026, 12:30 PM

by

Kautuk SINHA

This dissertation has been approved by the promotors.

Composition of the doctoral committee:

Rector Magnificus,	chairperson
Prof. dr. ir. Roeland De Breuker,	Delft University of Technology, promotor
Dr. F. Alijani,	Delft University of Technology, promotor

Independent Members:

Prof. dr. J.E. Cooper,	University of Bristol, UK
Prof. dr. ir. J.L. Herder,	Delft University of Technology
Prof. dr. ir. M. Langelaar,	Delft University of Technology
Dr. ir. P.R. Wellens,	Delft University of Technology
Dr. J.J.E. Teuwen,	Delft University of Technology, reserve member

Other Member:

Prof. Dr.-Ing. W.R. Krüger	Technical University of Berlin / DLR, Germany

This doctoral research was supported by the DLR-Institute of Aeroelasticity (Göttingen, Germany) and the Delft University of Technology (the Netherlands).

Keywords: Nonlinear aeroelasticity, reduced-order modelling, geometric nonlinearity, nonlinear dynamics, limit cycle oscillations

Printed by: Amazon Kindle Direct Publishing

Cover by: K. Sinha

ISBN 978-94-6384-963-0

An electronic version of this dissertation is available at https://repository.tudelft.nl/

Dedicated to my parents, Surabhi, Neha,

Priyanka and the little one

Table of Contents

Nomenclature

Abbreviations

AePW3	AIAA third aeroelastic prediction workshop
CFD	Computational fluid dynamics
DLM	Doublet lattice method
FE	Finite element
GEBT	Geometrically exact beam theory
IP	In-plane motion
K-N	Koiter-Newton method
LCO	Limit cycle oscillations
MRM	Modal rotation method
MD	Mode derivatives
NNM	Nonlinear normal modes
OOP	Out-of-plane motion
ODE	Ordinary differential equation
ROM	Reduced order model
SSM	Spectral sub-manifold approach
UVLM	Unsteady vortex lattice method
UDL	Uniformly distributed load
UK-N	Koiter-Newton method with ROM updating

Greek Symbols

α	Effective angle of attack
α_r	Root angle of attack
δ	Variational operator
$\delta_{k\alpha}$	Kronecker delta

ϵ	Element strain
θ	Pitch angle
θ_s	Twist in the structural coordinate system
$\dot{\theta}$	Pitch rate
λ_n	Induced flow states which are used to approximate the induced flow velocity
λ_0	Induced flow velocity due to the shed wake
λ_j	Induced flow velocity for the jth strip
$\boldsymbol{\xi}$	Generalised displacements in the ROM subspace
$\boldsymbol{\pi}$	Momentum variable of the ROM
ρ	Air density
$\boldsymbol{\phi}$	Vector of amplitudes of the loads included in the load matrix
$\boldsymbol{\Phi}_n$	Eigenvector corresponding to the n^{th} mode

Roman Symbols

a	Dimensionless parameter which determines the location of the reference point
$\bar{A}$	Constant computed according to Peters theory
A	Cross-section area of beam element
$\bar{b}$	Constant computed according to Peters theory
b	Semi-chord length of an airfoil
b_s	Width of strip in the aerodynamic model
$\bar{c}$	Constant computed according to Peters theory
$\boldsymbol{C}$	Cubic stiffness tensor of the FE model
$\overline{\boldsymbol{C}}$	Cubic stiffness tensor of the ROM
$\boldsymbol{d}^{\boldsymbol{j}}_{\boldsymbol{aero}}$	Aerodynamic damping corresponding to j^{th} strip
D_e	Dissipation energy

$\boldsymbol{D}_a$	Assembled aerodynamic damping matrix
$\boldsymbol{D}$	Damping matrix of the FE model
$\bar{\boldsymbol{D}}$	Damping matrix of the ROM
E	Elastic modulus
$\boldsymbol{f}_{ex}$	External load vector
$\boldsymbol{f}_{int}$	Element internal force
$\boldsymbol{f}_{k}$	Sub-load vectors included in the load matrix
$\boldsymbol{F}$	Load matrix utilised in the model order reduction
$\boldsymbol{F}_{aero}$	Load vector comprising aerodynamic forces and moments
h	Plunge motion of an airfoil at the reference point
$\boldsymbol{k}_{aero}^{j}$	Aerodynamic stiffness corresponding to j^{th} strip
$\boldsymbol{K}_a$	Assembled aerodynamic stiffness matrix
$\boldsymbol{K}$	Linear stiffness matrix of the FE model
$\bar{\boldsymbol{K}}$	Linear stiffness matrix of the ROM
l	Length of beam element
L_0	Lift per unit span
m	Number of vectors included in the load matrix
$\boldsymbol{m}_{aero}^{j}$	Aerodynamic mass corresponding to j^{th} strip
M_0	Moment per unit span
$\boldsymbol{M}_a$	Assembled aerodynamic mass matrix
$\boldsymbol{M}$	Mass matrix of the FE model
$\bar{\boldsymbol{M}}$	Mass matrix of the ROM
N_d	Number of degrees of freedom in the FE model
N	Number of induced flow states
$\boldsymbol{p}$	Momentum vector of the FE model
$\boldsymbol{P}$	Basis matrix utilised in the momentum subspace formulation

$\boldsymbol{q}$	Element degrees of freedom
$\boldsymbol{q_0}$	Current deformation state of the structure
$\boldsymbol{Q}$	Quadratic stiffness tensor of the FE model
$\bar{\boldsymbol{Q}}$	Quadratic stiffness tensor of the ROM
t	Time variable
T	Total kinetic energy in the FE model
$\boldsymbol{u}$	Displacement vector of the FE model
$\boldsymbol{u_\alpha}$	First order displacement field
$\boldsymbol{u_{\alpha\beta}}$	Second order displacement field
$\boldsymbol{u_{\alpha\beta\gamma}}$	Third order displacement field
U_e	Strain energy
U	Air flow speed
w_s	Structural degree of freedom in the transverse direction
W	Weight factor for tip loss correction

Summary

Modern aircraft designs aim to enhance overall performance and reduce fuel consumption, thereby minimising costs. The growing interest in high-aspect-ratio wings stems from the potential gains in aerodynamic performance. Concurrently, the utilisation of composite materials in the aircraft primary structure for weight reduction is increasing. Both aspects influence wing flexibility and may result in larger wing deflections than those of existing aircraft during operational conditions. Under appropriate loading conditions, the wing deflections can be large enough to surpass the threshold of geometrically linear analyses. This adds complexity to both structural and aeroelastic analyses.

The primary challenge in nonlinear structural analyses arises due to the replacement of the scalable linear methods with the iterative predictor-corrector methods. This can significantly exacerbate the required computational effort. The same limitation also extends to aeroelastic analyses. Beyond the computational aspects, the larger wing deflections introduce aeroelastic effects that cannot be modelled using the linear methods. Prior studies have demonstrated the influence of geometric nonlinearities on aeroelastic characteristics. Notably, a majority of numerical models used to investigate these effects so far rely on variants of geometrically exact beam theory for incorporating nonlinear structural kinematics. While this approach makes the analyses computationally efficient, it involves transforming finite element models into equivalent beam models.

The main objective of this dissertation is to develop a reduced-order nonlinear aeroelastic model that can be directly applied to finite

element models. The modelling of the nonlinear structural kinematics is accomplished through the utilisation of the Koiter-Newton (K-N) method. The K-N method is a finite element-based reduced order modelling (ROM) technique that utilises a cubically nonlinear model derived from the asymptotic expansion of the internal forces about an equilibrium position. The technique, however, is not inherently designed to tackle foreshortening effects in cantilevers undergoing large deflections. To address this limitation, a strategy is adopted to update the ROM at fixed displacement intervals. The key idea here is to incorporate the displacement-dependent structural characteristics into the ROM parameters. The application of this approach yields considerable improvements in capturing the large-amplitude static response. The approach is elaborated in Chapter 2 of this dissertation.

Next, the large-amplitude dynamics of cantilevered structures is investigated. The ROM constructed for the nonlinear dynamics problem differs from the model utilised in the statics problem. Chapter 3 describes a variant of the K-N method which can be utilised for investigating the nonlinear dynamic response in structures. The limitations described in Chapter 2, pertaining to the foreshortening effects, also apply to the dynamics case. A methodology is proposed to enhance the accuracy of the ROM for capturing extremely large amplitude dynamics (tip deflections up to 80% of the span) in cantilevered structures. In the related investigations, the ROM is found to be highly efficient compared to full-order models without exhibiting a significant loss in accuracy.

Chapter 4 describes the development of the finite element (FE) model of the Pazy wing, which is chosen as the reference for the aeroelastic investigations. Modelling adaptations in the FE model are described, which are necessary for the compatibility of the model with the analysis framework utilised in this research. The FE model verification is

performed by conducting nonlinear static and dynamic analyses. The obtained results demonstrate that the developed model can be effectively analysed using the procedures discussed in Chapters 2 and 3.

After verifying the structural ROM and the FE model, the work focuses on the application of the K-N method to nonlinear aeroelastic analyses. To this end, an aeroelastic model is developed by coupling the structural ROM to a low-fidelity aerodynamics model based on the Peters finite-state unsteady thin-airfoil theory (see Chapter 5). The choice of this aerodynamics model is made based on its compatibility with large deflection motion and fast computation times. The combined numerical formulation links the generalised displacement variables, in which the ROM is formulated, to the aerodynamic state variables. The model verification is conducted through its application to the Pazy wing. The developed aeroelastic model can predict flutter onset and offset speeds comparable to reference numerical models under the chosen test conditions. Additionally, the model is also able to capture limit cycle oscillations in the region of flutter instability, which occur in the presence of nonlinearities. The results of this dissertation identify the benefits and shortcomings of the nonlinear aeroelastic model based on the K-N method, and provide insights into potential future developments.

Samenvatting

Moderne vliegtuigontwerpen zijn gericht op het verbeteren van de algemene prestaties en het verminderen van het brandstofverbruik, waardoor de kosten geminimaliseerd worden. De groeiende interesse in vleugels met een hoge aspect ratio komt voort uit de potentiële verbetering van de aerodynamische prestaties. Tegelijkertijd neemt het gebruik van composietmaterialen in de primaire structuur van vliegtuigen toe om het gewicht te verminderen. Beide aspecten beïnvloeden de flexibiliteit van de vleugel en kunnen resulteren in grotere vleugeldoorbuigingen dan die van bestaande vliegtuigen tijdens operationele omstandigheden. Onder de juiste belastingsomstandigheden kunnen de vleugeldoorbuigingen groot genoeg zijn om de drempelwaarde van geometrisch lineaire analyses te overschrijden. Dit voegt complexiteit toe aan zowel structurele als aero-elastische analyses.

De grootste uitdaging bij niet-lineaire structurele analyses ontstaat door de vervanging van de schaalbare lineaire methoden door de iteratieve predictor-corrector methoden. Dit kan de benodigde rekenkracht aanzienlijk vergroten. Dezelfde beperking geldt ook voor aero-elastische analyses. Naast de rekenkundige aspecten introduceren de grotere vleugeldoorbuigingen aero-elastische effecten die niet gemodelleerd kunnen worden met de lineaire methoden. Eerdere studies hebben de invloed van geometrische niet-lineariteiten op aero-elastische karakteristieken aangetoond. Daarbij is op te merken dat de meerderheid van de numerieke modellen die tot nu toe worden gebruikt om deze effecten te onderzoeken, afhankelijk zijn van varianten van de geometrisch exacte balkentheorie voor het integreren van niet-lineaire

structurele kinematica. Hoewel deze aanpak de analyses rekenkundig efficiënt maakt, moeten eindige-elementenmodellen worden omgezet in equivalente balkenmodellen.

Het hoofddoel van dit proefschrift is het ontwikkelen van een niet-lineair aero-elastisch model van een gereduceerde orde dat direct kan worden toegepast op eindige-elementenmodellen. De modellering van de niet-lineaire structurele kinematica wordt bereikt door gebruik te maken van de Koiter-Newton (K-N) methode. De K-N-methode is een op eindige elementen gebaseerde techniek voor modellering op basis van gereduceerde orde (ROM) die gebruik maakt van een kubisch niet-lineair model dat is afgeleid van de asymptotische expansie van de interne krachten rond een evenwichtstoestand. De techniek is echter niet inherent ontworpen om verkortingseffecten aan te pakken in cantilevers die grote doorbuigingen ondergaan. Om deze beperking aan te pakken, wordt een strategie gebruikt om het ROM bij vaste verplaatsingsintervallen bij te werken. Het kern idee hierbij is om de verplaatsingsafhankelijke structurele kenmerken op te nemen in de ROM-parameters. De toepassing van deze aanpak levert aanzienlijke verbeteringen op in het vastleggen van de statische reactie bij grote amplitude. De methode wordt uitgewerkt in hoofdstuk 2 van dit proefschrift.

Vervolgens wordt de dynamica van vrijdragende constructies met grote amplitude onderzocht. De ROM die geconstrueerd is voor het niet-lineaire dynamische probleem verschilt van het model dat gebruikt is voor het statische probleem. Hoofdstuk 3 beschrijft een variant van de K-N-methode die gebruikt kan worden voor het onderzoeken van de niet-lineaire dynamische reactie in constructies. De beperkingen die beschreven zijn in hoofdstuk 2, met betrekking tot de verkortingseffecten, zijn ook van toepassing op het dynamische geval. Er wordt een methode

voorgesteld om de nauwkeurigheid van het ROM te verbeteren voor het vastleggen van dynamica met extreem grote amplitude (tipdoorbuigingen tot 80% van de spanwijdte) in vrijdragende constructies. In de gerelateerde onderzoeken blijkt het ROM zeer efficiënt te zijn in vergelijking met volledige-orde-modellen zonder een significant verlies in nauwkeurigheid.

Hoofdstuk 4 beschrijft de ontwikkeling van het eindige-elementenmodel (FE-model) van de Pazy-vleugel, dat is gekozen als referentie voor het aero-elastische onderzoek. Modelaanpassingen in het FE-model worden beschreven, die nodig zijn voor de compatibiliteit van het model met het analysekader dat in dit onderzoek wordt gebruikt. De verificatie van het FE-model wordt gerealiseerd door niet-lineaire statische en dynamische analyses. De verkregen resultaten tonen aan dat het ontwikkelde model effectief kan worden geanalyseerd met behulp van de procedures die in hoofdstuk 2 en 3 zijn besproken.

Na het verifiëren van het structurele ROM en het FE-model, richt het werk zich op de toepassing van de K-N methode op niet-lineaire aero-elastische analyses. Hiertoe wordt een aero-elastisch model ontwikkeld door de structurele ROM te koppelen aan een low-fidelity aerodynamicamodel gebaseerd op de Peters finite-state unsteady thin-airfoil theory (zie hoofdstuk 5). De keuze voor dit aerodynamicamodel is gebaseerd op de compatibiliteit met grote doorbuigingsbewegingen en snelle rekentijden. De gecombineerde numerieke formulering koppelt de gegeneraliseerde verplaatsingsvariabelen, waarin het ROM is geformuleerd, aan de aerodynamische toestandsvariabelen. Het model wordt geverifieerd door het toe te passen op de Pazy-vleugel. Het ontwikkelde aero-elastische model kan flutter begin -en eind snelheden voorspellen die vergelijkbaar zijn met die van numerieke referentiemodellen onder de gekozen testomstandigheden. Bovendien is

het model ook in staat om limietcyckels in het gebied van flutterinstabiliteit, die optreden in de aanwezigheid van niet-lineariteiten, vast te leggen. De resultaten van dit proefschrift identificeren de voordelen en tekortkomingen van het niet-lineaire aero-elastische model op basis van de K-N-methode, en geven inzicht in mogelijke toekomstige ontwikkelingen.

1

INTRODUCTION

Improvements in aircraft performance and efficiency have been the primary driving factors for technological innovations in the aviation industry. Achieving lower emissions, which contributes to global environmental preservation efforts, is directly linked to several design factors. From a structural perspective, designers strive to minimise the aircraft mass to meet this objective. The utilisation of composite materials is becoming more prominent in this context due to their higher strength-to-mass and stiffness-to-mass ratios, which usually result in a comparatively lightweight structure. Moreover, designers have more control over the directional stiffness of composites, which allows tailoring of the structural properties (Dillinger, 2014). The application of such novel materials has an impact on wing flexibility, potentially resulting in larger wing deflections. The Airbus A350 is well-known for its utilisation of up to 53% composite materials in the airframe construction (Marsh, 2010) and has a visibly large wing deflection during flight.

Aerodynamic drag is another factor that influences total fuel consumption. Point-to-point transportation of an aircraft involves, to a large extent, overcoming air resistance, besides gravitational forces. Therefore, drag minimisation is one of the primary considerations in the design of an aircraft. Total drag can be segregated into drag components influenced by viscous and transonic effects and drag components arising as a consequence of lift generation. At cruise conditions for a typical transport aircraft, lift-induced drag can constitute up to 40% of the total drag (Kroo, 2001). This drag component is associated with the tip vorticity effects of the wing. One way to reduce it is through high-aspect-ratio wing designs, which minimise tip vorticity and, consequently, the induced drag component. The slender wing designs, however, introduce additional challenges due to increased wing flexibility and lower structural frequencies (Gonzalez et al., 2024). The combination of novel lightweight materials and high-aspect-ratio wings can potentially lead to wing deflections exceeding the geometrically linear domain.

Looking beyond conventional aircraft, we need to go back a couple of decades in time to observe the hazardous effects of unaccounted increased flexibility in wings. The remotely piloted environmental research aircraft *Helios Prototype* took off on the 26th June 2003 and soon encountered turbulence during flight, which caused the wing to deform with a persistently high dihedral angle. The consequent instability led to a structural failure and ultimately resulted in the loss of the aircraft. The crash investigation report highlights the lack of adequate analysis techniques for highly flexible wings. One of the key recommendations is the development of multidisciplinary time-domain analysis methods suitable for highly flexible wings (Noll et al., 2004).

Figure 1.1: Helios Prototype HP01 High-Altitude Configuration (Noll et al., 2004)

As wing designs evolve into more flexible structures, it is evident that the historically used linear analysis methods are insufficient for analysing such structures. A generally accepted view is that when the normalised wing tip deflections exceed 10% of the semi-span, geometrically nonlinear effects become relevant (Ritter, 2019). Structural solvers based on finite element (FE) methods already incorporate the necessary mechanics to model such nonlinear behaviour accurately. However, they come with one major limitation, which is the significantly high computational costs in comparison to linear models. In particular, time domain structural analyses can be costly for large deflection problems. In the field of nonlinear structural dynamics, this is tackled through the utilisation of reduced order models (ROM). However, few methods exist which have been applied to large-scale structural models for time domain simulations. Constructing such ROMs can be even more challenging for aircraft wings because accurate predictions of the structural deflections involve the complex modelling of the aerodynamic and structural interactions, also known as aeroelasticity.

This chapter aims to provide an overview of the various aspects of nonlinear structural and aeroelastic modelling. Section 1.1 provides an insight into structural nonlinearities and various methodologies developed specifically for modelling nonlinear structural behaviour. Progress in the field of nonlinear aeroelasticity is discussed in Section 1.2. Section 1.3 highlights the progress in methods developed for modelling large amplitude dynamics. Finally, the dissertation objectives and layout are summarised in Section 1.4.

1.1. STRUCTURAL NONLINEARITIES

In many engineering problems, it is often sufficient to linearise the system for predicting the structural response. It is assumed in such cases that the stiffness of the structure remains constant regardless of the state of deformation. This is generally a valid approximation when deformations are small. In practice, however, the stiffness of an elastic structure is a function of the deformation. In aerospace structures, two commonly observable nonlinear structural behaviours, depending on the boundary conditions and the kinematics of the structure, are: (1) nonlinearity due to bending-stretching coupling in thin panels and (2) nonlinearity due to large rotations. In the first case, distinctive differences between linear and nonlinear solutions are observable at very small deflections, in the order of magnitude similar to the panel thickness. In such structures, investigations pertaining to nonlinear vibrations are of great interest (Amabili, 2008).

The second form is commonly observable in cantilever structures where the free end can undergo large rotations under appropriate loading conditions. In the early work of Bisshopp and Drucker (1945), it is highlighted that the solution for the large deflection of beams is not

attainable using elementary beam theory without correction for beam foreshortening effects and nonlinear curvature.

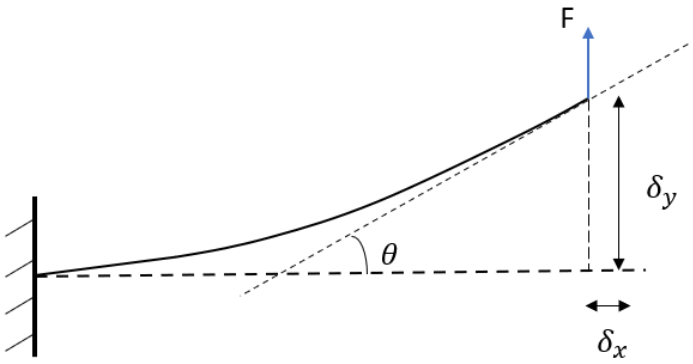

Figure 1.2: Large deflection motion and beam foreshortening in cantilevers

The visualisation in Fig. 1.2 shows the beam foreshortening occurring during large deflection motion with an applied transverse tip load. It is observable that, along with the transverse deflection δ_y, the beam also undergoes an in-plane deflection δ_x in the axial direction, which is a direct consequence of the beam rotation. Assuming that there are no forces acting in the axial direction, it can also be concluded that for smaller beam deflections, the in-plane axial displacement is relatively smaller. Therefore, there is a deflection limit until which the foreshortening effect does not play a major role and the linear approximations are valid. However, in the case of large deflections, the implication of this axial in-plane motion is that the moment arm does not remain constant along the load-deflection trajectory. The root bending moment, therefore, varies as the deflection changes.

When considering forces due to applied pressure, the direction of the forces always remains normal to the tangent at the point of application. This implies that in a two-dimensional plane, such as the one

shown in Fig. 1.2, the forces can be resolved into a transverse and an in-plane axial component. The force components undergo a continuous change as the structure deflects, and this must be accounted for in large deflection problems. These types of forces are referred to as follower forces and are a characteristic of the aerodynamic forces acting on wing structures (Ritter, 2019). Moreover, the changing curvature of the structure also affects its structural stiffness. Since the linear methods neglect these effects, this inevitably leads to artificial extension and over-prediction of the displacements. Several methods have been developed to overcome this limitation. The following subsections provide an overview of various methods with application to the nonlinear analysis of highly flexible structures. In Section 1.1.1, the nonlinear finite element method is discussed, Section 1.1.2 discusses the geometrically exact beam theory, which is commonly applied to equivalent beam models of flexible wings, and Section 1.1.3 discusses numerical methods that utilise finite element models to construct reduced-order models for efficient nonlinear analyses.

1.1.1. Nonlinear finite element method

The Finite Element method is currently the standard approach for solving a diverse range of structural problems. Originally developed for linear analyses, the understanding of the general behaviour of flexible structures led to the demand for further developments in the field of nonlinear finite element analysis. One of the earliest works on nonlinear FE analysis was initiated by Turner et al. (1960), coincidentally in the aerospace industry. The related article describes how the then relatively new FE method can be extended to handle large deflections using iterative procedures and simultaneous update of coordinates. The application of iterative procedures enables us to account for the variation

in the structural stiffness, loads and elastic properties of the structure. The utilisation of the Newton-Raphson method for this purpose was independently proposed by Mallet & Marcel (1968) and Oden (1967). The incremental FE problem for nonlinear analyses is generally formulated using three approaches: (1) total Lagrangian, (2) updated Lagrangian, and (3) the corotational framework (Crisfield et al., 1997).

The main characteristics of the total Lagrangian method are: (1) no assumption for small displacements is required, (2) the initial configuration is assumed to be the reference configuration, and (3) stresses and strains are computed with respect to the initial configuration. The basis of the FE formulation is to solve the equation of motion based on the principle of virtual work, which is described as:

$$\int_{\mathbf{V^0}} {}^{\mathrm{t+\Delta t}}_{0}\mathbf{S}\ \delta({}^{\mathrm{t+\Delta t}}_{0}\boldsymbol{\epsilon}_{ij})\ d\mathrm{V}^0\ = {}^{\mathrm{t+\Delta t}}\mathbf{R} \tag{1.1}$$

where $\mathbf{S}$ is the second Piola-Kirchhoff stress, $\boldsymbol{\epsilon}$ is the Green-Lagrange strain, $\mathbf{R}$ is a vector of external nodal forces, V is the element volume, the superscript t represents the current configuration, the superscript Δt represents an incremental change in the configuration and the superscript 0 represents the initial configuration. The integration in Eq. 1.1 is performed over the volume of the initial configuration.

The updated Lagrangian approach differs from the total Lagrangian in how the reference configuration is defined. All computations in the updated Lagrangian formulation are done with the configuration in the previous analysis step as the reference. This implies that the reference configuration is updated in each analysis step. Stresses and strains in the current configuration are also evaluated with

respect to the previous configuration. The equation of motion is thus described as:

$$\int_{\mathbf{V}^{t}} {}^{t+\Delta t}_{t}\mathbf{S}\ \delta({}^{t+\Delta t}_{t}\boldsymbol{\epsilon}_{ij})\, d\mathrm{V}^{t} = {}^{t+\Delta t}\mathbf{R} \tag{1.2}$$

The relatively new corotational formulation is especially suitable for structures undergoing finite rotations and small strains (Argyris et al., 1978). A local element coordinate system is defined in this method, which rotates and translates along with the element. Therefore, in the local frame of reference, the rigid body motion and the pure deformation component can be separated. The earliest foundational work can be traced back to Wempner (1969), who decomposed the motion of a Kirchhoff shell element into a rigid body motion followed by a deformation. The goal of this approach was to extend existing linear elastic formulations to finite rotations and buckling problems. The generation of the tangent stiffness matrix in the corotational approach through a consistent derivation based on the local-global transformation matrices was explored by Oran (1976). Currently, several related works can be found in the literature (Rankin and Brogan, 1986; Battini and Pacoste, 2002; Felippa, 2000; Moita and Crisfield, 1996; Garcea et al., 2012; Sodja et al., 2021), which further affirm the applicability of the corotational formulation to nonlinear analyses.

Regardless of the formulation used, the obtained stiffness matrix is a function of the structural deformations and is commonly referred to as the tangent stiffness matrix. Predictor-corrector methods, such as the Newton-Raphson method, are required to solve such problems. As the terminology suggests, it comprises an initial predictor step where an initial guess for the solution is made, followed by a corrector step where the guessed initial solution is updated until it satisfies the equilibrium

conditions. Figure 1.3 illustrates the Newton-Raphson method, providing insight into the nature of predictor-corrector methods.

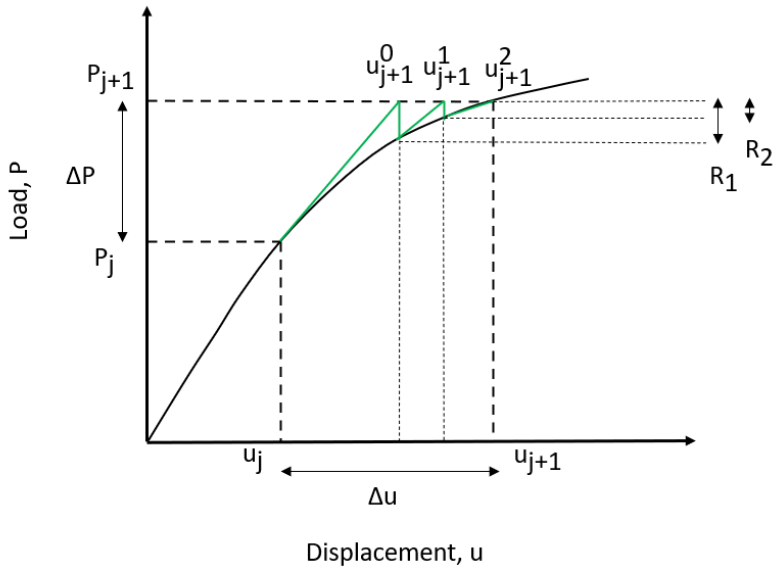

Figure 1.3: Representation of the Newton-Raphson method

The reference state of the structure lies at a known solution $\mathbf{u_j}$ at the applied load $\mathbf{P_j}$. An initial guess to the solution $\mathbf{u}^0_{j+1}$ for a load step $\Delta\mathbf{P}$ is made using the tangent stiffness matrix computed at the deformation state $\mathbf{u_j}$. The residual $\mathbf{R_1}$, which is the norm of the difference between the applied external force vector and the total internal force, is computed at deformation $\mathbf{u}^0_{j+1}$.The next iteration of the solution step makes a solution correction based on the residual force and the tangent stiffness matrix. The process is repeated until the residual forces are minimised to a user-defined limit. Due to the incremental load application and iterative process followed, nonlinear analyses are more time-consuming compared to linear methods.

1.1.2. Geometrically exact beam theory

Modelling of slender structures as equivalent beams is a widely applied strategy, provided it is possible to easily obtain equivalent beam structural properties corresponding to the structure. This implies that the equivalent beam model should be able to capture the global deflection and rotation behaviour in all six degrees of freedom comparably to a full 3-D model. The reduced model complexity is beneficial since such beam models can be solved efficiently using analytical or finite element methods based on beam theories. In particular, for large deflection problems, the geometrically exact beam theory (GEBT) has been effectively utilised in several research works. The GEBT is a nonlinear beam theory which does not make any simplifying assumptions regarding the kinematics of the beam. The main characteristics of this theory are: (1) consideration of finite rotations and displacements without small-angle assumptions, (2) no approximations regarding the deformations, i.e. axial, bending, shear and torsional deformations are all included, and (3) inclusion of fully nonlinear strains. According to Crisfield and Jelenic (1999), “when the relationships between the configuration and strain measures are consistent with the virtual work principle and the equilibrium equations at a deformed state, regardless of the magnitude of displacements, rotations and strains”, the theory is deemed to be geometrically exact. Howcroft et al. (2018) describe a geometrically exact beam formulation in their nonlinear beam shape approach where the equations of motion are obtained using a variational approach and the beam deformations are represented using assumed shape functions based on Chebyshev polynomials which satisfy prescribed boundary conditions. Applications of the GEBT for nonlinear analyses of slender structures have been further successfully demonstrated by Hodges (1990), Cesnik et al. (1996), and Patil and Hodges (2004).

1.1.3. Reduced-order models based on the finite element method

Several methods have been recently developed that rely on FE models to construct reduced order models and aim to perform nonlinear analyses in a more efficient manner in comparison to the traditional FE method. The utilisation of modal methods in linear models is well established and often used for reducing the model order for efficient analyses. However, this is not directly applicable to nonlinear analyses since the principle of superposition, which forms the core of linear modal reduction, is no longer valid. Furthermore, the mode shapes utilised in modal reduction are computed with a small-angle approximation and therefore cannot accurately be used for large deflection analyses. The subsequent sections summarize methods where the nonlinear ROMs are obtained with the direct or indirect use of the finite element method.

1.1.3.1. Modal rotation method

The Modal Rotation Method (MRM) aims to resolve the limitations of the traditional modal reduction methods by utilising curvature-based mode shapes rather than displacement-based mode shapes (Drachinsky, 2020). The method is based on the idea that discretising a structure into fine enough segments ensures that the change in bending slope in each segment is also small. A linearised evaluation is then possible for the segments, which is summed up over the body using nonlinear kinematics. An iterative procedure is utilised to update the forces based on the deformed shape, which accounts for the changing location and orientation of forces. Studies conducted on large deflection analysis of wing-like structures using the MRM show a high level of accuracy when compared to full FE solutions.

1.1.3.2. Modal derivatives method

The concept of modal derivatives (MD) was first introduced by Idelsohn and Cardona (1985) as an approach for model order reduction through basis enrichment applied to nonlinear dynamic analyses. The change in displacement generally can be expressed as a function of the modal amplitudes. This expression is expanded in the Taylor series, which makes it evident that there is a dependence on the higher-order mode derivatives. According to Jain et al., (2017), the MDs are physically thought of as the sensitivity of an eigenmode corresponding to a displacement given in the direction of the eigenmode. The utilisation of MDs in the context of nonlinear dynamics of large-scale structures is well demonstrated. However, it is also highlighted that the number of MDs required exponentially increases with increasing complexity of the structure, which makes it cumbersome to generate ROMs.

1.1.3.3. Equivalent linearization

The approach presented by Muravyov and Rizzi (2003) is focused on structures exhibiting a high degree of bending-stretching coupling with application to arbitrary FE models. A reduced set of modal equations is obtained using linear eigenvectors. The idea is to obtain a reduced form of the nonlinear component of the internal force $\boldsymbol{\gamma}$. This is expressed as a third-order polynomial function of the modal coordinates q_i with unknown coefficients a_{jk}^r and b_{jkl}^r:

$$\boldsymbol{\gamma}(q_1, q_2, \dots q_L) = \sum_{j=1}^{L}\sum_{k=j}^{L} a_{jk}^r \; q_j \, q_k + \sum_{j=1}^{L}\sum_{k=j}^{L}\sum_{j=l}^{L} b_{jkl}^r \; q_j \, q_k q_l \tag{1.3}$$

where *L* is the number of eigenvectors in the basis matrix. The unknown coefficients are obtained from full FE solutions. The purely nonlinear component of the internal force can be obtained as a difference between the total nodal force and the linear component. A set of linear equations can be obtained from Eq. 1.3 through the application of various displacement fields. The unknown coefficients are then obtainable by solving these linear equations. The method was exclusively tested for clamped and simply supported structures. The authors highlight that for cantilevered structures, it may be essential to utilise displacement fields with in-plane components in order to capture the large rotation effects.

1.1.3.4. Extended modal approach

The Extended modal approach was developed to model geometrically nonlinear behaviour in wing-like structures with direct application to generic FE models. The main features of this approach are: (1) a cubically nonlinear force-displacement relationship derived using Taylor series expansion of the internal strain energy about an equilibrium position, and (2) reconstruction of nodal displacement fields from the generalised displacement using higher order mode components (Ritter et al., 2015). Up to fourth-order mode components are considered in this method, and the studied examples show how the addition of each mode component influences the accuracy of the nonlinear response. The construction of the nonlinear force-displacement relationship relies on a series of full FE nonlinear analyses with the application of various generalised forces. The nonlinear solutions are utilised in a surface fitting procedure to compute the unknown coefficients in the nonlinear force-displacement relationship. Studies conducted on cantilevers using this method have shown accuracy for moderately large deflections.

1.1.3.5. Spectral submanifold approach

The Spectral Submanifold (SSM) approach is based on the concept of invariant manifolds. According to Jain and Haller (2022), “invariant manifolds are low-dimensional surfaces in the phase space of a dynamical system that constitute organising centres of nonlinear dynamics”. Invariant manifolds were previously explored, for example, by Shaw and Pierre (1991); however, they were primarily applied to academic nonlinear dynamics problems due to computational challenges faced when applying them to high-dimensional FE models. The research presented by Jain and Haller (2022) develops methodologies for computing invariant manifolds and their reduced dynamics, with applications to large-scale engineering structures.

1.1.3.6. Koiter-Newton method

The Koiter-Newton method was developed for investigating the post-buckling response of thin-walled structures (Liang, 2013; Liang et al., 2016). It is an asymptotic technique which utilises a cubically nonlinear force-displacement relationship. The higher-order stiffness tensors are evaluated as derivatives of the strain energy with respect to an equilibrium position. Reduced order models are obtained by utilising buckling modes in the reduction basis. The reduction method is combined with an arc-length continuation technique to ensure that the ROM stays valid over the entire equilibrium path. While this approach is applicable to FE models, the earlier studies were focused on buckling-sensitive panel structures.

1.1.3.7. Other indirect methods

Indirect methods have been previously developed which rely on data obtained from FE tools to compute the nonlinear ROM parameters.

Mignolet et al. (2013) provide a comprehensive overview of some of these indirect methods which specifically utilise standard outputs from FE tools. McEwan et al. (2001) developed the combined modal and FE analysis approach for nonlinear dynamic analyses of simply supported and clamped-clamped structures. In this method, a series of nonlinear static analyses are conducted where the applied external loads are a weighted sum of the mode shapes. The obtained deflections are transformed to modal coordinates using the linear eigenmodes. The key idea is to curve fit the restoring force based on the load-deflection dataset obtained from finite element analyses. The nonlinear stiffness coefficients in the modal coordinates are then obtained by performing a regression analysis. Wang et al. (2013) discuss a cubically nonlinear ROM where the nonlinear stiffness coefficients are obtained by imposing a set of displacements and forces on the system and solving the resultant equations simultaneously. The method was applied to cantilever beams and later to a wing structure to demonstrate its effectiveness. Demasi and Palacios (2010) developed a method based on Proper Orthogonal Decomposition (POD). In their approach, the basis utilised for computing the ROM comprises structural tangent modes which are reconstructed using POD. The full-order model is first simulated under prescribed load conditions which produces a displacement dataset. POD is then used to extract the optimal basis functions from this dataset. The full-order model is projected onto the reduced subspace using the POD modes.

1.2. AEROELASTICITY

In the early years of aircraft development, structures were rigid compared to modern-day aircraft, and flight speeds were in the low subsonic regime. Under those conditions, the aeroelastic phenomenon had no significant influence. As the designs evolved in the early 1900s,

novel phenomena were observed, occasionally leading to failure and loss of aircraft. Failure investigation, for example, of the Fokker D.VIII aircraft during World War I, revealed the coupled nature of wing bending and twist, resulting in load redistribution and was perhaps the first documented and understood case of failure resulting from static aeroelastic effects (Bisplinghoff, 2013). Current generation of high-speed aircraft are designed with consideration of all known aeroelastic effects which can be static or dynamic in nature. However, aeroelastic phenomena remain a source of operational incidents.

On the simplest level, aeroelasticity can be explained as the interaction between inertial forces, elastic forces, and aerodynamic forces. The interactions between the various disciplines are often depicted using the Collar triangle (Collar, 1946). As shown in Fig. 1.4, static aeroelasticity involves the study of the interactions between the steady aerodynamics and the elasticity of the structure. The inter-dependency can result in effects such as load redistribution or divergence, which occur when an arbitrary increment in aerodynamic torsional moment exceeds the elastic restoring moment. This leads to a cascading effect, where the aerodynamic forces and structural deformations continuously increase until failure occurs. Under dynamic loading conditions, inertial forces are also involved, in addition to aerodynamic and elastic forces. The most critical dynamic aeroelastic stability phenomena is the flutter phenomenon. In its classical form, it typically involves the coupling of eigenmodes related to two or more degrees of freedom, which leads to unstable oscillations and ultimately results in structural failure. A well-known dynamic aeroelastic effect is the response to gust loads, which act as dynamic perturbations to the aircraft.

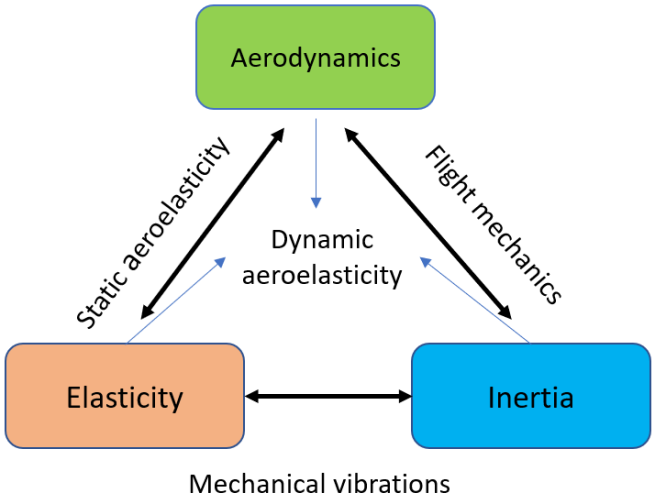

Figure 1.4: The Collar triangle depicting multi-disciplinary interactions in aeroelasticity

Historically, the various methods developed for aeroelastic analyses were generally based on linear structural models, even as the aerodynamics tools evolved. The considerable ease in building numerical models with the linear structural theory and the general lack of requirement for nonlinear structural models due to relatively lower structural flexibility compared to modern-day aircraft, made linear structural models the obvious choice. Modern-day aircraft are still designed using aeroelastic tools based on linear FE methods. However, the need for venturing into the world of structural nonlinearities is also increasingly apparent.

1.2.1. Nonlinear aeroelasticity

Nonlinear aeroelasticity broadly concerns aeroelastic effects arising due to nonlinearities in the structural and aerodynamic responses. In the case of flexible aircraft structures, the utilisation of numerical

methods that account for these nonlinearities is necessary for modelling the nonlinear aeroelastic effects. Some of the first publications in nonlinear aeroelasticity were focused on panel flutter, whose occurrence is primarily observed in supersonic flow (Dowell, 1972). The eigenfrequencies of thin panels are sensitive to deformations due to the membrane stretching coupled to the lateral bending, and thus, nonlinear effects are prominent at sufficiently high static loading. In the related field of nonlinear aeroelasticity of highly flexible wings, there has been a marked increase in developments in the last two decades following the seminal work of Patil et al. (1998, 1999, 2000, 2004). Their research was conducted with the aim of constructing a low-order aeroelastic model for the preliminary design of aircraft with highly flexible wings. The framework includes geometrically nonlinear modelling of wing structures as beams and utilises the mixed variational geometrically exact formulation developed by Cesnik et al. (1996). The aerodynamics is modelled using the finite-state airloads theory (Peters et al., 1994; Peters et al., 1995). The follow-up investigations of a high-aspect-ratio wing by Patil et al. (1999) revealed that the geometrically nonlinear effect is a result of the non-zero steady state curvature of the wing. A reduction in the flutter speed was observed due to large wing deflections. In a later work conducted by Patil et al. (2001), the finite state airloads model is combined with a static stall model to demonstrate that stall limits the amplitudes of limit cycle oscillations (LCO). The studies also showed that LCOs can be observed below the linear flutter speed, a typical characteristic of subcritical flutter in nonlinear aeroelastic systems. The initiation mechanism is attributed to the change in structural characteristics due to large deformation.

Tang and Dowell (2001) performed experimental studies on a high-aspect- ratio wing and measured the response due to LCO of the

wing. One of the main conclusions of their work is that the influence of structural nonlinearity on the LCO behaviour is dependent on the ratio of flexural rigidity in the transverse and chord-wise directions. For wings with a lower ratio of the flexural rigidities, the changes in the flutter boundary with increasing deflections were found to be small. A novel strain-based method was introduced by Cesnik and Su (2005) for modelling nonlinear aeroelastic behaviour of a fully flexible aircraft, i.e. including six rigid body degrees of freedom. The entire aircraft is modelled as a beam structure, and the cross-sectional properties are incorporated into a 1-D nonlinear beam model. Around the same time, a high-fidelity numerical formulation was presented for nonlinear static aeroelastic analyses of slender wings in transonic flow (Palacios and Cesnik, 2005). An asymptotic reduction method was used for the structural representation, whereas the aerodynamics was modelled using the Euler equations. The authors highlight that deformation modes typically captured in 3-D models, for example, corresponding to the camber bending degree of freedom, are of importance. These deformations are not captured in 1-D structural models; therefore, they should be additionally accounted for when using 1-D models with high-fidelity aerodynamics.

In the studies conducted by Jian and Jinwu (2009), a geometrically exact nonlinear anisotropic beam model is combined with a nonlinear dynamic stall model. The work is focused on the initiation and sustaining mechanisms of LCOs. The authors observed in their test case that at lower flow speeds in the absence of stall, geometrical nonlinearities are responsible for the occurrence of LCO. In the presence of dynamic stall, the aerodynamic nonlinearity was found to have a greater influence on the time history evolution of the LCO. The dynamic response of a highly flexible flying wing configuration is investigated by Su and Cesnik (2011). The studies show that gust disturbances could

cause an unstable oscillatory response in the flying wing. UM-NAST, a toolbox for nonlinear aeroelastic analysis of very flexible aircraft, which utilises the methodology developed by Cesnik and Su (2005), was used in these studies. The GEBT is applied in combination with an unsteady aerodynamic model including dynamic stall effects in the investigations conducted by Arena et al. (2013). The work highlights the influence of prestress loads on the post-flutter response. A comparison of five different approaches of modelling geometric nonlinearities and their utilisation in an aeroelastic framework is presented by Howcroft et al. (2016). The authors note that specific attributes of each of these methods can be combined into an overall nonlinear design strategy. Afonso et al. (2017) provide a comprehensive overview of the progress in nonlinear aeroelasticity of highly flexible wings. A vast majority of the research during this period was focused on highly flexible wings under subsonic flow. This is useful for early-stage investigations since aerodynamic nonlinearities are less relevant at low Mach numbers, and the effects due to structural nonlinearities can be focused upon. It is also evident that the geometrically exact beam formulations have been predominantly utilised in such studies. Some of the developed methodologies have been integrated into automated analysis frameworks, which have been lately applied for further investigations of highly flexible wings.

The need for a better understanding of nonlinear aeroelastic behaviour led to the development of configurations such as the X-HALE (Cesnik et al., 2012). One of the objectives of this aircraft was to provide data related to geometrically nonlinear response coupled with flight dynamics, which could act as a reference for future developments in numerical methods. Similarly, wind tunnel experiments were conducted by Xie et al. (2016) for obtaining validation data for their computational framework. More recently, the Pazy wing developed at Technion (Avin et

al., 2022) was studied within the framework of the AIAA third aeroelastic prediction workshop (AePW3) (Ritter et al., 2024). The wing is designed to be highly flexible for investigating nonlinear aeroelastic phenomena and generating experimental data to provide a benchmark for future studies. Major collaborative efforts have been undertaken in the AePW3 to understand nonlinear aeroelastic phenomena using the Pazy wing benchmark. Static aeroelastic test cases were used to demonstrate the effects of geometric stiffening on the wing deflection. Comparisons with linear models clearly highlight the variations in a nonlinear response as the deflection amplitudes increase. Furthermore, the effect of geometric stiffening on the eigenfrequencies of the wing was investigated. Eigenfrequencies corresponding to specific modes were observed to have significant variations with increasing wing deflection (Riso et al., 2021; Hilger and Ritter, 2021; Goizueta et al., 2022; Drachinsky et al., 2022). The eigenfrequency variation has direct implications for the dynamic aeroelastic characteristics of such wing structures. Flutter onset was predicted using eigenvalue analysis of the deformed wing structure. The studies indicate a reduction of the flutter speed in comparison to a fully linear model when the wing undergoes geometrically nonlinear deformation (Hilger and Ritter, 2021; Riso and Cesnik, 2023; Stanford et al., 2024). The flutter onset speed predicted by all collaborative partners of the AePW3 was found to be within a range of $\pm 7\%$ (Ritter et al., 2024) in comparison to the experimental studies done by Drachinsky et al. (2022).

A further excursion into the rich collection of literature on nonlinear aeroelasticity, while compelling, is not necessary in the scope of this work. The key takeaways that can be highlighted here are: (1) Frameworks comprising low order aeroelastic models have been previously constructed, although a majority of them utilize the GEBT for

which it is necessary to have accurate conversion of FE models to equivalent beams, (2) highly flexible wings show distinctly different static structural and modal characteristics at large deflections than what linear models predict, and (3) geometric nonlinearity causes considerable changes in the aeroelastic stability margins and the post-flutter behaviour, thus, development and further improvements in nonlinear aeroelastic frameworks are paramount.

1.2.2. Aerodynamic models in nonlinear aeroelasticity

While structural nonlinearities have been extensively discussed, the choice of an appropriate aerodynamic model is equally important for investigations of nonlinear aeroelastic effects. One of the obvious requirements of such a model is compatibility with large deflection and large rotation behaviour. Additionally, the aerodynamic model should be able to capture unsteady effects if dynamic conditions are of interest. High-fidelity aerodynamics tools based on computational fluid dynamics (CFD) can offer high accuracy; however, they are also computationally the most expensive. Panel methods such as the Doublet Lattice Method (DLM) (Albano and Rodden, 1969) and the Unsteady Vortex Lattice Method (UVLM) (Murua et al., 2012) are other commonly used approaches in computational aeroelasticity. According to Erickson (1990), panel methods refer to numerical schemes which solve for the potential flow about an aircraft. Fundamental analytic solutions exist, which are known as source, doublet and vorticity singularities. The panel methods are based on the superposition of these singularities over discrete panels on the aircraft surface. Since these methods are based on potential flow, viscous effects cannot be modelled. However, these methods are comparatively faster than CFD. Between the two mentioned panel methods, the DLM is commonly used to compute unsteady

aerodynamic forces in linear aeroelastic analyses, but does not inherently account for geometry changes due to large deflection. A small flow perturbation about a steady state condition is assumed in this approach, which is invalid for large deflection problems. The UVLM is suitable for nonlinear aeroelastic investigations conducted at low Mach numbers. As highlighted by Ritter (2019), a major advantage of the UVLM is that the aerodynamic panels can undergo large translations and rotations in all directions. Referring back to the literature on nonlinear aeroelasticity of highly flexible wings in Section 1.2.1, effective utilisation of the UVLM can be seen in the work of Benini et al. (2004), Murua (2012), Howcroft et al. (2016), and Hilger and Ritter (2021).

Strip theory-based models offer an alternative where 2-D approaches can be applied in a simplified manner. In this method, the lifting surface is divided into a sequence of strips, each of whose aerodynamic characteristics is individually determined from the local airfoil definition. It is assumed that there are no interactions of the flow in adjacent strips. Furthermore, 3-D effects cannot be captured, for example, at the wing tip. This can, however, be resolved by introducing corrections based on external data obtained from experiments or high-fidelity numerical methods. The foundational work of Theodorsen (1935) on unsteady aerodynamic forces of an oscillating airfoil and aerodynamic instability is one of the methods applicable in combination with strip theory. Although Theodorsen's theory inherently assumes small harmonic oscillations, it has been applied in nonlinear aeroelastic models where the nonlinear behaviour is introduced due to freeplay, i.e. mechanical clearances between structural components (Conner et al., 1997). In a similar study conducted by Fernandez-Escudero et al. (2019), the authors compare the effectiveness and simulation times when using Theodorsen's method and CFD methods. For the test cases investigated,

Theodorsen's model is able to capture the complex LCO behaviour similar to the CFD methods, whereas the simulation times differ by three orders of magnitude. This is, of course, only plausible in the low subsonic regime where the assumptions of potential flow are reasonable and aerodynamic nonlinearities do not have a measurable influence. Palacios *et al.* performed a similar comparison between the UVLM and a strip theory model based on indicial airfoil response (Palacios, 2010); however, they focused on geometrically nonlinear aeroelastic problems. The studies indicate that the strip theory model performs well for small amplitude dynamic motions about a state of large static deflection.

In a review of recent advances in nonlinear aeroelasticity (Xiang et al., 2014), the authors discuss the need for time domain numerical models for capturing the aerodynamic response under arbitrary motion of an airfoil. One of the widely employed models is the unsteady wake model, where the induced velocity from the shed wake contributes to the unsteady aerodynamic effects. The finite-state unsteady thin-airfoil theory, developed by Peters et al. (1994) and Peters et al. (1995), utilises the unsteady wake model. The major advantages of the Peters theory are that it allows for large deformations and arbitrary airfoil motion. The application of Peters theory in nonlinear aeroelastic problems is well demonstrated by Patil et al. (1998), Cesnik and Su (2005) and Riso and Cesnik (2023). The results presented by Ritter et al. (2024) show that for a rectangular wing in subsonic flow, both Peters theory and UVLM predict flutter speeds with an error margin within 2.5% of each other. Another commonly employed model is the dynamic stall model (Tran and Petot, 1980; Leishman and Beddoes, 1989). These are particularly useful when investigating LCO phenomena where amplitudes are expected to exceed the stall limits. Stall refers to the condition where the effective angle of attack exceeds a critical value, resulting in flow separation and loss of lift.

A dynamic stall occurs during oscillatory motion, but with a lagging effect, so that there is a temporary increase in lift followed by a sudden loss of lift.

1.3. LARGE AMPLITUDE DYNAMICS

Nonlinear structural effects resulting in frequency-amplitude dependency during large amplitude oscillations is a well-established concept. The idea of nonlinear normal modes (NNMs) was first described by Rosenberg (1962) for an n-DOF spring mass system as an extension to the linear theory. Kerschen et al. (2009) address the applicability of the NNM concept to large-scale structures and its utility in capturing complex dynamical responses which are very specific to nonlinear systems. In particular, the nonlinear dynamics of thin panels with bending-stretching coupling have been widely investigated using various analytical and numerical techniques. A review of the related research has been presented by Alijani and Amabili (2014) and Touzé et al. (2021). In the context of wing structures, there has not been a substantial interest in studying large amplitude dynamics in the sense of NNMs since traditionally wings were never designed to be flexible enough to transition into the geometrically nonlinear domain. Recent developments in highly flexible wings, however, make it worthwhile to investigate their nonlinear dynamical response.

Large amplitude dynamics of cantilevers have been previously primarily studied using analytical beam formulations. Early investigations conducted by Crespo da Silva et al. (1978a, 1978b) utilised the assumption of beam centreline inextensibility to obtain third-order governing equations for modelling moderately large non-planar oscillations. Contributions particularly due to nonlinear curvature and

inertial terms are relevant in accurate nonlinear modelling using these equations. A similar approach is utilised by Mahmoodi and Jalili (2007) with an assumed inextensibility condition for studying nonlinear dynamics of micro-cantilevers. The authors highlight that this assumption is suitable only for cases where the cross-section is much smaller than the length of the beam. As in the statics case, the utilisation of geometrically exact beam theory provides a more generic representation for such models (Simo and Vu-Quock, 1991; Vu-Quoc and Deng, 1995).

An invariant manifold approach is utilised for studying the nonlinear dynamic response of structures where the nonlinearities purely arise from the large deformation kinematics (Shang-Rou et al., 1994). A key finding of their work is that linear normal modes provide a suitable representation of the NNM shape in cantilevers for tip displacements up to 50% of the beam length. This can be obtained just by accounting for the kinematic effect due to beam foreshortening. Yoo et al. (2003) conducted a nonlinear dynamic analysis in the time domain using the absolute nodal coordinate formulation, which is an FE technique and compared it to experiments. The authors utilised the Rayleigh damping and showed that, for low damping ratios, considering only mass-proportional damping in their analysis model provides a comparable result to the full Rayleigh damping. In the experimental work of Farokhi et al. (2022), extremely large amplitude dynamic motion of a cantilever sheet is studied using a geometrically exact beam model along with experimental validation. The authors emphasise that the commonly used third-order nonlinear model is insufficient for modelling extremely large amplitude oscillations. The analytical results show that for the simple beam structure, the hardening effect appears but only at amplitudes beyond a tip deflection of 60% of the beam length. This behaviour is in contrast to the nonlinear dynamics of thin panels, where the onset of

frequency variations begins to occur at relatively much lower amplitudes. Nevertheless, this does not necessarily give an indication about the dynamics of a more complex assembly, such as a wing structure.

1.4. OBJECTIVES AND DISSERTATION LAYOUT

The state-of-the-art presented in the previous Sections highlights the importance of considering structural nonlinearities in numerical models when investigating aeroelastic effects in wings undergoing geometrically nonlinear deformations. Prior numerical studies using low-fidelity aerodynamics and nonlinear structural models have demonstrated the occurrence of nonlinear aeroelastic effects, which are overlooked when using traditional linear methods. The drawback of utilising full order FE models in such numerical studies is the higher computational cost compared to linear models. This can be circumvented through the use of structural ROMs. However, constructing ROMs, specifically eigenmode-based ROMs, for large deflection problems is not a straightforward task. Structural eigenmodes are computed with a small-angle approximation and do not contain information about large deflections and rotations in structures. A majority of the numerical methods previously developed have utilised variants of the geometrically exact beam theory. This approach, however, requires accurate transformation of complex FE models to equivalent beams.

The primary objective of this dissertation is to develop a reduced order nonlinear aeroelastic model for investigating geometrically nonlinear aeroelastic effects in highly flexible wings under subsonic flow. The described framework can be directly applied to FE models where reduced simulation times are achievable through the utilisation of a structural ROM. The presented work expands the scope of the Koiter-

Newton method, briefly discussed in Section 1.1.3, which is compatible with generic FE models. Initial assessment of the Koiter-Newton method for large deflection static analysis revealed that if the ROM is formulated in the initial undeformed state, it can only accurately trace the load-deflection path up to 20% tip deflection. By extension, similar characteristics are also exhibited in the dynamic analyses. In this work, one of the objectives was to assess and, if possible, improve the performance of the ROM for studying large amplitude dynamics in cantilevers. To this end, a strategy to update the ROM is proposed such that the effects of geometrically nonlinear deformation are integrated in the ROM construction process. The key idea here is that reduction bases, when defined in the initial configuration of the structure, do not contain information about the geometrically nonlinear effects. Therefore, updating the reduction bases as the structure deforms enables us to extend the domain applicability of the ROM.

For the development of the reduced order nonlinear aeroelastic framework, the ROM obtained from the Koiter-Newton method is coupled to the aerodynamics model based on Peters theory. The choice of the aerodynamics model is based on prior research presented in the literature review showing its accuracy in the low subsonic regime, as well as the relatively faster computational times compared to the higher fidelity aerodynamics methods such as UVLM and CFD. To construct an aeroelastic model, the process requires coupling of the generalised displacement variables of the ROM subspace to the aerodynamic degrees of freedom. A coupling strategy of the structural ROM, obtained from the K-N method, to the aerodynamics model is presented in this dissertation. The overall performance of the nonlinear aeroelastic framework is assessed through investigations of various aspects of nonlinear aeroelastic behaviour in a highly flexible wing.

The remainder of the dissertation is structured as follows. In Chapter 2, investigations pertaining to nonlinear static analyses of cantilevers using the Koiter-Newton method are presented. The theoretical formulation of the Koiter-Newton method is discussed, limitations applicable due to large rotation problems are highlighted, and verification studies are presented. Chapter 3 discusses the methodology used for investigating large amplitude dynamics. A novel adaptation of the Koiter-Newton method is presented, which allows modelling of the large amplitude dynamics in cantilevers. In Chapter 4, the Pazy wing benchmark case is presented, which is utilised as the reference model for aeroelastic studies conducted in this work. The nonlinear static and dynamic characteristics of the Pazy wing are presented. Chapter 5 builds upon the structural ROM and describes the development of the reduced order nonlinear aeroelastic framework with the utilisation of an appropriate aerodynamics model. Furthermore, the analyses performed on the Pazy wing using this framework are presented in Chapter 5. In Chapter 6, the conclusions and recommendations derived from this dissertation are presented.

2

NONLINEAR STATIC ANALYSES OF HIGHLY FLEXIBLE WINGS

In Section 1.1, the challenges in modelling geometrically nonlinear behaviour in cantilevers are highlighted. As discussed by Bisshopp and Drucker[1] (1945), the inclusion of the foreshortening effect and the nonlinear curvature is necessary for accurately modelling the nonlinear response in cantilevers. In this context, the use of geometrically exact beam theory is well-established (Hodges, 1990; Cesnik et al., 1996; Crisfield and Jelenić, 1999; Patil and Hodges, 2004) and offers an elegant solution when the structural model can be defined as a beam. However,

This Chapter is based on the publication: Sinha, K., Alijani, F., Krüger, W. R., & De Breuker, R. (2023). Koiter–Newton based model reduction for large deflection analysis of wing structures. *AIAA Journal*, *61*(8), 3608-3617.

few reduced-order modelling techniques have previously addressed the large deflection problem in 3-D finite element geometries (Idelsohn and Cardona, 1985; Muravyov and Rizzi, 2003; Ritter et al., 2015; Jain et al., 2017; Drachinsky and Raveh, 2020). This is primarily because the traditional modal reduction approach, which uses linear eigenmodes, has limited application in large deflection problems due to the small-angle approximations inherent in eigenmode computations. Modelling adaptations, such as the enrichment of the reduction basis using modal derivatives, have been found to improve the performance of the nonlinear ROM for moderately large tip deflections in cantilevers ranging up to 25% of the span (Ritter et al., 2015).

The Koiter-Newton (K-N) method (Liang, 2013), which is compatible with finite element models, has been previously utilised for post-buckling analyses of thin panels. This Chapter presents the first investigations, using the Koiter-Newton method, pertaining to geometrically nonlinear behaviour in cantilevers. The theoretical formulation of the Koiter-Newton method is presented in Section 2.1. A strategy for applying the Koiter-Newton method to large deflection problems is proposed in Section 2.2. Numerical studies for validating the method are presented in Section 2.3. The conclusions of the Chapter are presented in Section 2.4.

2.1. KOITER-NEWTON METHOD

The K-N method builds upon Koiter's initial post-buckling analysis (Koiter, 1945). The method was developed to obtain an FE-based ROM formulation for accurately capturing the post-buckling behaviour of thin-walled structures. The method is based on the use of Koiter's asymptotic expansion along the equilibrium path of the structure in combination with

the arclength method. This Section provides an overview of the theoretical formulation of the K-N method.

A statically loaded discrete structure is governed by the equation:

$$\boldsymbol{f}(\boldsymbol{q_0}) = \lambda \boldsymbol{f}_{ex} \tag{2.1}$$

where $\boldsymbol{q_0}$ describes the current configuration of the structure, λ is a load parameter, $\boldsymbol{f_{ex}}$ is a vector of external loads. The presence of buckling in a structure indicates that secondary paths branching out of the main equilibrium path exist. To excite these secondary equilibrium paths, the reduction method proposes a force subspace which comprises the externally applied loads and additional perturbation load vectors.

The force subspace is then defined as:

$$\boldsymbol{f} = \boldsymbol{F}\boldsymbol{\phi} \tag{2.2}$$

where $\boldsymbol{F}$ is the load matrix comprising the sub-load vectors (external force and perturbation loads) $\boldsymbol{f_k}$, $\boldsymbol{\phi}$ is a vector of amplitudes of the load vectors in $\boldsymbol{F}$.

The solution of such a system, in general, lies on a nonlinear surface. This surface is parameterised by coordinates $\boldsymbol{\xi}$ and the solution is approximated using Taylor series expansion. The relationship between $\boldsymbol{\xi}$ and $\boldsymbol{\phi}$ provides the nonlinear reduced order model.

Performing a Taylor series expansion up to the third order on the internal forces (Eq. 2.1) about an equilibrium position with displacements $\boldsymbol{u}$,

reference position $\boldsymbol{q}$ and combining with Eq. 2.2, the nonlinear static equilibrium equations can be redefined as:

$$\boldsymbol{K\,u} + \boldsymbol{Q\,u\,u} + \boldsymbol{C\,u\,u\,u} = \boldsymbol{F\phi} \tag{2.3}$$

where $\boldsymbol{K}$ represents the linear component, $\boldsymbol{Q}$ represents the quadratic component, and $\boldsymbol{C}$ represents the cubic component of the stiffness. Eq. 2.3 describes a full-order model comprising the complete set of N_d degrees of freedom.

The nonlinear equilibrium surface is similarly parametrised using the generalised displacements $\boldsymbol{\xi}$ with up to third-order terms. The equilibrium displacement is then defined as:

$$\boldsymbol{u} = \boldsymbol{u}_{\alpha}\xi_{\alpha} + \boldsymbol{u}_{\alpha\beta}\xi_{\alpha}\xi_{\beta} + \boldsymbol{u}_{\alpha\beta\gamma}\xi_{\alpha}\xi_{\beta}\xi_{\gamma} \tag{2.4}$$

where the subscripts vary from 1 to *m* with the summation convention applied, and *m* is the number of force vectors included in the load matrix described in Eq. 2.2. The coefficients $\boldsymbol{u_{\alpha}}$, $\boldsymbol{u_{\alpha\beta}}$, $\boldsymbol{u_{\alpha\beta\gamma}}$ refer to the first, second and third order displacement fields, respectively. Note that while the derivation of the ROM demands a definition of up to third order displacement field, the real solution is constructed using up to the second order displacement field. The parameterisation of this equilibrium surface is possible in an infinite number of ways. For consistency, this parameterisation is fixed to ensure work equivalence in the full and reduced-order models:

$$(\boldsymbol{F\phi})'\delta\boldsymbol{u} = \boldsymbol{\phi}'\,\delta\boldsymbol{\xi} \tag{2.5}$$

The expansion in Eq. 2.4 is substituted in the left-hand side of Eq. 2.5, which provides the following:

$$(\boldsymbol{F\phi})'\delta\boldsymbol{u} = \boldsymbol{\phi}'\,\boldsymbol{F}'\left(\boldsymbol{u}_\alpha\delta\xi_\alpha + \boldsymbol{u}_{\alpha\beta}\delta\xi_\alpha\xi_\beta + \boldsymbol{u}_{\alpha\beta}\xi_\alpha\delta\xi_\beta + \cdots\right) = \boldsymbol{\phi}'\,\delta\boldsymbol{\xi} \tag{2.6}$$

It is evident from the comparison of the coefficients on the left and right-hand sides of the Eq. 2.6 that all higher-order terms must have zero coefficients. This provides a set of constraint equations relating the sub-load vectors in the load matrix and the displacement fields $\boldsymbol{u_\alpha}, \boldsymbol{u_{\alpha\beta}}$ and $\boldsymbol{u_{\alpha\beta\gamma}}$. The constraint equations are given by:

$$\begin{aligned} \boldsymbol{f_k'u_\alpha} &= \delta_{k\alpha} \\ \boldsymbol{f_k'u_{\alpha\beta}} &= 0 \\ \boldsymbol{f_k'u_{\alpha\beta\gamma}} &= 0 \end{aligned} \tag{2.7}$$

where $\delta_{k\alpha}$ is the Kronecker delta. The constraint equations imply orthogonality between the load vectors and the higher-order displacement fields.

The load amplitudes are expanded consistent with the displacement expansion in Eq. 2.4. The third-order expansion, which is representative of the reduced-order model, is defined as:

$$\boldsymbol{\phi} = \bar{\boldsymbol{K}}\boldsymbol{\xi} + \bar{\boldsymbol{Q}}\boldsymbol{\xi\xi} + \bar{\boldsymbol{C}}\boldsymbol{\xi\xi\xi} \tag{2.8}$$

where $\bar{\boldsymbol{K}}, \bar{\boldsymbol{Q}}, \bar{\boldsymbol{C}}$ are the unknown ROM variables and represent the linear, quadratic and cubic terms, respectively. The determination of these unknown coefficients is based on the algebraic manipulation of the Eqs. 2.3, 2.4 and 2.8. The Eqs. 2.4 and 2.8 are substituted into the Eq. 2.3 and

expanded. The coefficients of various powers of $\boldsymbol{\xi}$ are equated and combined with the constraint equations from Eq. 2.7. The resultant set of linear equations is solvable in a matrix form to obtain the unknown ROM variables using the following equations:

$$\begin{bmatrix} \boldsymbol{K} & -\boldsymbol{F} \\ -\boldsymbol{F}' & \boldsymbol{0} \end{bmatrix} \begin{Bmatrix} \boldsymbol{u}_{\alpha} \\ \overline{\boldsymbol{K}}_{\alpha} \end{Bmatrix} = \begin{Bmatrix} \boldsymbol{0} \\ -\boldsymbol{E}_{\boldsymbol{\alpha}} \end{Bmatrix} \tag{2.9}$$

$$\begin{bmatrix} \boldsymbol{K} & -\boldsymbol{F} \\ -\boldsymbol{F}' & \boldsymbol{0} \end{bmatrix} \begin{Bmatrix} \boldsymbol{u}_{\alpha\beta} \\ \overline{\boldsymbol{Q}}_{\alpha\beta} \end{Bmatrix} = \begin{Bmatrix} -\boldsymbol{Q}(\boldsymbol{u}_{\alpha}, \boldsymbol{u}_{\beta}) \\ \boldsymbol{0} \end{Bmatrix} \tag{2.10}$$

$$\begin{aligned} \bar{C}_{\alpha\beta\gamma\delta} = \boldsymbol{C}(\boldsymbol{u}_{\alpha}, \boldsymbol{u}_{\beta}, \boldsymbol{u}_{\gamma}, \boldsymbol{u}_{\delta}) \\ -\frac{2}{3}\left[\boldsymbol{u'}_{\alpha\beta}\, \boldsymbol{K}\, \boldsymbol{u}_{\delta\gamma} + \boldsymbol{u'}_{\beta\gamma}\, \boldsymbol{K}\, \boldsymbol{u}_{\delta\alpha} + \boldsymbol{u'}_{\gamma\alpha}\, \boldsymbol{K}\, \boldsymbol{u}_{\delta\beta}\right] \end{aligned} \tag{2.11}$$

where $\boldsymbol{E}_{\boldsymbol{\alpha}}$ is a unit vector which has its α^{th} component as one and the other components are zero. Eqs. 2.9 and 2.10 show that the displacement coefficients $\boldsymbol{u}_{\boldsymbol{\alpha}}$ and $\boldsymbol{u}_{\boldsymbol{\alpha\beta}}$ are computed simultaneously with the ROM variables. Therefore, no prior assumptions are required for these terms.

The size of the load matrix $\boldsymbol{F}$ determines the size of the ROM. For example, *m* load vectors included in the load matrix result in a ROM with linear components of the order *m* x *m.* It can be recalled that the perturbation load vectors are added in the load matrix $\boldsymbol{F}$ to excite secondary load-displacement paths. When the buckling response is not investigated, the load matrix consists only of the external force vector and it results in a 1-DOF reduced-order model. The model order can, therefore, be greatly reduced regardless of the size of the initial FE model. The limitation is that the ROM construction relies on the external

forces, which are not necessarily constant in all conditions. Another notable aspect is the construction of higher-order stiffness tensors $\boldsymbol{Q}$ and $\boldsymbol{C}$, as described in Eq. 2.3. Commonly utilised FE software do not provide these higher-order stiffness terms as an output, and therefore, they must be computed independently. These stiffness terms are obtained using a strain energy-based approach, which is illustrated below for a planar beam element with 3-DOF per node.

Nonlinear FE solvers utilise the Green-Lagrange strain model, which, for a beam, defines the strain ϵ as:

$$\epsilon = u_{,x} + \frac{1}{2}\left(u_{,x}^2 + w_{,x}^2\right) \tag{2.12}$$

where *u* and *w* are displacement components in the *x* and *y* directions, respectively and the subscript ,x indicates the derivative with respect to the *x* direction.

The strain energy U_e of a Euler-Bernoulli beam, with cross-section A, length *l* and elastic modulus E, based on the strain description in Eq. 2.12, is defined for a discretised model as:

$$U_e = \frac{1}{2}\,\mathrm{A}l\;\epsilon'\;E\;\epsilon \tag{2.13}$$

The corresponding internal force $\boldsymbol{f_{int}}$ on the element level is computed as the first order derivative of the strain energy, as given by:

$$\boldsymbol{f}_{int} = EAl\;\epsilon\;\frac{\partial \epsilon}{\partial \boldsymbol{q}} \tag{2.14}$$

where $\boldsymbol{q} = [\boldsymbol{u}\ \boldsymbol{v}\ \boldsymbol{\theta}]$ describes the element degrees of freedom.

The stiffness tensors can be similarly obtained through higher order derivatives of the strain energy, defined as:

$$K_{ij} = EAl\left(\epsilon\frac{\partial^2\epsilon}{\partial q_i\,\partial q_j} + \frac{\partial\epsilon}{\partial q_i}\frac{\partial\epsilon}{\partial q_j}\right) \tag{2.15}$$

$$Q_{ijk} = \frac{EAl}{2}\left(\frac{\partial\epsilon}{\partial q_i}\frac{\partial^2\epsilon}{\partial q_j\,\partial q_k} + \frac{\partial\epsilon}{\partial q_j}\frac{\partial^2\epsilon}{\partial q_k\,\partial q_i} + \frac{\partial\epsilon}{\partial q_k}\frac{\partial^2\epsilon}{\partial q_i\partial q_j}\right) \tag{2.16}$$

$$C_{ijkl} = \frac{EAl}{6}\left(\frac{\partial^2\epsilon}{\partial q_i\,\partial q_j}\frac{\partial^2\epsilon}{\partial q_k\,\partial q_l} + \frac{\partial^2\epsilon}{\partial q_i\,\partial q_k}\frac{\partial^2\epsilon}{\partial q_j\,\partial q_l} + \frac{\partial^2\epsilon}{\partial q_i\,\partial q_l}\frac{\partial^2\epsilon}{\partial q_j\partial q_k}\right) \tag{2.17}$$

These stiffness tensors correspond to the axial strain, and therefore, a bending stiffness component obtained from the linear curvature relationship $\chi = w_{,xx}$ must be appended separately. A similar approach is adopted for triangular shell elements with a modified Green-Lagrange strain model, details of which are provided in Appendix I. The linear FE formulation of the 6-DOF per node triangular shell element is based on the work of Militello & Felippa (1991) and Alvin et al. (1992). All ROM variables for the static case can thus be computed using the Eqs. 2.9 – 2.11. The required external inputs are only the stiffness tensors, which are computed using the strain energy-based approach, and the load matrix $\boldsymbol{F}$, which comprises the external force vector. The reader is referred to Liang (2013) for a comprehensive discussion on the K-N method and the computation of higher order stiffness tensors. In the

present work, the process has been implemented in MATLAB for utilisation in the subsequent studies.

2.2. GEOMETRICALLY NONLINEAR ANALYSIS

Preliminary studies have been conducted to assess the performance of the K-N method in nonlinear static analyses. In these studies, the ROM is initially computed in the undeformed state of the structure. Two representative test cases are presented here: a beam clamped on both ends (C-C) and a clamped-free configuration (C-F). In the C-C test case, a concentrated point force is applied at the mid-point of the beam along the span. A load-deflection curve is obtained by incrementally increasing the load for both linear and nonlinear cases using the K-N method. For comparison, the same analyses are also conducted in the SOL400 module of MSC NASTRAN. The dimensions of the beam are defined as: length l = 20 m, width w = 0.01 m and depth d = 0.1 m. A maximum load of up to 1000 N is applied on the structure. The isotropic material properties are defined as follows: elastic modulus E = 69 GPa, Poisson's ratio ν = 0.3, and density ρ = 2840 kg/m^3.

Figure 2.1 shows a comparison between the K-N method and NASTRAN results. The significant difference of 72% between the linear and nonlinear displacements indicates a high degree of nonlinearity at the maximum load of 1000 N. Overall, the K-N method is able to trace the load-deflection path predicted by Nastran with a maximum error of 2.1%. The cubically nonlinear model is well-suited for such structures where the coupling between transverse bending and in-plane stretching is the dominant source of nonlinearity.

Next, a similar analysis is conducted in the C-F configuration. The beam dimensions are defined as: length l = 0.55 m, width w = 0.06 m, and depth d = 2.25 mm. The isotropic material properties are defined as follows: elastic modulus E = 71 GPa, Poisson's ratio ν = 0.33, and density ρ = 2700 kg/m^3. A concentrated, non-follower force is applied at the free end of the cantilever. A load-deflection curve is constructed, and a comparison, similar to the C-C case, is done with NASTRAN predictions.

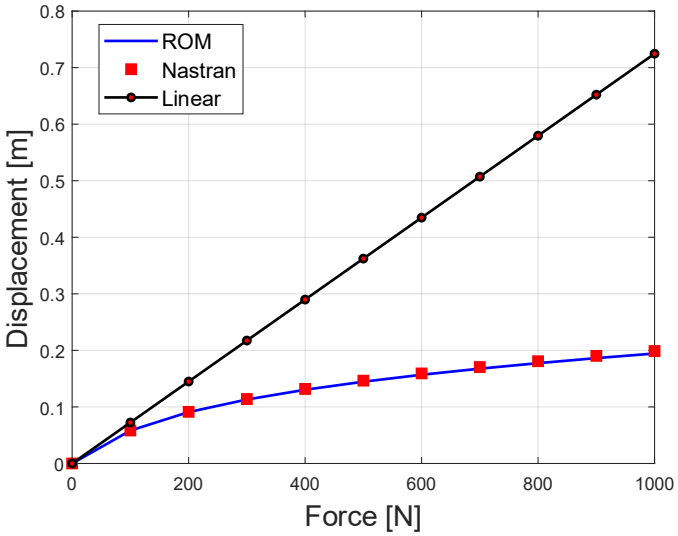

Figure 2.1 Comparison of the load-deflection curve of the C-C beam with Nastran nonlinear solution

Figure 2.2 shows the comparison of the load-deflection path of the cantilever beam with a maximum applied load of 70 N. Similar to the first case, the difference between the linear and nonlinear responses shows a high degree of nonlinearity at the applied maximum load. The results from the K-N method show that the solution begins to deviate from the reference nonlinear results at around 15 N, where the nonlinearity is comparatively weak. As the load is incremented, this deviation increases progressively, resulting in a very large solution error (75%) at the

maximum load. These results show that when the ROM is constructed only in the initial equilibrium state, it is insufficient for tracing the nonlinear load-deflection equilibrium path.

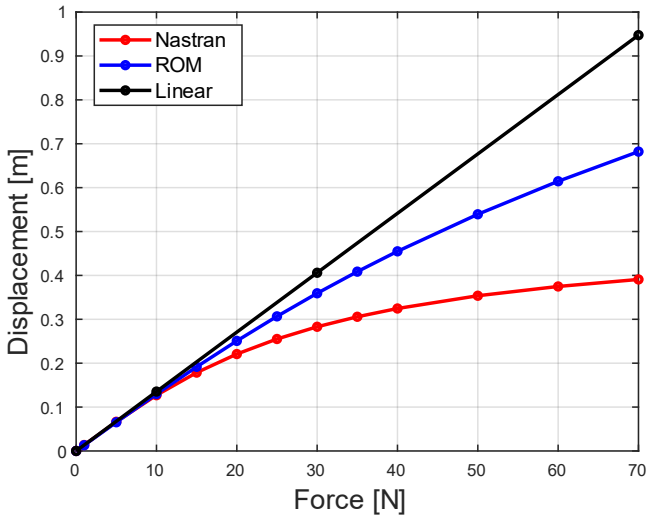

Figure 2.2: Comparison of the load-deflection curve of the cantilever beam with the NASTRAN nonlinear solution

It has been discussed in Section 1.1, that the foreshortening effect is a major factor influencing the accuracy of ROM across the load-deflection path. The change in force position due to the large rotation and bending of the beam causes a redistribution in the internal forces. Moreover, the geometry changes caused due to the large deformations influence the stiffness. Therefore, the K-N method requires modifications for application to large deflection analysis of cantilevers.

In the present work, a ROM updating strategy is utilised with the objective of improving its performance for large deflection analyses. As discussed in Section 1.1, an FE analysis follows a predictor-corrector approach with force, displacement or work correction to accurately obtain

the nonlinear displacement response. The ROM is an approximation of the FE model; therefore, it is presumable that a solution approach similar to that of an FE analysis can improve the accuracy of the ROM. A strategy resembling FE solvers is therefore adopted for solving the ROM. Figure 2.3 depicts a schematic of the process implemented for large deflection analyses of cantilevers.

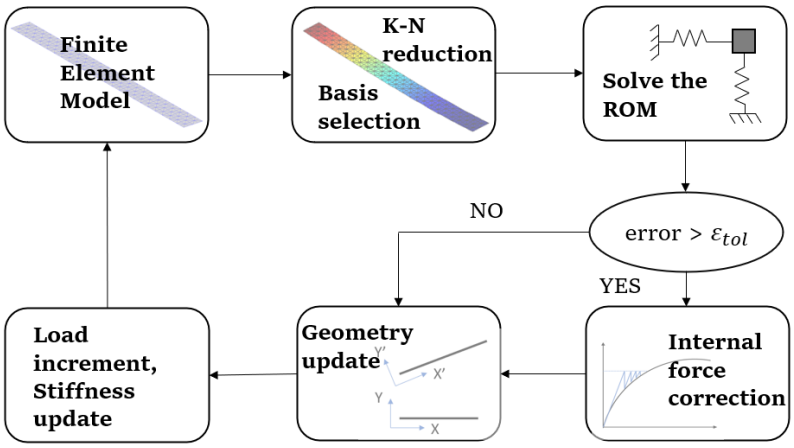

Figure 2.3: Schematic of the ROM update process for large deflection analyses

The process begins with the computation of the ROM variables in the initial equilibrium state of the structure, using the equations described in Section 2.1. The external force vector is chosen as the reduction basis which results in 1-DOF ROM. Next, the solution of the generalised displacements is obtained using a polynomial solver. The real structural displacements are computed based on Eq. 2.4. An error check is performed by comparing the total internal forces to the applied external force. If this error is greater than a pre-defined tolerance ε_{tol}, a force correction is performed using the Newton method. The nodal coordinates of the geometry are then updated using the current displacements. This

is a mandatory step since a new set of ROM variables is computed in the new equilibrium state of the structure. The process is repeated until the maximum load is reached. When compared to FE analyses, the major benefit of this approach is the utilisation of a nonlinear predictor, i.e., the cubic ROM equations solved to obtain the displacements. This allows for comparatively larger load increments to be applied without deviating significantly from the true equilibrium path.

2.3. NUMERICAL STUDIES

Several verification cases have been considered to evaluate the performance of the ROM when integrated into an updating procedure, described in Section 2.2. This Section presents the results of the numerical studies for the considered test cases. The following five examples considered with varying complexity are: (1) beam roll-up under applied tip moment, (2) cantilever plate subjected to tip shear force, (3) I-section cantilever with distributed loading and follower forces, (4) comparison to experimental results of a highly flexible wing, and (5) a high-aspect-ratio wingbox structure.

2.3.1. Cantilever beam roll-up under applied tip Moment

The classical benchmark problem of beam roll-up is first considered as a verification case. In this example, a cantilever beam subjected to an applied tip moment rolls into a perfect circular shape. In the present work, the structural dimensions are based on the benchmark case presented by Sze et al. (2004), where all parameters were defined in dimensionless form. For consistency, the SI units are considered in the analysis discussed here. The model parameters are: elastic modulus E = 1.2 MPa, length l = 12 m, cross-section width b = 1 m, height h = 0.1 m,

and Poisson's ratio $\upsilon = 0$. A pure bending moment is applied at the tip of the cantilever with a magnitude of $M = 50\pi/3$ N-m. The applied moment is increased from zero to the maximum with fixed intermediate load steps. The analysis is conducted using a beam element formulation with discretisation into 20 elements.

Figure 2.4 depicts a comparison of the in-plane displacements in the axial direction and out-of-plane displacements, computed at different applied moment magnitudes, with the reference analytical solution obtained from Sze et al. (2004). A good agreement is obtained with respect to the reference solution for the entire range of applied moments. A deviation of only 0.27% from the reference results occurs at the maximum load. The error is computed as the ratio of the norm of the vector comprising the error measure in x- and y-directions to the norm of the tip deflection vector.

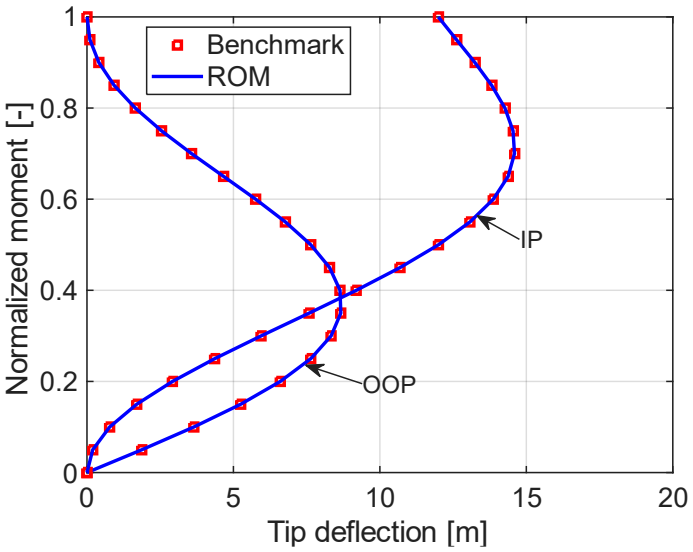

Figure 2.4: Comparison of in-plane displacements (IP) and out-of-plane displacements (OOP) to the benchmark (Sze et al., 2004) for the applied moment case

Figure 2.5 illustrates the beam deflection at various load intervals, ultimately resulting in the complete roll-up of the beam, where the free end comes into contact with the fixed end of the cantilever after bending into a circular form. Although the example simulates extremely large deflections, it is relatively easier to model than a case where a transverse tip force is applied since the applied moment creates a uniform moment distribution across the span, which does not vary with the increasing deflection. According to the Euler-Bernoulli beam theory, the moment *M* has a linear relationship with the curvature κ. This indicates that for an applied tip moment, the curvature is constant across the beam length. Furthermore, no corrector step is required in obtaining this solution, which makes the process considerably faster. The maximum moment is applied using 50 equal load increments; therefore, the solution requires updating the ROM 50 times. It is not possible to obtain this solution utilising the K-N method if no ROM updating strategy is applied. The simulation time for the analysis is 0.73 s, while the ROM construction requires 2.8 s.

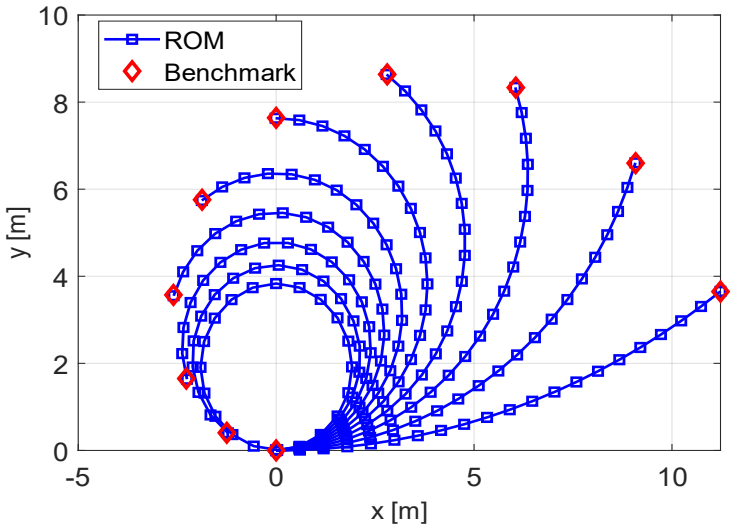

Figure 2.5: Incremental beam deflection at different load steps for the applied moment case

Additionally, it is noted that the number of load increments, and by extension, the number of ROM updates, has an influence on solution accuracy. By reducing the number of load increments to 30, a relatively larger error of 0.77% is obtained. This, however, reduces the simulation time to 0.42 s. Similarly, if the load increments are increased to 70, the error reduces to 0.13 % and the simulation time increases to 0.95 s.

2.3.2. Cantilever flat plate with an applied tip shear force

The second verification case involves a cantilevered flat plate subjected to a transverse bending force. The model complexity is increased in two ways in this case: a greater number of FE nodes is utilised with the application of shell elements, and a shear force is applied, resulting in a varying bending moment across the span. The problem setup is similar to the cantilever example discussed in Section 2.2, where large errors are observed when ROM updates are not conducted. The geometrical details and reference data are obtained from Sze et al. (2004). The discretised FE model comprises 320 elements. The model parameters are defined as follows: elastic modulus E = 1.2 MPa, length l = 10 m, cross-section width b = 1 m, height h = 0.1 m and Poisson's ratio $\upsilon = 0$. The maximum applied force is $P = 4EI / l^2$, where I is the area moment of inertia. The force is applied using 10 increments per load step, effectively as 200 increments.

Contrary to the previous verification case, the moment-curvature relationship is no longer linear. According to the direct nonlinear solution approach for a beam subjected to non-follower force (Morsch et al., 2009), the governing equation being solved for large deflections is of the form:

$$\frac{d^2\theta}{ds^2} = \frac{-F\cos\theta}{EI} \tag{2.18}$$

where *s* is the beam length, *E* is the elastic modulus, *I* is the area moment of inertia, and θ is the rotation angle.

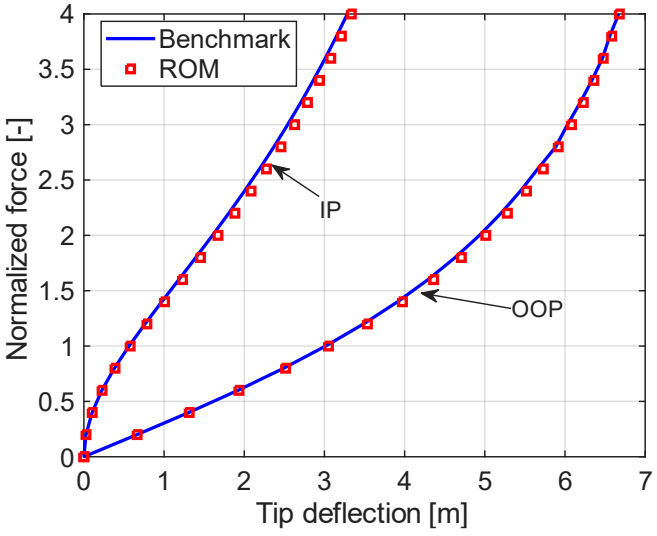

Figure 2.6: Comparison of in-plane displacements (IP) and out-of-plane displacements (OOP) to the benchmark (Sze et al., 2004) for the applied shear force case

The load-deflection paths showing both the in-plane displacement in the axial direction and out-of-plane deflection are plotted in Fig. 2.6. The results are in good agreement with the reference benchmark solution, with an error of 1.4% in tip deflection at the maximum applied load. The total computational time, including ROM formulation time, for this load case with 10 increments per load step, is approximately 8.4 s. The error margins can be reduced by increasing the load increments. For example, with 20 load increments, the error is reduced to only 0.8% with a

computational time of 17.2 s. The pre-processing time required to obtain the ROM is comparatively higher since the initial FE model comprises 1,230 DOFs.

2.3.3. I-section cantilever beam with follower force

In this verification case, the K-N method is compared against the Modal Rotation Method (Drachinsky and Raveh, 2020), which is briefly discussed in Section 1.1. The structural model is an I-section cantilever beam for which the geometrical and material definitions are obtained from (Drachinsky and Raveh, 2020). The cantilever beam, which is modelled using 10 planar beam elements, has a length l = 30 m, total cross-section area A = 0.0152 m^2, and an area moment of inertia I = 2.69×10^{-5} m^4. The force is applied as a uniformly distributed load (UDL) of 1250 N/m. Additionally, the follower force effect is considered so that the nodal loads remain normal to the surface in any state of deflection. The nodal forces are therefore resolved into sine and cosine components based on the nodal rotation angle at the points of force application.

Figure 2.7 shows a comparison of the beam deflection obtained using the K-N method and the MRM. The results are in good agreement, with a maximum deviation of 0.83% at 100% loading. The beam rotation is beyond 90 degrees from the reference configuration. The load is applied in 40 fixed incremental steps, and the simulation requires a total time of 0.63 s with a ROM formulation time of about 2.1 s. A force correction is performed using a tolerance of 0.01, which requires a total of 309 iterations. Variations in the solution are seen based on the number of load increments chosen. Simulation time reduces to 0.28 s if 18 load increments are applied; however, the error increased to 2.4%. At lower loads, the solution is obtained faster since a smaller number of load increments is sufficient. At 56% loading, the solution can be obtained in

0.07 s with a solution error of 3.01% and only four load increments. Variations in the errors and simulation times are shown in Fig. 2.8.

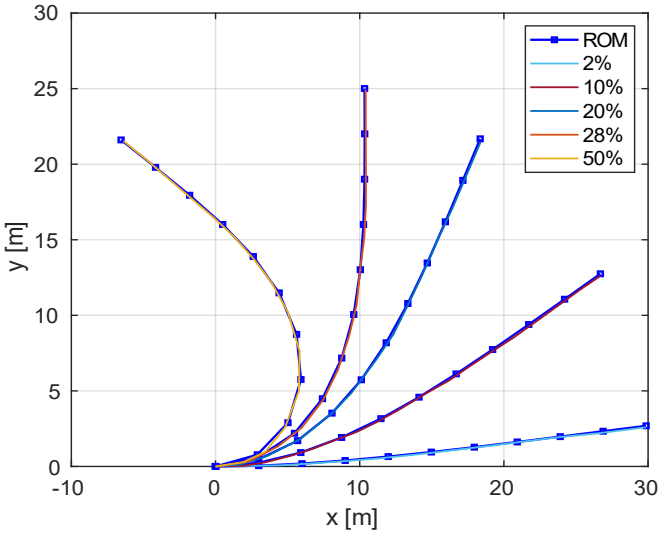

Figure 2.7: I-section beam deflection compared to the results from MRM at different load fractions

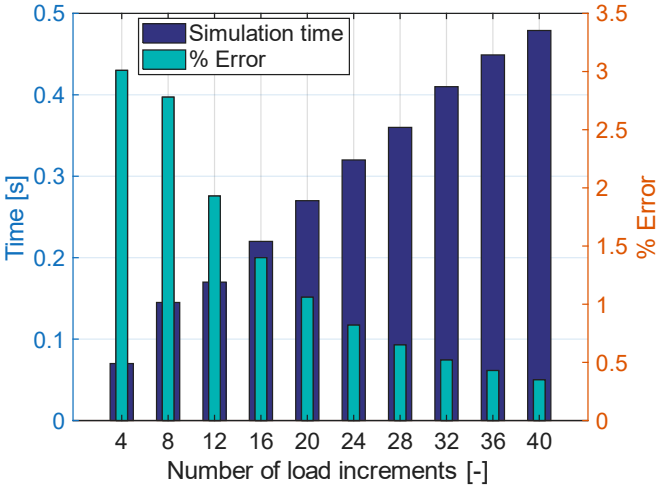

Figure 2.8: Influence of the number of load intervals on the simulation time and % error in the solution at applied UDL = 750 N/m

2.3.4. Validation against experimental data

Next, the K-N method is validated against experimental data. The intended application of this method is for highly flexible wing structures. Accordingly, the experiment conducted on the Pazy wing is chosen as a reference. The design, analysis and testing of the Pazy wing have been presented by Avin et al. (2022). The wing is constructed with a NACA 0018 airfoil whose chord length is 100 mm and span of 550 mm. The wing comprises a central rectangular plate, which is made of Aluminium 7075, and a surrounding frame structure made of Nylon 12. The present analysis is conducted using an equivalent beam model developed by Riso and Cesnik (2021). The beam has a varying cross-sectional area and inertia properties, which are defined in Appendix II**.** In the experiments, the wing tip was loaded using weights ranging from 0 to 3 kg.

Figure 2.9 shows a comparison of the transverse tip deflection obtained using the K-N method, experimental measurements and full FE analysis in MSC NASTRAN. Additionally, results are obtained using the K-N method with the ROM formulated only for the initial undeformed wing. At the maximum load, tip deflection of around 45% of the span is observed. The results obtained using the K-N method are well matched with the experiments, with a maximum deviation of -2.5%. There is a perfect agreement between NASTRAN results and the K-N method when internal force correction is applied with an error tolerance of 0.01. However, when comparing the number of iterations needed for convergence, NASTRAN requires 985 iterations, while the K-N method requires only 54 iterations to trace the entire load-deflection path. The reduction in the number of iterations aligns with the discussions in Section 2.2 regarding the benefit of using a predictor with a cubic nonlinear

model. If the ROM is only constructed in the undeformed state, an almost linear solution is observed. This is explainable by the fact that the nonlinear terms in this model are insignificant in magnitude when the ROM is constructed in the undeformed state.

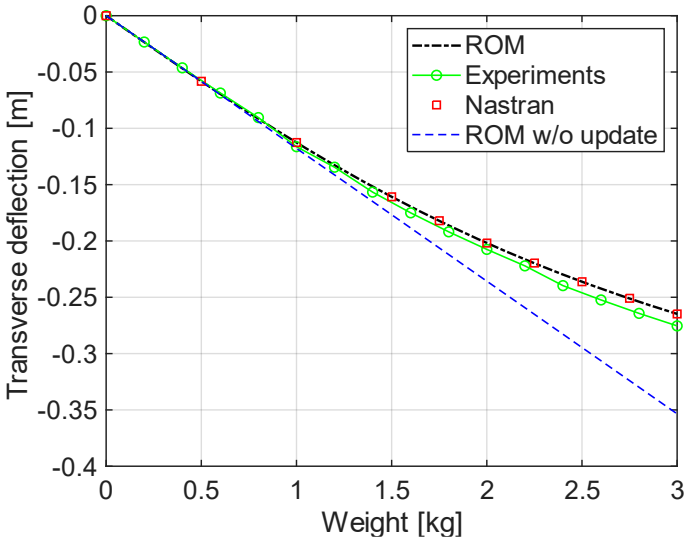

Figure 2.9: Transverse tip deflections of the Pazy wing at different loads compared to experimental results

2.3.5. Generic high-aspect-ratio wingbox structure

For the final verification case, the K-N method is applied to a slender 3-D wingbox model. The geometry definition is similar to the wingbox described by Ritter (2019), albeit with the simplification that the same material properties are defined at all wing sections. The model features anisotropic material definition, where the elements of the property matrix are: $G_{11} = G_{22} = 79.15$ GPa, $G_{12} = 26.91$ GPa, and $G_{33} = 26.12$ GPa. The wingbox construction comprises an assembly of skin panels, spars and ribs, each with varying thickness from root to tip. Figure 2.10 illustrates the wingbox construction, along with its thickness

distribution. The FE model shown comprises 8,660 triangular shell elements.

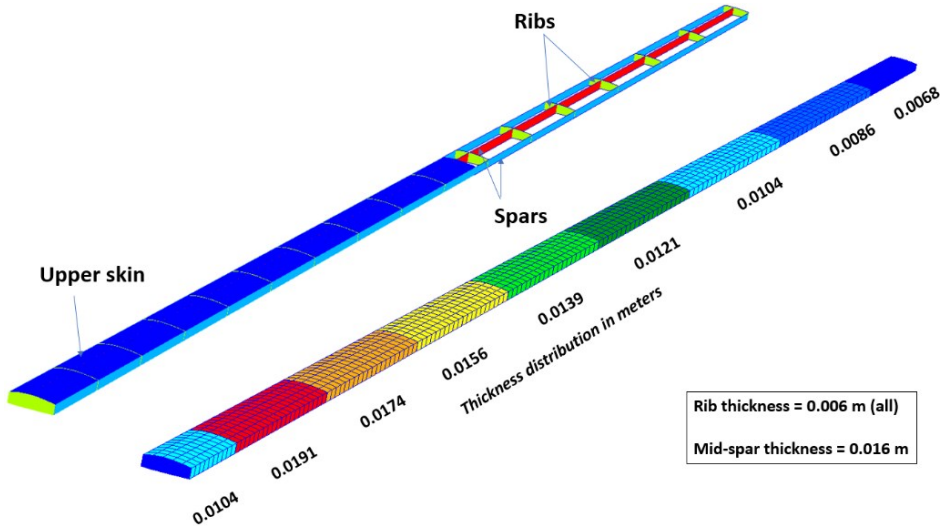

Figure 2.10: Wingbox construction and thickness distribution along the half-span

The analysis is conducted with a distributed load acting along the 40% chord line, which consists of 160 unconstrained node points. At each of these node points, a transverse force of 500 N is applied, resulting in a total transverse force of 80,000 N. Additionally, a 2,000 N-m torsional moment is applied to each of the 160 node points to enforce a twisting motion. All degrees of freedom at the node points forming the root profile are fully constrained. Figure 2.11 shows the stepwise normalized deflection data along the reference line at the 40% chord position on the upper skin panel as a percentage of the semi-span of the wingbox. The peak transverse tip deflection obtained is 9.21 m, which is approximately 46% of the semi-span. A comparison is made to the results obtained from SOL400 of MSC NASTRAN, and a deviation of 1.45% is found. The error is measured as the ratio of the norm of the vector comprising the error

measure in the global x, y, and z- directions to the norm of the reference tip deflection vector.

The rotation angles in transverse bending θ_1 and twist θ_2 are also compared in the analysis. The variation of these angles is shown in Figures 2.12 and 2.13, respectively. In alignment with deflection results, the bending angle θ_1 is well matched with the reference results. The twist angle θ_2 shows a higher deviation with an error of approximately 4.6% at the tip. There is also, however, some deviation seen in the linear results, which indicates that the variations are arising due to the different FE formulations used.

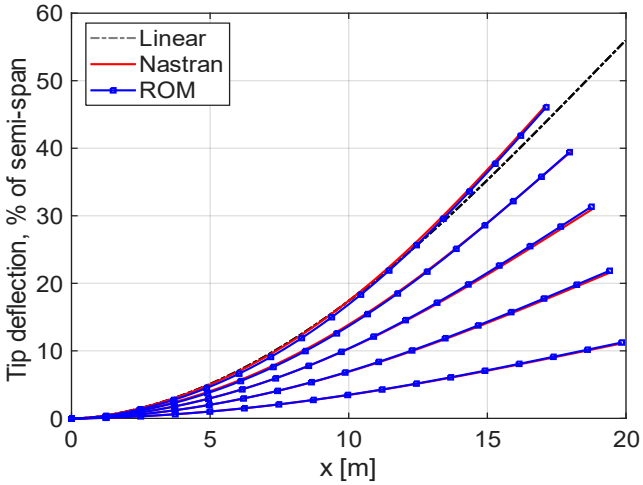

Figure 2.11: Deflection of the reference line (40% chord position) on the upper skin of the slender wingbox

Since the FE model comprises 24,582 DOFs, the ROM formulation time is considerably higher and requires about 45.7 s for the full run. The total computation time differs depending on the number of load increments applied. In this model, 11 increments are applied to get

a comparable response to NASTRAN. The solution obtained from NASTRAN required a total of 395 iterations and 42 s for completion.

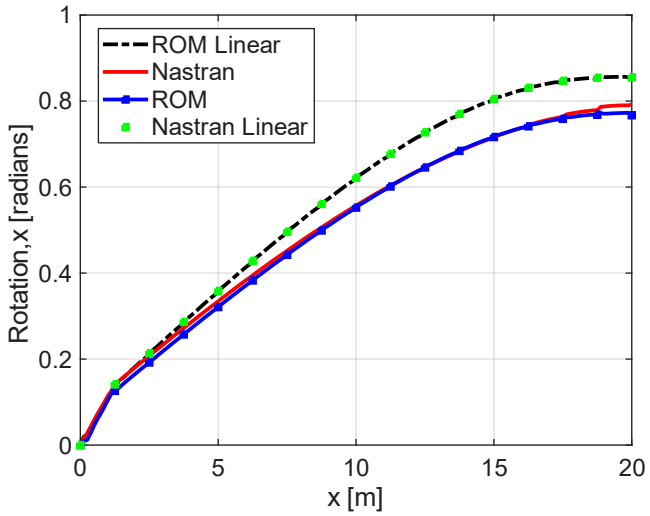

Figure 2.12: Rotation angle θ_1 due to transverse bending, comparison to NASTRAN results

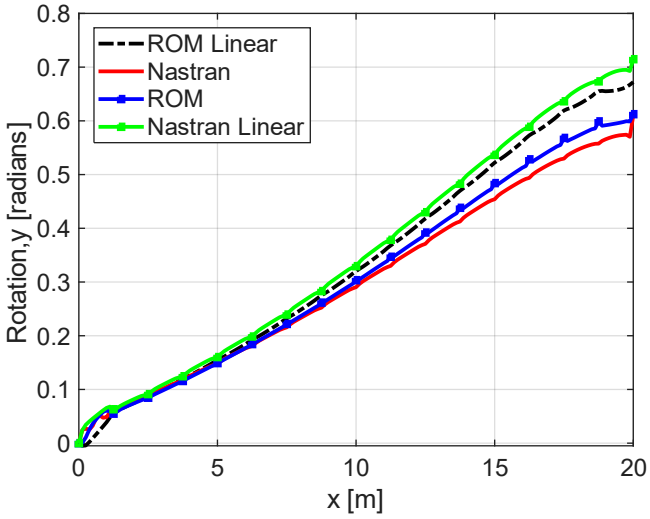

Figure 2.13: Rotation angle θ_2 due to twist, comparison to NASTRAN results

It is inferred that for FE models comprising a large number of DOFs, the time required for ROM formulation has a contradictory effect on the efficiency of the analyses. The interesting aspect is that, regardless of the initial size of the FE model, a 1-DOF reduced-order model can be obtained when utilising the K-N method.

2.4. CONCLUSIONS

The numerical formulation of the K-N method has been discussed. Preliminary studies have been conducted to assess the performance of the K-N method for large deflection problems. It has been observed that since the K-N method does not inherently account for foreshortening effects and nonlinear curvature in cantilevers, a ROM obtained in an undeformed state is insufficient to capture the entire load-deflection path. A strategy for updating the ROM integrated in the process to account for the foreshortening effects. Various verification cases have been utilised to evaluate the ROM performance. For FE models with a low number of DOFs, it is efficient to compute and update the ROM multiple times. However, for FE models with a larger number of DOFs, as in Section 2.3.5, construction of the ROM is time-consuming. As a result, the total ROM computation time may overshoot the total analysis time required for a full-order model. The approach becomes progressively more beneficial if repeated analyses for the same model are required. Overall, the results are found to be sufficiently accurate in all test cases. The results show that the K-N method can be utilised effectively for large deflection analyses when the ROM is updated with increasing deflections.

3

NONLINEAR DYNAMIC ANALYSES OF HIGHLY FLEXIBLE WINGS

In the discussions presented in Chapter 1, it has been highlighted that changes in eigenfrequencies of wing structures due to large amplitude static deflections are of interest since they affect the dynamic characteristics of the structure. Similarly, large amplitude dynamic motion can also influence the eigenfrequencies. However, this has been largely unexplored in relation to wing structures. Prior numerical and experimental investigations on the large amplitude dynamics of beam

This Chapter is based on the publication: Sinha, K., Alijani, F., Krüger, W. R., & De Breuker, R. (2025). Nonlinear dynamics of wing-like structures using a momentum subspace-based Koiter-Newton reduction. *Journal of Sound and Vibration*, *596*, 118747.

structures have been conducted using inextensibility constraints, which are limited to cases where the cross-sectional area is significantly smaller than the beam length Crespo da Silva (1978a, 1978b). The geometrically exact beam theory provides a more generic kinematic description and is found to be effective in such problems (Simo and Vu-Quoc, 1991; Vu-Quoc and Deng, 1995). Methodologies such as the Modal Derivatives approach (Jain et al., 2017) and the Spectral Submanifold approach (Jain and Haller, 2021) are applicable to finite element models and have been previously utilised for investigating the nonlinear dynamics of wing structures.

The Koiter-Newton method, as described in Chapter 2, has been developed for nonlinear static problems. The objective of this Chapter is to exploit the procedures developed in Chapter 2 and present a methodology for investigating large amplitude dynamics of wing structures. The remainder of the Chapter is divided as follows: Section 3.1 introduces the momentum subspace formulation (Sinha et al., 2020), an adaptation of the Koiter-Newton method, which is more suitable for nonlinear dynamics problems, Section 3.2 introduces a procedure which can be applied for investigating large amplitude dynamics of cantilevers, Section 3.3 presents numerical studies for validating the proposed methodology, and finally, the conclusions are presented in Section 3.4.

3.1. MOMENTUM-SUBSPACE METHOD

In Chapter 2.1, an overview of the Koiter-Newton method for constructing a ROM in nonlinear static analyses has been presented. This model utilises the external force vector as the reduction basis. The momentum subspace formulation (Sinha et al., 2020), discussed in Section 3.1.1, extends the K-N method to nonlinear dynamic analyses. In

Section 3.1.2, a discussion is presented on the choice of linear eigenmodes as the reduction basis in the dynamics problem.

3.1.1. Theoretical formulation

The D'Alembert's principle serves as the foundation for the adaptation of the ROM from statics to dynamics. Considering a free and undamped vibration problem, the governing equation of motion, in a form similar to Eq. 2.3, can be described as:

$$\boldsymbol{K}\,\boldsymbol{u} + \boldsymbol{Q}\,\boldsymbol{u}\,\boldsymbol{u} + \boldsymbol{C}\,\boldsymbol{u}\,\boldsymbol{u}\,\boldsymbol{u} = -\dot{\boldsymbol{p}} \tag{3.1}$$

where $\dot{\boldsymbol{p}}$ is the time derivative of momentum.

An assumption is introduced for the momentum, which is described as:

$$\boldsymbol{p} = \boldsymbol{M}\,[\boldsymbol{\Phi_1}\ \boldsymbol{\Phi_2}\ \ldots\ \boldsymbol{\Phi_n}]\,\boldsymbol{\pi} \tag{3.2}$$

where $\boldsymbol{M}$ is the mass matrix, $\boldsymbol{\Phi_n}$ is the eigenvector of the n^{th} mode, and $\boldsymbol{\pi}$ is a vector of momentum amplitudes and the momentum variable in the reduced order model. In a more general form, the Eq. 3.2 is written as $\boldsymbol{p} = \boldsymbol{P\pi}$, where $\boldsymbol{P}$ is the basis matrix. The assumption implies that the momentum of the system lies in a linear subspace of the eigenmode shapes, and by extension, the time derivative of the momentum also lies in the same subspace. The number of eigenvectors chosen to define the basis matrix determines the size of the ROM. The stiffness tensors corresponding to the ROM can be obtained in a form similar to Eqs. 2.9 – 2.11 and are given by:

$$\begin{bmatrix} \boldsymbol{K} & -\boldsymbol{P} \\ -\boldsymbol{P}' & \boldsymbol{0} \end{bmatrix} \begin{Bmatrix} \boldsymbol{u}_\alpha \\ \bar{\boldsymbol{K}}_\alpha \end{Bmatrix} = \begin{Bmatrix} \boldsymbol{0} \\ -\boldsymbol{E}_\alpha \end{Bmatrix} \tag{3.3}$$

$$\begin{bmatrix} \boldsymbol{K} & -\boldsymbol{P} \\ -\boldsymbol{P}' & \boldsymbol{0} \end{bmatrix} \begin{Bmatrix} \boldsymbol{u}_{\alpha\beta} \\ \bar{\boldsymbol{Q}}_{\alpha\beta} \end{Bmatrix} = \begin{Bmatrix} -\boldsymbol{Q}(\boldsymbol{u}_\alpha, \boldsymbol{u}_\beta) \\ \boldsymbol{0} \end{Bmatrix} \tag{3.4}$$

$$\bar{C}_{\alpha\beta\gamma\delta} = \boldsymbol{C}(\boldsymbol{u}_\alpha, \boldsymbol{u}_\beta, \boldsymbol{u}_\gamma, \boldsymbol{u}_\delta) - \frac{2}{3}\left[\boldsymbol{u'}_{\alpha\beta}\,\boldsymbol{K}\,\boldsymbol{u}_{\delta\gamma} + \boldsymbol{u'}_{\beta\gamma}\,\boldsymbol{K}\,\boldsymbol{u}_{\delta\alpha} + \boldsymbol{u'}_{\gamma\alpha}\,\boldsymbol{K}\,\boldsymbol{u}_{\delta\beta}\right] \tag{3.5}$$

From Eqs. 3.3 - 3.5, it is evident that the primary difference, compared to the ROM formulation in the static case, is the replacement of the load matrix $\boldsymbol{F}$ by the matrix $\boldsymbol{P}$. The validity of this comparable formulation has been previously discussed by Sinha et al. (2020).

In addition to the stiffness tensors, a reduced mass matrix is required to define the ROM equations. Consider the expression for total kinetic energy for the full order model in terms of the momentum $\boldsymbol{p}$:

$$T = \frac{1}{2}\,\boldsymbol{p}'\boldsymbol{M}^{-1}\boldsymbol{p} \tag{3.6}$$

Replacing $\boldsymbol{p}$ by Eq. 3.2, we obtain:

$$T = \frac{1}{2}\,\boldsymbol{\pi}'(\boldsymbol{\Phi}'\boldsymbol{M}\,\boldsymbol{\Phi})\boldsymbol{\pi} \tag{3.7}$$

where $\boldsymbol{\Phi}$ is a modal matrix comprising *n* eigenvectors.

Since the kinetic energy of the full-order and reduced-order models must be the same, by comparison, the reduced mass matrix $\bar{\boldsymbol{M}}$ is obtained as:

$$\bar{\boldsymbol{M}} = \ (\boldsymbol{\Phi}'\boldsymbol{M}\,\boldsymbol{\Phi})^{-1} \tag{3.8}$$

The equation of motion of free and undamped vibrations can be written as:

$$\bar{\boldsymbol{M}}\ddot{\boldsymbol{\xi}} + \bar{\boldsymbol{K}}\boldsymbol{\xi} + \bar{\boldsymbol{Q}}\boldsymbol{\xi}\boldsymbol{\xi} + \bar{\boldsymbol{C}}\boldsymbol{\xi}\boldsymbol{\xi}\boldsymbol{\xi} = \mathbf{0} \tag{3.9}$$

The reduced damping matrix is evaluated by assuming a quadratic damping model, where the dissipation energy D_e is defined as:

$$D_e = \frac{1}{2}\,\dot{\boldsymbol{u}}'\boldsymbol{D}\,\dot{\boldsymbol{u}} \tag{3.10}$$

Rewriting $\dot{\boldsymbol{u}}$ in terms of momentum $\boldsymbol{p}$ and utilising Eq. 3.2, the dissipation energy can be expressed as:

$$D_e = \frac{1}{2}\,\boldsymbol{\pi}'\left(\boldsymbol{P}'\boldsymbol{M}^{-1}\boldsymbol{D}\,\boldsymbol{M}^{-1}\,\boldsymbol{P}\right)\boldsymbol{\pi} \tag{3.11}$$

where $\boldsymbol{D}$ is the damping matrix. In the present work, for the full order model, $\boldsymbol{D}$ is assumed to be Rayleigh damping of the form $\boldsymbol{D} = \alpha\boldsymbol{M} + \beta\boldsymbol{K}$.

The reduced damping matrix is obtained from Eq. 3.11 as:

$$\bar{\boldsymbol{D}} = \bar{\boldsymbol{M}}\left(\boldsymbol{P}'\boldsymbol{M}^{-1}\boldsymbol{D}\,\boldsymbol{M}^{-1}\,\boldsymbol{P}\right)\bar{\boldsymbol{M}} \tag{3.12}$$

Finally, the reduced-order external force vector $\boldsymbol{\phi}$ is obtained as:

$$\boldsymbol{\phi} = \boldsymbol{u}'_{\alpha}\,\boldsymbol{f}_{ex} \tag{3.13}$$

The reduced-order model of a forced and damped vibration is defined as:

$$\bar{\boldsymbol{M}}\ddot{\boldsymbol{\xi}} + \bar{\boldsymbol{D}}\dot{\boldsymbol{\xi}} + \bar{\boldsymbol{K}}\boldsymbol{\xi} + \bar{\boldsymbol{Q}}\boldsymbol{\xi}\boldsymbol{\xi} + \bar{\boldsymbol{C}}\boldsymbol{\xi}\boldsymbol{\xi}\boldsymbol{\xi} = \boldsymbol{\phi}(t) \tag{3.14}$$

Eq. 3.14, solved using time integration schemes, provides the generalised displacements ξ. The real displacements are then obtained by the substitution of ξ in Eq. 2.4.

3.1.2. Note on the use of eigenmodes in the basis matrix

Linear eigenmodes are computed using the small-angle approximation; therefore, they do not contain information about in-plane displacements in large deflection motion. Developments of methods such as the Quadratic Manifold approach (Jain et al., 2017), which achieves improved accuracy through basis enrichment using higher-order mode derivatives, and the Extended Modal approach (Ritter, 2019), which also utilises higher-order mode derivatives, were necessary for this reason. It invites speculation whether the utilisation of NNMs in formulating ROMs instead of the linear modes is more pragmatic since the NNMs already carry the information of the nonlinear dynamic system. Kerschen et al. (2009) have comprehensively discussed the application of NNMs to large-scale engineering structures, where they also highlight the challenges related to the use of NNMs in formulating ROMs. The authors state that “the lack of orthogonality relations satisfied by NNMs complicates their exploitation as bases for model order reduction”. For the specific case of cantilevers, Shang-Rou et al. (2014) found in their investigations that linear modes are a good approximation for the NNMs up to 50% tip deflection, provided that the kinematics related to foreshortening effects are considered. This indicates that while the utilisation of linear modes in the reduction basis may be appropriate, the ROM requires re-evaluation in updated configurations to ensure that the foreshortening effect is accounted for. This, of course, also aligns with the approach utilised for the nonlinear static analyses.

3.2. METHODOLOGY FOR LARGE AMPLITUDE DYNAMICS

The discussions in Section 3.1.2 highlight the potential issues in utilising linear eigenmode-based model order reduction for investigating large amplitude dynamics. In Section 3.2.1, a methodology is proposed for incrementally updating the ROM within a time integration scheme while utilising linear eigenmodes in the reduction basis. The objective of the proposed method is to circumvent the limitations of such ROMs in large deflection problems. In Section 3.2.2, important considerations for using the proposed method are discussed.

3.2.1. ROM updating in time marching

Initial studies are conducted on a cantilever beam to assess the extent of applicability of the momentum subspace variant of the K-N method. The beam geometry and material properties are adopted from (Pany and Rao, 2002). The dimensions of the beam are: length l = 0.693 m, height h = 0.99 mm, and width b = 0.0254 m. The material properties of the beam are: elastic modulus E = 200 GPa, and density ρ = 7800 kg/m^3. The first modal frequency is found to be at 1.68 Hz. A concentrated tip force is applied at a frequency equal to the first modal frequency. The ROM is formulated once in the initial undeformed state. The load is applied until a steady state oscillation is reached, and a snapshot of the peak amplitude is captured. The load is then incremented, and the same process is repeated.

Figure 3.1 illustrates the peak amplitudes in the axial in-plane direction and the transverse direction, as the excitation force increases, compared to results from MSC NASTRAN SOL 400. Up to around 0.03

N applied force and tip deflection 29% of the beam length, comparable results are obtained from both methods, beyond which the K-N method overpredicts, and the error progressively increases as the applied load is increased. The method presented in Section 2.2 is therefore extended to the dynamics problem, where the ROM is reformulated at different states of deformation. A time domain dynamic analysis generally involves a large number of time steps, which makes it impractical to reformulate the ROM at each time step. The key idea is to utilise a ROM database based on the nonlinear static analyses using the method described in Section 2.2. The ROM database stores information about the ROM variables $\bar{\boldsymbol{L}}, \bar{\boldsymbol{Q}}, \bar{\boldsymbol{C}}$ required for obtaining the solution to the generalised displacements; the displacement fields $\boldsymbol{u}_{\alpha}, \boldsymbol{u}_{\alpha\beta}$ required to reconstruct the true displacements and the basis matrix used to formulate the ROM, which is also used in computing the reduced mass and damping matrices. Additionally, the ROM database contains information about the range of tip displacements for which the ROM variables remain valid.

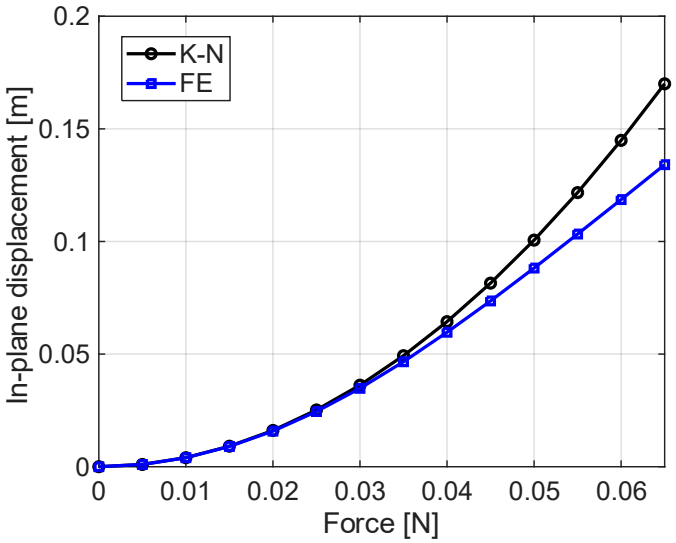

(a)

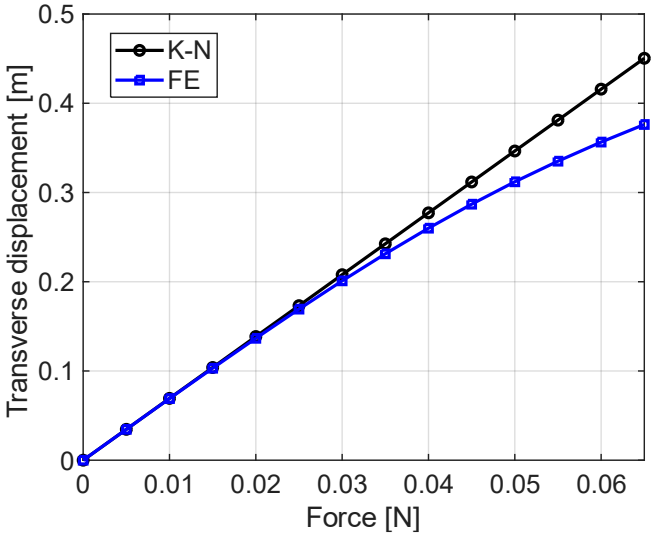

(b)

Figure 3.1: Snapshot of peak amplitude in steady state at different excitation loads compared to FE results (a) axial in-plane displacement, (b) transverse displacement

Figure 3.2 illustrates the procedure for conducting dynamic analyses of cantilevers undergoing extremely large amplitude dynamic motion. Broadly, the flow diagram can be distinguished into two parts, which are shown in green and blue. The green section of the flow diagram depicts the procedure for nonlinear static analysis, highlighting the preliminary steps where the ROM database is generated. The region of validity of the ROM is pre-determined based on the static deflections. The blue section of the flow diagram represents an incremental dynamic analysis procedure implemented within the framework of the Newmark-beta method.

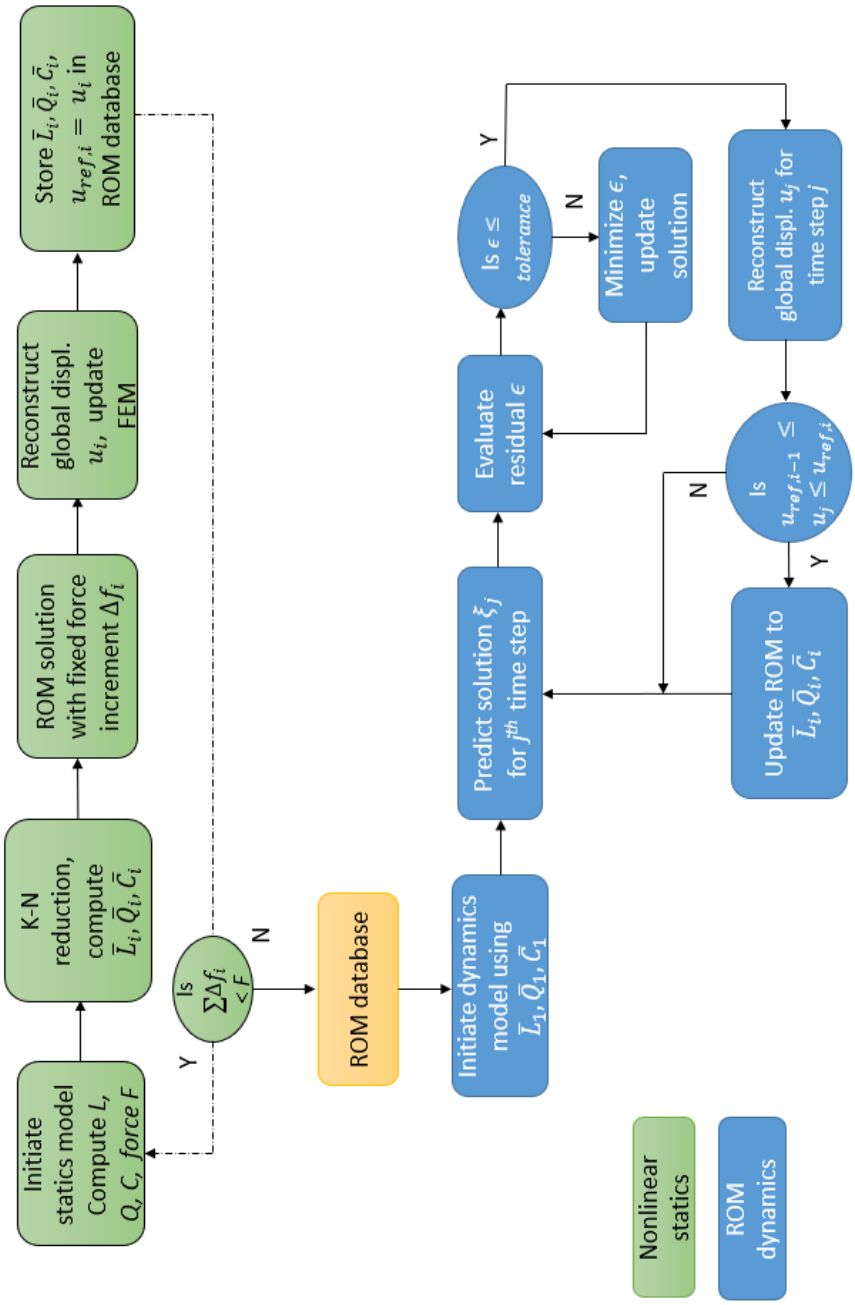

Figure 3.2: Momentum subspace variant of K-N method with incremental ROM update for modelling extremely large amplitude dynamics

The steps presented below describe the procedure within the dynamic analysis module.

Step 1: First, ROM parameters are computed based on the initial equilibrium state of the structure. The reference solution in the ROM subspace $\boldsymbol{\xi}_{ref}$ is set to zero. The ROM is constructed with various intermediate deformed states as references; therefore, for larger deflections, the $\boldsymbol{\xi}_{ref}$ must be updated accordingly so that the ROM solution is obtained with respect to the previous reference state.

Step 2: Begin with the Newmark time integration. Obtain a solution predictor for *j+1*th time step.

$$\boldsymbol{\xi}_{\mathrm{j+1}} = \boldsymbol{\xi}_{\mathrm{j}} + \dot{\boldsymbol{\xi}}_{\mathrm{j}}\,\Delta t + \ddot{\boldsymbol{\xi}}_{\mathrm{j}}\,(0.5-\beta)\Delta t^{\mathbf{2}} \tag{3.15}$$

$$\dot{\boldsymbol{\xi}}_{\mathrm{j+1}} = \dot{\boldsymbol{\xi}}_{\mathrm{j}} + \ddot{\boldsymbol{\xi}}_{\mathrm{j}}\,(1-\gamma)\Delta t \tag{3.16}$$

$$\ddot{\boldsymbol{\xi}}_{\boldsymbol{j+1}} = \mathbf{0} \tag{3.17}$$

Step 3: Evaluate the force residual as the difference between the total internal force and the applied external force. Compute error ε from the residual and the applied load increment.

Step 4: If the error is greater than a pre-defined tolerance, update the solution using a solution corrector:

$$\boldsymbol{\delta} = \boldsymbol{\xi}_{\mathrm{j+1}} - \boldsymbol{\xi}_{\boldsymbol{ref}} \tag{3.18}$$

$$\Delta\boldsymbol{\xi} = \left[\frac{\overline{\boldsymbol{M}}}{\beta\,\Delta t^2} + \frac{\gamma\overline{\boldsymbol{D}}}{\beta\,\Delta t} + \overline{\boldsymbol{K}} + \overline{\boldsymbol{Q}}\,\boldsymbol{\delta} + \overline{\boldsymbol{C}}\,\boldsymbol{\delta\delta}\right]^{-1}\varepsilon \tag{3.19}$$

$$\xi_{j+1} = \xi_{j+1} + \Delta\xi, \qquad (3.20)$$
$$\dot{\xi}_{j+1} = \dot{\xi}_{j+1} + \frac{\gamma\,\Delta\xi}{\beta\,\Delta t}, \quad \ddot{\xi}_{j+1} = \ddot{\xi}_{j+1} + \frac{\Delta\xi}{\beta\,\Delta t^2}$$

Step 5: Generalised displacements are converted to the real displacements.

Step 6: Check if the displacement limits for which the chosen ROM variables are valid have been exceeded. If yes, update the reference equilibrium state and the corresponding ROM variables. Continue to the next time step and repeat until the total simulation time is reached.

Note that ROM databases should be individually generated for loading and unloading cycles. Although the magnitudes of the ROM variables remain unchanged, their signs do change. Particular attention is also needed for the quadratic stiffness tensor $\overline{\boldsymbol{Q}}$. In the undeformed state $\overline{\boldsymbol{Q}}$ is approaching zero; however, in a deformed configuration, it is non-zero and contributes to the asymmetrical response from the deformed equilibrium state. Therefore, it is beneficial to generate individual databases for loading and unloading cycles.

3.2.2. Key considerations for dynamic analyses

- Due to the proposed updating methodology and dependence on the eigenmode shapes, which evolve with increasing deflections, the damping and mass matrices also vary. In the specific case where the reduction basis comprises mass orthonormalized eigenvectors, the reduced mass matrix is always normalised to an identity matrix. There is no explicit accountability of nonlinear inertia terms, which usually arise due to approximations in the formulations, for example, due to the beam inextensibility assumption (Belardinelli et al., 2017).

- Similar to the eigenmode-based linear ROM formulations, the choice of the eigenmodes in the reduction basis has an influence on the dynamic response. A ROM, therefore, formulated by omission of the torsion modes, cannot predict the twisting motion in the dynamic response.

- The ROM variables rely on the nonlinear static deflections in the preliminary steps for generating the ROM database. It is practical to compute a ROM database with sufficiently large deflections to ensure that the range of interest in dynamic analyses is encompassed. A ROM database computed for up to 50% tip deflection may be unsuitable for analyses where the deflections exceed this range.

3.3. NUMERICAL STUDIES

Three verification cases are presented in this Section: (1) First, a comparison is made to a full-order model where an FE analysis is conducted on a cantilever beam excited harmonically at the free end, (2) Next, a comparison is made to experimental results where frequency response curves are generated for a thin metal sheet under base excitation and, (3) Finally, nonlinear dynamic analyses are conducted on a wingbox structure to demonstrate the application to practical engineering structures.

3.3.1. Comparison to FE model

The steel cantilever beam described by Pany and Rao (2002) is chosen as the first test case. In this example, a time domain simulation is conducted, and the solution is compared to the results of SOL400 MSC NASTRAN. The dimensions of the beam are: length l = 0.6931 m, cross-section width b = 0.0254m and height h = 0.99 mm. The material

properties of the beam are: elastic modulus E = 200 GPa and density ρ= 7800 kg/m^3.

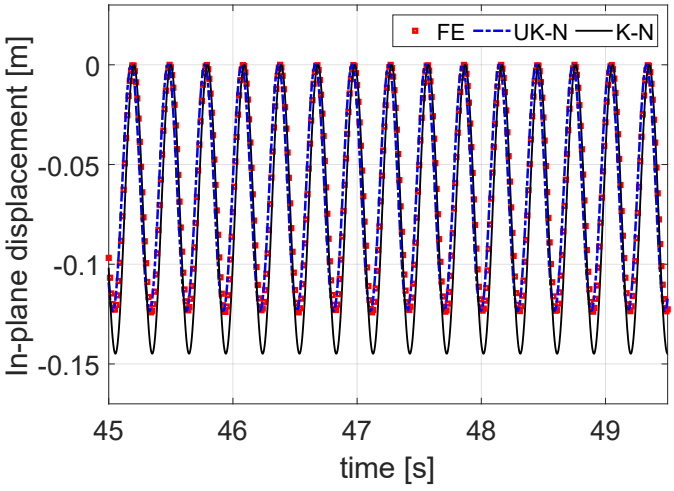

(a)

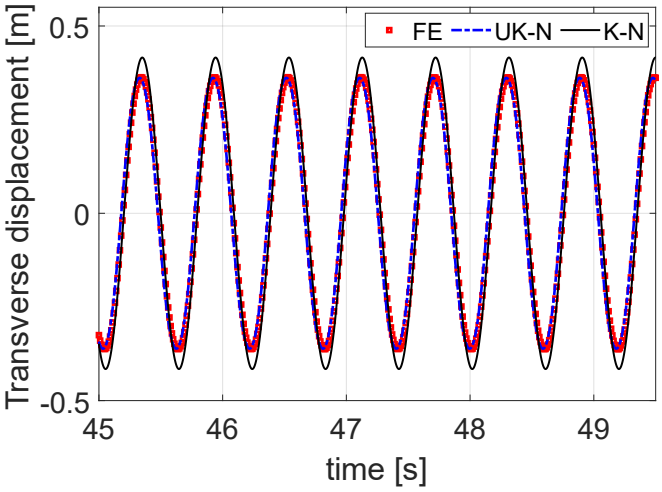

(b)

Figure 3.3: Comparison of time domain response for the steel cantilever beam (Pany and Rao, 2002) obtained using the ROM to FE results (a) in-plane displacement, (b) transverse displacements

A concentrated force of 0.06 N is applied on the tip with an excitation frequency equal to the first modal frequency. The first bending mode is found to be at 1.68 Hz. A mass proportional damping is applied with a damping ratio of 0.0189.

The initial FE model is constructed using 10 beam elements, which results in mass and stiffness matrices of the size 66 x 66. The solution reaches a steady state at around 25 sec; however, the analysis is conducted up to 50 sec. A comparison between the FE results and the ROM is shown in Fig. 3.3. The final few seconds of the analysis, after the steady state is reached, are shown for clarity. The ROM solution has been obtained using two methods: (1) utilising constant values of the ROM variables where the ROM data is generated only for the initial equilibrium state of the structure, shown as K-N in the results, and (2) utilising the ROM updating strategy proposed in Section 3.2, henceforth denoted as UK-N in the results. The chosen analysis parameters result in a maximum tip deflection of 0.364 m, which is approximately 54.5% of the beam length. In comparison, the K-N method without ROM updates predicts a maximum tip deflection of 0.416 m, which is a deviation of 14.4%. The UK-N performs comparatively much better and predicts a maximum transverse deflection of 0.362 m, which is a deviation of -0.56%. Similarly, the maximum axial in-plane displacement is 0.124 m according to the FE solution. The K-N method predicts a deviation of 16.7%, while the UK-N method only has a deviation of 0.4%. The linear analysis methods are obviously incapable of capturing these in-plane responses, nor can they predict the geometric stiffening effects.

The proposed ROM updating strategy results in a definite improvement in accuracy; however, it incurs some additional computational costs in the preparatory offline stages. The full FE solution

required 298 s for completion. The K-N method without ROM updates required only 4 s for all computations, including pre-processing steps. The UK-N method with ROM updates required a total of 28 s for all computations. A large percentage of this total simulation time is attributed to the preparatory stage for ROM database construction, while the actual dynamic analysis required only 7.6 s. In this analysis, the ROM is constructed using the first three eigenmodes, resulting in a 3-DOF reduced-order model. A convergence study is conducted by adding more eigenvectors to the reduction basis. The results of the convergence study are presented in Figure 3.4, which shows a magnified view of a peak in the steady-state solution. When utilising only the first eigenmode in the reduction basis, the dynamic response differs from the converged response by 1.1%. However, further addition of eigenmodes beyond the first three does not have a major impact on the analysis results.

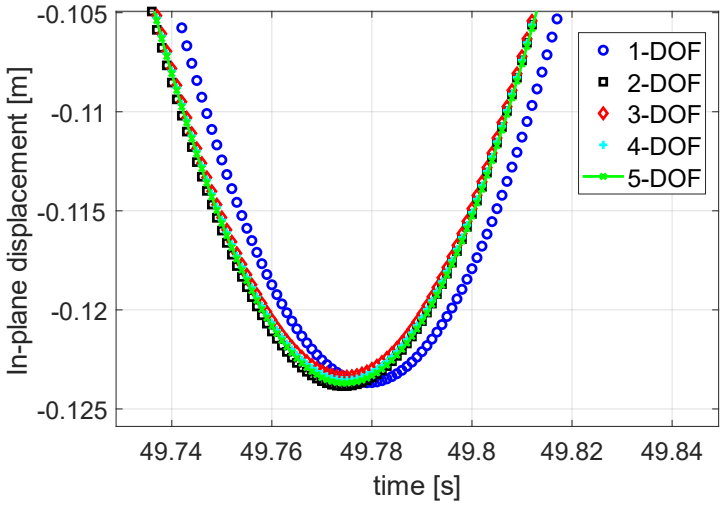

(a)

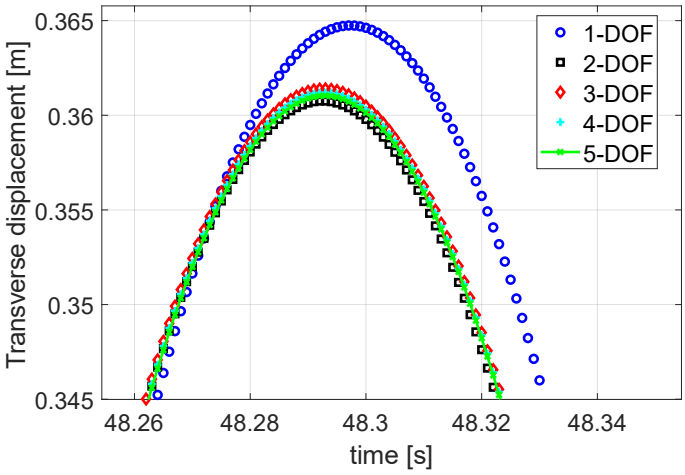

(b)

Figure 3.4: Convergence study with up to 5-DOF ROM for the steel cantilever beam (Pany and Rao, 2002) – (a) in-plane displacement, (b) transverse displacement

3.3.2. Experimental validation

The first experimental investigations of extremely large amplitude dynamics of cantilevers with base excitation were conducted by Farokhi et al. (2022). The experiments were performed on a thin 1095 blue-tempered spring steel cantilever sheet to achieve very large oscillation amplitudes without plastic deformation. The cantilever was placed in a vacuum environment to minimise air damping effects. A high-speed camera was utilised to capture the vibration response at different frequencies, and changes in eigenfrequencies with increasing amplitudes due to geometrically nonlinear effects were studied. In the present work, the K-N method is applied to obtain frequency-amplitude variation, and the results are compared to the experimental studies. The dimensions of the test structure are as follows: length l = 81.5 mm, cross-section width

b = 9 mm, and height h = 0.0762 mm. The material properties are: elastic modulus E = 200 GPa and density ρ = 7800 kg/m^3. The first eigenfrequency of the cantilever sheet is 9.38 Hz. An excitation force of 0.005 N is applied at the tip, and a mass-proportional structural damping is applied with a damping ratio of 0.0068. To generate the frequency-amplitude response curve, a frequency sweep is conducted around the linear eigenfrequency and the peak amplitudes at each excitation frequency are captured. The analysis using the ROM is conducted through two approaches: without ROM updating (K-N method) and with ROM updating (UK-N).

The ROM is constructed using the first three eigenmodes, which results in a 3-DOF model. Figure 3.5 shows comparisons of the nonlinear frequency response curves for the first eigenfrequency to experimental data. The experimental data show a hardening-type nonlinearity, which results in an increase in the eigenfrequency with increasing amplitude. In this case, a frequency change of less than 3% is observed when the transverse vibration amplitude is around 80% of the beam length. The results of the K-N method (in blue in Figure 3.5) indicate that it is unable to capture the hardening nonlinearity. This is in agreement with the discussions presented by Farokhi et al. (2022) where a third-order nonlinear model is unable to capture the hardening effects. However, the UK-N method with the suggested ROM updating strategy performs comparatively much better. At vibration amplitudes comparable to the experimental data, a hardening effect is captured by the UK-N approach. The extent of the hardening effect is comparatively lower than the experimental results. This is explainable by the fact that the ROM does not correct for errors in the internal forces. As previously discussed in Section 1.1.1, the FE method employs a corrector step to ensure that the internal forces are accurately matched with the applied external forces.

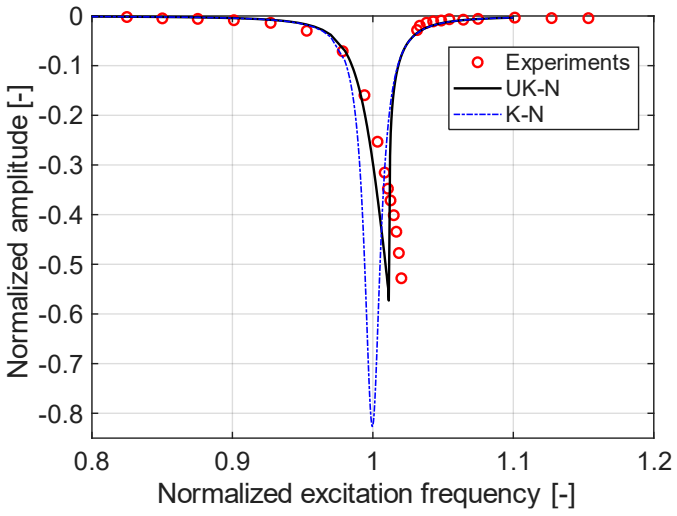

(a)

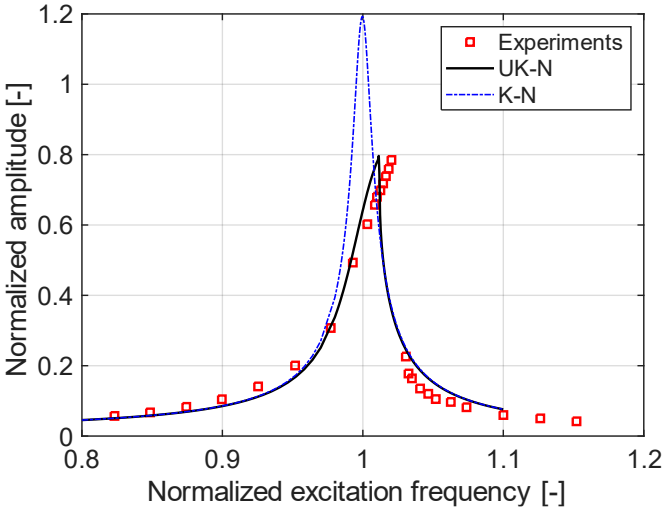

(b)

Figure 3.5: Nonlinear frequency response curves for cantilever sheet compared to experimental data –(a) axial in-plane displacement, (b) transverse displacement

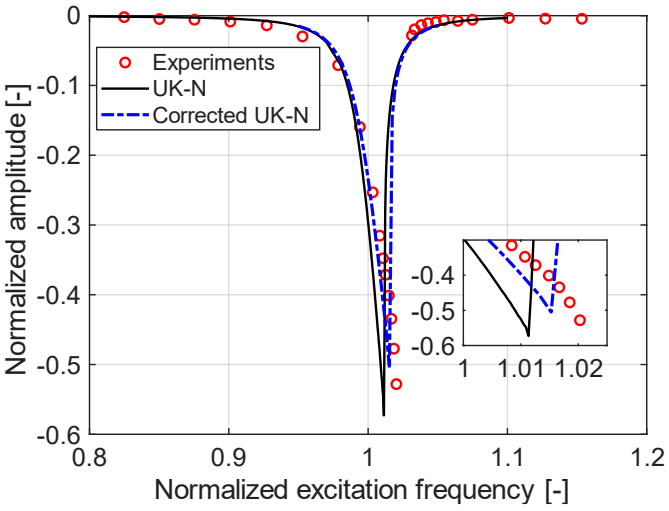

(a)

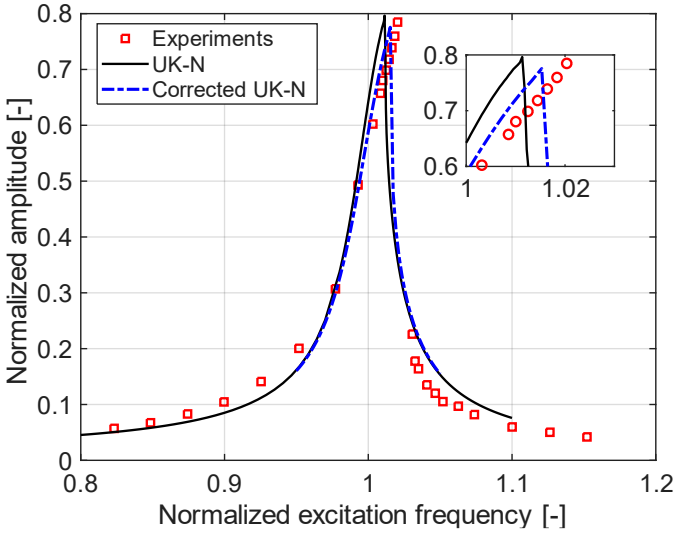

(b)

Figure 3.6: Nonlinear frequency response curves with internal force correction for cantilever sheet compared to experimental data –(a) axial in-plane displacement, (b) transverse displacement

In the ROM solver, this is normally excluded since performing a force correction would entail reconstructing full FE matrices, and make the process less efficient. For comparison, analyses are done where a corrector step is also included, and the results presented in Figure 3.5 are computed again. Figure 3.6 illustrates the nonlinear frequency response curves, which include internal force correction in the solution. This involves computing the internal forces and correcting the displacements through an iterative approach. There is a distinctive difference between the original UK-N solution and the force corrected UK-N solution (refer to the magnified view in Fig. 3.6). The force corrected UK-N is closer to the experimental predictions. However, since this is similar to solving a full order model, it results in a significantly large computational time, which, in this case, is approximately 8 hours. The ROM computations are performed with a time step of 10^{-4} s and a total simulation time of 50 s. The nonlinear frequency response curve consists of 160 data points. With these parameters, the UK-N computations require less than 1 hour to generate the frequency response curve. Note that the utilisation of parametric continuation techniques can further significantly improve the performance of the process. In this verification case, the benefits in accuracy gained from the internal force correction are overshadowed by the considerably large loss in efficiency, which contradicts the purpose of a ROM. For further analysis, moderately large amplitude motion is considered, within the domain of which the ROM is found to be accurate enough without the requirement of internal force correction. Overall, it can be concluded that the utilisation of a ROM updating strategy in combination with the K-N method enhances the accuracy of the method in large amplitude dynamic analyses.

3.3.3. Generic high-aspect-ratio wingbox structure

As a final verification step, the UK-N approach is applied to the slender wingbox structure, presented in Section 2.3.5. The geometrical and material parameters remain as previously defined. The dynamic analysis is conducted using a concentrated tip force of 1000 N applied at two locations – 40% and 60% chord position - with an excitation frequency of 0.685 Hz. The grid points forming the cross-sectional profile at the wing root are fully clamped. A mass proportional damping is applied with a damping ratio of 0.0562. The analysis is conducted for a total simulation time of 30 s with a fixed time increment of 10^{-3} s. A convergence study is conducted, and the first 8 eigenmodes are selected in the reduction basis, which results in an 8-DOF reduced order model. For comparison with the full-order FE model, an analysis is conducted in MSC NASTRAN using an adaptive time step increment.

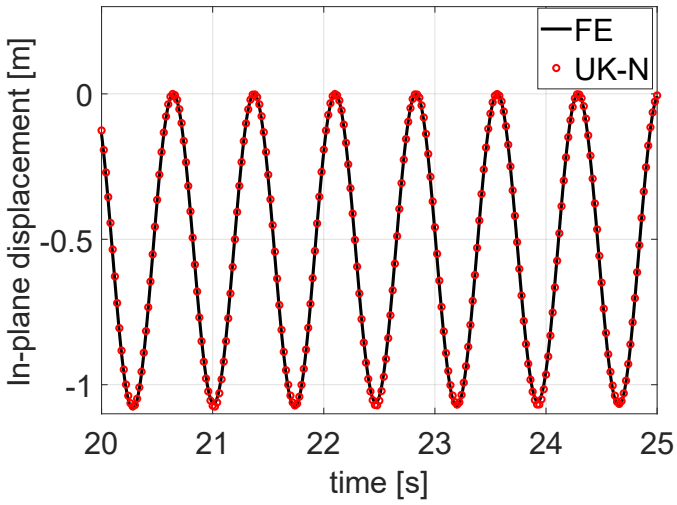

(a)

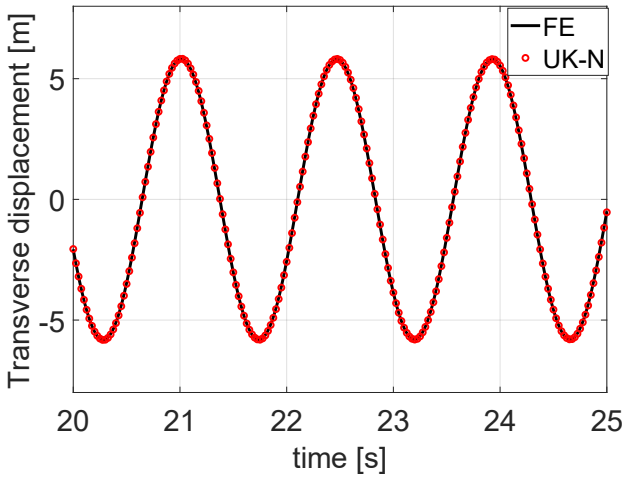

(b)

Figure 3.7: Comparison of time domain response, obtained from the K-N method with ROM updates and from MSC NASTRAN –(a) axial in-plane displacements, (b) transverse displacements

Figure 3.7 illustrates a comparison of the time domain response after the steady state is achieved. The results from the UK-N method are in good agreement with NASTRAN. A difference of 0.02 % is obtained in transverse displacement and 0.94% in the axial in-plane displacement. The FE solution requires 4.85 hours for completion, while the UK-N with an 8-DOF model can be fully executed in 4.16 minutes. A reduction of 98.6 % is achievable in the simulation time. However, this does not include the time required for computing the ROM database. The computational costs incurred for the preparatory stages depend on the number of load increments applied in nonlinear static analyses.

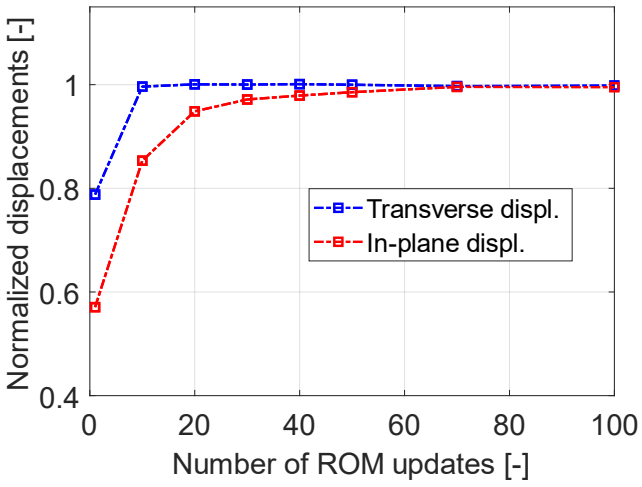

(a)

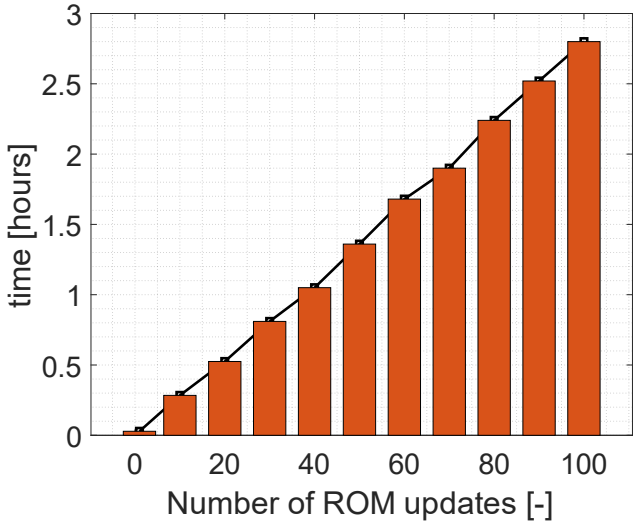

(b)

Figure 3.8: Influence of different numbers of load increments on the ROM construction process – (a) variation in tip displacements, (b) increase in computational time

Smaller FE models, such as the beam models utilised in the first two verification cases, enable rapid ROM computation. Therefore, applying a large number of load increments and ROM updates in the preparatory stages is not detrimental to the efficiency gained through the ROM. However, the wingbox model demands a closer assessment of the required number of ROM updates due to a significantly higher ROM computational cost. Figure 3.8 depicts the influence of choosing different number of ROM updates in the preparatory stage on the dynamic response and the corresponding computational costs.

The maximum tip displacements normalised by the FE solution in steady state are plotted against the number of ROM updates in Figure 3.8 (a). The transverse displacements converge quickly, while a greater number of updates are required to obtain a convergence in the in-plane displacements. The results presented in Fig. 3.7 are obtained using 100 load increments which required a computational time of 2.8 hours. Depending on the requirement, a compromise can be made with respect to the number of load increments and accuracy. For this model, the utilization of 40 increments is sufficient to obtain results with a maximum 2% error margin. The time required for the ROM computations is plotted against the number of load increments in Figure 3.8 (b). The variation is almost linear since each ROM update cycle involves the same set of computations with different geometrical configurations. The gain in computational efficiency is greater when the ROM is utilised for multiple analyses since the ROM database must only be computed once.

In Section 3.3.2, the nonlinear dynamic characteristics of a thin cantilever sheet are discussed, where a hardening effect, typical of nonlinear models, is observed at vibration amplitudes approaching 80% of the cantilever length. A similar analysis is conducted for the wingbox structure to assess if the same behaviour can also be expected for a more

complex geometry. The time domain analysis presented for this model has already demonstrated that results comparable to the full-order model can be obtained using an 8-DOF reduced-order model. Therefore, to obtain the nonlinear frequency response curve, we utilise the same 8-DOF model.

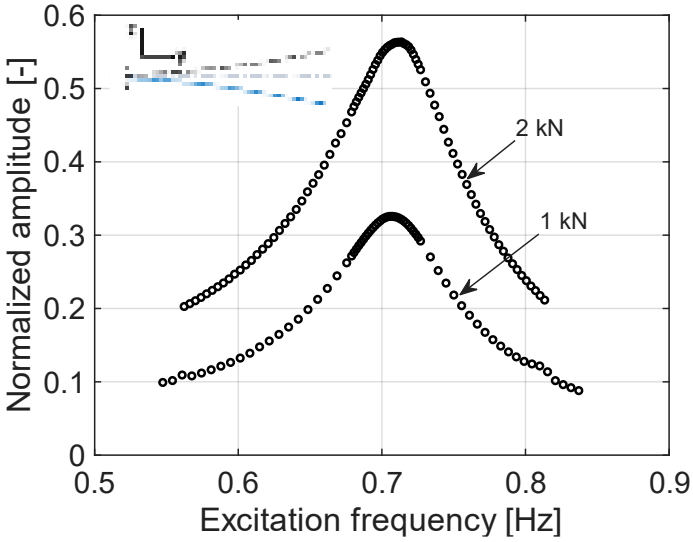

Figure 3.9: Frequency-amplitude variation in the first eigenmode of the wingbox structure

To construct the frequency response curve, time domain analysis is conducted for various excitation frequencies in the neighbourhood of the linear eigenfrequency of interest and the maximum tip amplitudes for each case are extracted. Figure 3.9 shows the nonlinear frequency response curve of the first bending mode of the wing. Even at almost 50 % tip deflection there is not a significant variation in the eigenfrequency. This aligns with the results presented in Section 3.3.2. Considering the computational time, the ROM is much more efficient requiring 5.87 hours to generate the entire frequency response curve with 90 data points. The

full order FE model requires approximately 5 hours for a time domain response at a single excitation frequency. Generating a similar frequency response curve with the FE model would require several days. A similar analysis is also conducted for the second eigenmode which is an in-plane bending mode. In this case, a relatively stronger hardening effect is seen at around 16 % tip deflection, as shown in Fig. 3.10. Even though the general bending profiles are same for both the mode shapes, the wingbox construction is not symmetrical and therefore, differences are expected in the nonlinear characteristics. Considering realistic wing structures, the amplitudes at which hardening effect begins to show for both cases are far beyond what is encompassed in normal operational conditions of an aircraft.

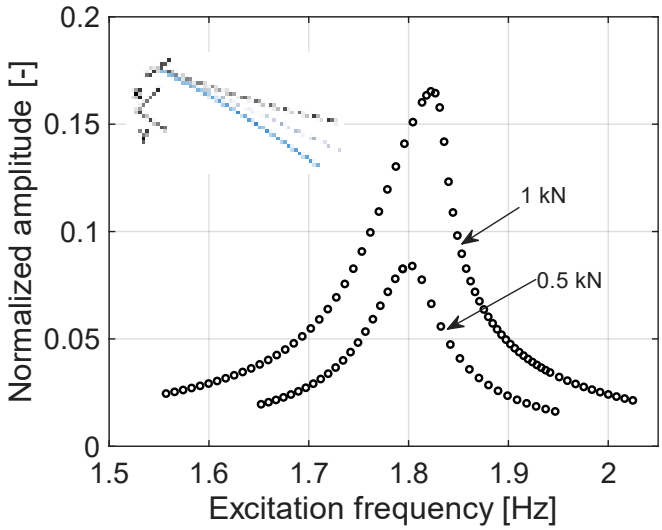

Figure 3.10: Frequency-amplitude variation in the second eigenmode of the wingbox structure

3.4. CONCLUSIONS

A momentum subspace variant of the K-N method has been introduced in this Chapter. Numerical studies showed that extremely large amplitude dynamics cannot be modelled if the ROM is formulated only in the initial equilibrium state. A ROM updating strategy is proposed within the framework of Newmark time integration, which involves creating a ROM database based on nonlinear static analyses. Model verification has been done through comparison to full-order FE time domain analyses and experimental data. The utilisation of the updating strategy has been found to be effective in capturing hardening effects in cantilevers undergoing extremely large amplitude vibrations. The method has also been applied to a wingbox structure comprising a large number of degrees of freedom. It is found that even though the ROM generation time considerably increases for large models, computation of the nonlinear frequency response curve using the ROM is an efficient approach in comparison to FE analyses. The frequency response curves for the wingbox structure indicate that large-amplitude dynamic motion does not significantly impact the eigenfrequencies of the transverse and in-plane bending modes.

4

PAZY WING AS A BENCHMARK CASE

The Koiter-Newton method and its momentum subspace variant have been established in Chapters 2 and 3, respectively. Numerical investigations have demonstrated that the method can be successfully utilised for large deflection analyses, both static and dynamic. For large structural models, which are representative of engineering structures, analysis efficiency can be considerably improved compared to full-order models, particularly in dynamic analyses. However, the time required to obtain the ROM parameters counteracts the efficiency gain, as seen in Section 3.3. To achieve the objective of constructing a nonlinear

This Chapter is based on the publication: Sinha, K., Alijani, F., Krueger, W. R., & De Breuker, R. (2024). Nonlinear dynamic response of a Pazy wing variant using Koiter-Newton model reduction. In *International Forum on Aeroelasticity and Structural Dynamics*.

aeroelastic model using the Koiter-Newton method, subsequent studies focus on the Pazy wing as a benchmark case. The choice of Pazy wing as a reference model is based on the availability of prior research data, both experimental and numerical. In this Chapter, the structural characteristics of the Pazy wing are presented, the development of a Pazy wing model variant is discussed, and numerical studies are conducted to additionally verify the developed model. The Chapter is further divided as follows: Section 4.1 provides a general overview of the Pazy wing and discusses the characteristics of the FE model used in the present work, Section 4.2 presents the impact of large deflection on the static response, Section 4.3 presents dynamic characteristics of the Pazy wing, and finally, the Chapter is concluded in Section 4.4.

4.1. FE MODEL DEVELOPMENT

The Pazy wing has been designed at Technion with the objective of investigating nonlinear aeroelastic phenomena related to large deflection behaviour in highly flexible wings. The design, analyses and experimental data of the wing were first presented by Avin et al. (2022). One of the primary design criteria for the wing is that it should be able to deform up to 50% of its span under static loading conditions. The experimental measurements were performed at a Mach number of approximately 0.15, corresponding to the highest air speeds. The wing is constructed with a rectangular planform and no sweep. The symmetrical NACA0018 airfoil is utilised for the cross-section definition. The wing has a chord length of 100 mm and a span of 550 mm. The wing comprises a rectangular Aluminium 7075 plate structure (spar), 550 mm in length and 60 mm in width. The plate is surrounded by a 3-D printed chassis made of Nylon 12. Additionally, a 300 mm long rod with a diameter of 10 mm is added at the tip, which is used to attach extra weights and modify the

dynamic characteristics of the wing. The chassis is wrapped with an Oralight Polyester foil to provide a uniform surface for airflow. Structural FE models of this wing were made available within the framework of the AePW3. The full FE model comprises a combination of shell elements, beam elements and rigid body elements. Figure 4.1 depicts the FE model of the Pazy wing originally developed by Avin et al. (2022). The elements in red depict the beam elements in the model, while the remainder of the model is constructed using shell elements.

In the studies conducted in the AePW3, it was found that the Oralight foil causes issues in nonlinear analyses. Due to the relatively low thickness of the foil and its stiffness characteristics, these elements buckle at low deformations (Ritter et al., 2024), as the pre-stressing in the foil is not considered. This causes convergence problems in nonlinear analyses. The thin foil adds a relatively small stiffness to the structure; therefore, a model variant without the foil has been utilised in some of the prior research (Hilger and Ritter, 2021).

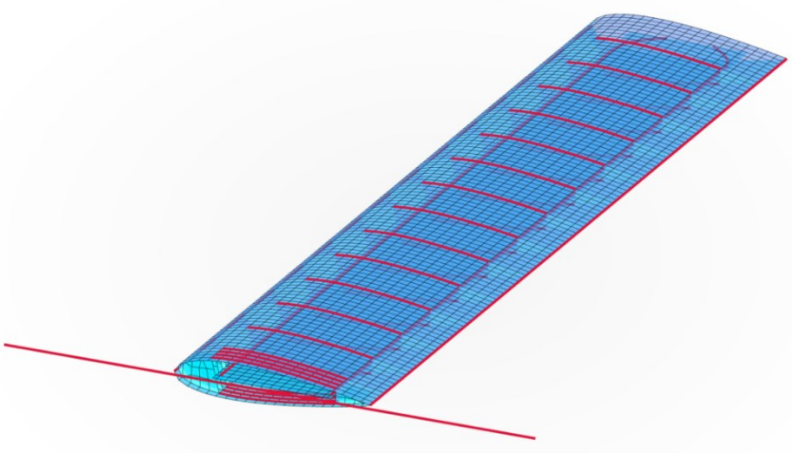

Figure 4.1: FE model of the original construction of the Pazy wing (Avin et al., 2022)

In Section 2.1, the requirement of higher-order stiffness tensors and the utilisation of triangular shell elements in the FE modelling have been discussed. An FE model is required, which is compatible with the FE formulations described in Appendix I. Due to this, adaptations are introduced in the original FE model of the Pazy wing to ensure its compatibility. The beam elements used to model the leading edge, trailing edge, tip rod, and parts of the Nylon chassis (see Fig. 4.1) are replaced by shell elements, considering the cross-sectional area and inertial properties of the beams defined in the reference model.

Figure 4.2 shows the FE model constructed using shell elements. The shell model comprises 39,930 triangular elements and 21,712 grid points, which results in 130,272 DOFs in the model. The meshing in the present model is refined compared to the reference model to assess how the K-N method performs when the number of DOFs in the model is increased. The distinctive features observable are the 2-D adaptations of the leading edge, trailing edge and the tip rod. This results in an extended structural definition in the x- and y-directions when compared to the original model, 112 mm and 560 mm, respectively. Another modification is in the way the Nylon chassis connects to the central spar section. Figure 4.3 a and b show the cross-sectional view of the original and modified FE models, respectively. The cross-section shape definition for the present model is in accordance with the CAD model developed by Avin et al. (2022). The stiffening element along the edges of the central spars, however, is excluded. The resultant differences in structural characteristics are assessed by conducting a modal analysis of the two FE models using MSC NASTRAN. Additionally, the model is imported into the framework used in the present work (MATLAB implementation, discussed in Chapter 2), and an eigenvalue analysis is performed to verify the model.

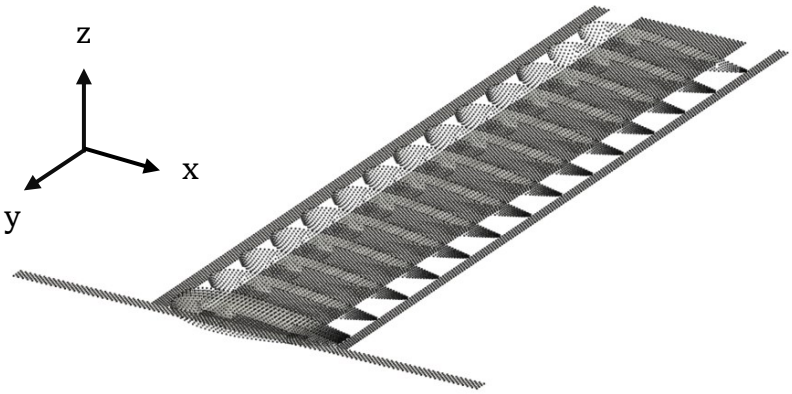

Figure 4.2: FE model of the Pazy wing constructed entirely with shell elements

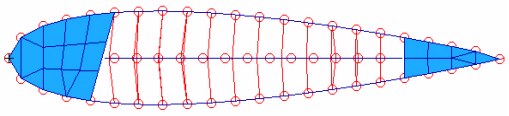

(a)

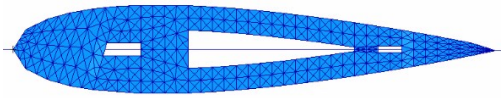

(b)

Figure 4.3: Comparison of cross-sectional view of the (a) reference FE model (Avin et al., 2022) and, (b) modified shell model (present work)

The Oralight foil is also excluded in the present model to avoid issues due to skin buckling in nonlinear analyses. The first five eigenmodes of the Pazy wing are shown in Fig. 4.4, and the eigenfrequencies of the present model are compared to the reference

model in Table 4.1. The eigenfrequencies show some expected differences between the reference and the present models, with a maximum difference of 3.1%. A comparison is also made between the eigenfrequencies of the present model computed in NASTRAN and in MATLAB. The third eigenfrequency, corresponding to the first torsion mode, shows a relatively large difference of 2.6%. This is attributed to the differences in the FE formulations.

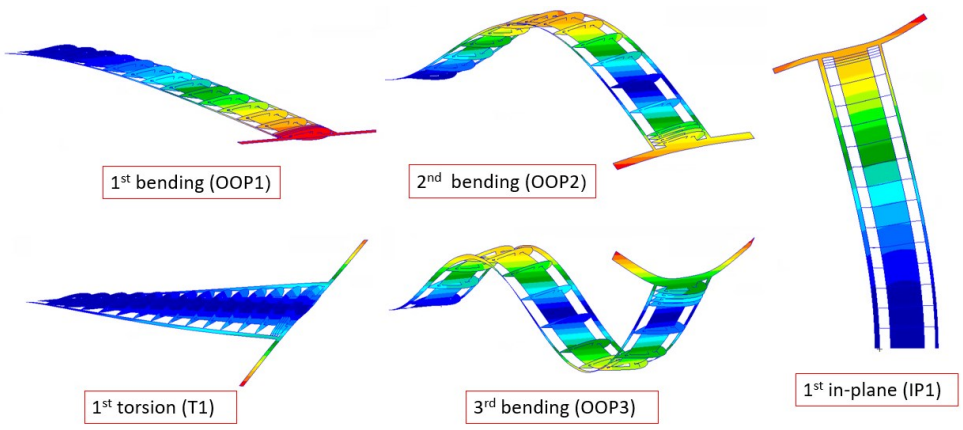

Figure 4.4: First five eigenmodes of the Pazy wing

The total mass of the present FE model is 0.334 kg, while the reference FE model has a total mass of 0.328 kg. A linear static analysis conducted with a concentrated point load of 20 N yields a tip transverse displacement of 0.252 m for the reference model and 0.272 m for the present model, which is a difference of 3.6% of the span. The lower frequencies and displacements for the same applied load indicate that the present model is less stiff compared to the reference. The model characteristics are sufficiently close to the original design and suitable for

further investigations related to nonlinear structural and aeroelastic effects.

Table 4.1: Comparison of eigenfrequencies of the Pazy wing model variants

Mode	Reference [Hz] NASTRAN	Present [Hz] NASTRAN	Present [Hz] MATLAB
1 - OOP1	4.42	4.28	4.28
2 – OOP2	28.98	28.12	28.15
3 – T1	40.33	38.49	39.47
4 – OOP3	82.40	80.17	80.39
5 – IP1	112.56	111.50	111.75

4.2. LARGE DEFLECTION BEHAVIOUR

The structural model of the Pazy wing has been verified, and we can now proceed to investigate the nonlinear response of the Pazy wing variant. First, a nonlinear static analysis is conducted using the K-N method, and the results are presented in Section 4.2.1. In Section 4.2.2, the influence of nonlinear static deformations on the eigenfrequencies is investigated.

4.2.1. Nonlinear static response of the Pazy wing

The methodology for nonlinear static analyses described in Section 2.2 is used to predict the large deflection response of the Pazy wing. A concentrated load of 20 N is applied such that the wing tip deflects approximately up to 45 % of the span. In addition to the geometric

nonlinearity, follower forces are also considered, which are typical for a wing structure. For reference, nonlinear static analyses are also conducted in SOL400 MSC NASTRAN using the same analysis parameters. An adaptive load step increment is applied in NASTRAN, and solution convergence is based on the total internal force and work done. In the K-N method, the external force vector is utilised as the reduction basis, resulting in a 1-DOF reduced-order model.

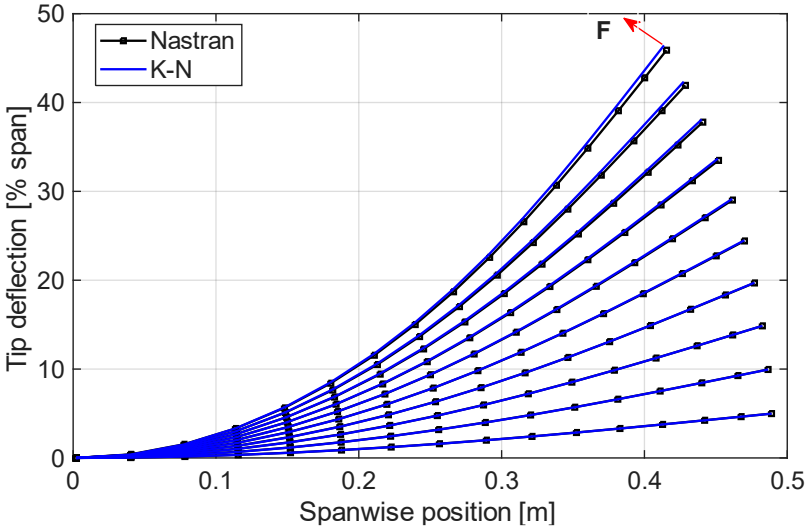

Figure 4.5: Nonlinear static deformation of the Pazy wing under tip concentrated follower force

The K-N method is able to closely replicate the results from NASTRAN with an error of 0.7% at the maximum loading condition, when the tip deflection is approaching 45% of the span. NASTRAN has a significantly longer computational time for this model and requires around 96 minutes for full completion. This is due to the much larger model size in terms of the number of DOFs. Additionally, the number of steps required for convergence within the iterative solution procedure is also large, requiring

up to 3152 iterations. The K-N method requires 30 minutes for the complete analysis, including ROM generation, with the application of 12 load increments.

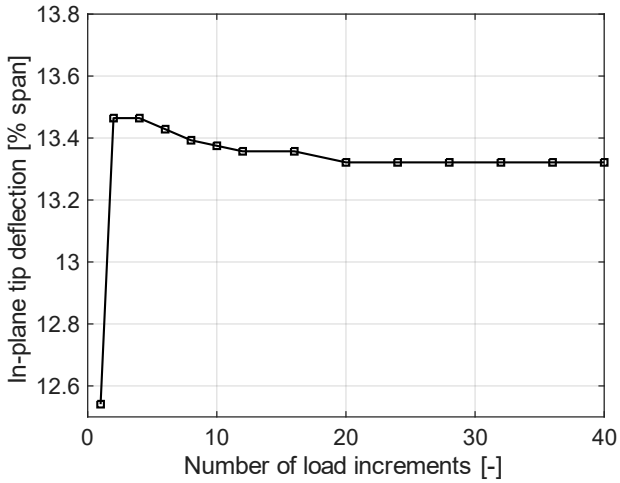

(a)

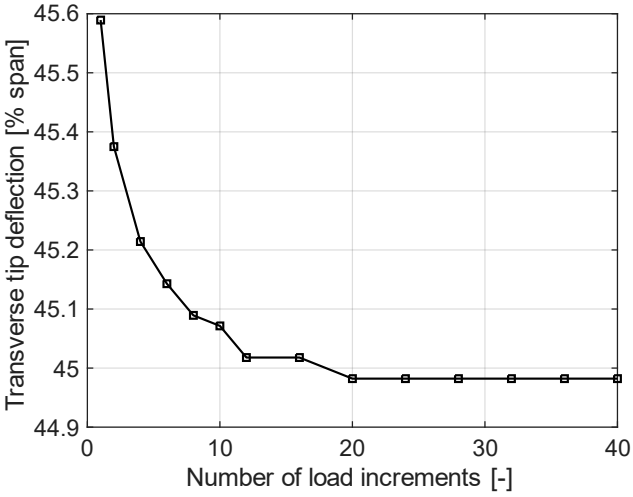

(b)

Figure 4.6: Convergence of (a) transverse and (b) in-plane tip deflections with increasing number of load increments

A convergence analysis is conducted to understand the effect of the number of load increments on the accuracy of the solution. Figure 4.6 illustrates the improvement in ROM results achieved by increasing the number of load increments. At 20 load increments, the solution shows a difference of only 0.03 % compared to the NASTRAN results. This, however, increases the computation time to 48 minutes.

4.2.2. Influence of geometric nonlinearities on the eigenfrequencies

Static structural deformations in the nonlinear domain result in changes to the structural stiffness. These changes consequently influence the modal characteristics. Understanding the variations in modal characteristics is not only important from a structural perspective but also, in the case of aircraft wings, crucial from an aeroelastic perspective. The approach employed here involves deforming the structure nonlinearly when subjected to various applied loads. In each of these deformed equilibrium states, the system is linearised, and an eigenvalue analysis is performed in order to evaluate the eigenfrequencies.

Figure 4.7 depicts the first five eigenfrequencies of the Pazy wing as a function of transverse tip displacements. The abbreviations of the mode shapes correspond to the modes described in Figure 4.4. To obtain these results, 40 load increments are applied, and for each load step, an eigenvalue analysis is performed using the stiffness matrix extracted from the deformed structural model. Note that the ROM does not need to be recomputed for these analyses; rather, the ROM generated in the static analyses performed in Section 4.2.1 can be utilised. The results are compared to MSC NASTRAN, and they are observed to be qualitatively similar. Interestingly, the first modal frequency shows only a minor

variation of 2.5%. The second frequency varies by 7.5%, and the fourth frequency varies by 4.7%. Larger variations are seen in the third (52.1%) and the fifth (51.3%) eigenfrequencies. The trends observed are also similar to those reported by Riso and Cesnik (2021) and Hilger and Ritter (2021).

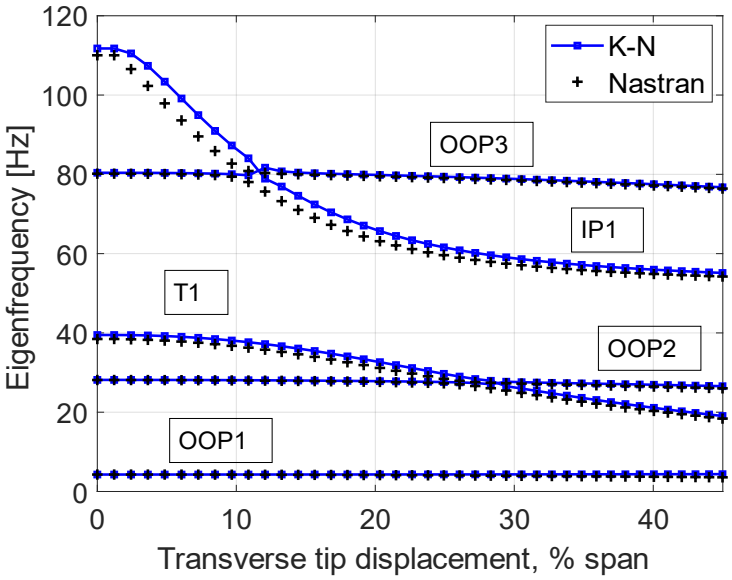

Figure 4.7: Evolution of eigenfrequencies of the Pazy wing with increasing nonlinear deflection

4.3. NONLINEAR TIME DOMAIN RESPONSE OF THE PAZY WING

In this Section, the K-N method is utilised to study the nonlinear dynamic characteristics of the Pazy wing. The wing is subjected to harmonic perturbations, and the time domain response is computed. The effectiveness of the ROM for this model is established through comparisons to full-order FE solutions. The wing is excited using a load

which is a 1-*cos* function of time. Such a perturbation is a typical approximation for simulating gust loads on an aircraft. A concentrated, non-follower force of 4 N is applied at the wing tip with an excitation frequency of 4.28 Hz. A mass proportional damping is applied with a damping ratio of 0.093. A relatively higher damping ratio is chosen, as the reference solution in NASTRAN is unable to reach convergence at lower damping ratios. The ROM solver does not encounter convergence problems, regardless of the choice of damping ratios. The excitation force is applied for 1.5 s, and a time step of 0.001 s is utilised. A fixed time step increment is utilised in the ROM solver. In NASTRAN, an adaptive time step increment is utilised with convergence criteria based on the internal force and total work. Figure 4.8 shows the transient response obtained using the momentum subspace variant of the K-N method (see Chapter 3). For the applied conditions, the tip transverse displacement exceeds 27% of the span and is in the geometrically nonlinear domain.

The solution obtained using the K-N method is in good agreement with the results of the full-order model in NASTRAN. The maximum transverse displacement predicted using NASTRAN is approximately 27.6%, while the ROM predicts 28.3% of the span. Similarly, the in-plane displacement predicted by NASTRAN is -4.66%, while the ROM predicts it to be -4.72% of the span. The in-plane displacements are not predicted when using a linear model. The computational time required in NASTRAN is about 4.2 hours. The ROM is constructed using the first two eigenmodes of the wing, which results in a 2-DOF model. The total time required for constructing the ROM is considerably large, approximately 33 minutes. However, the actual simulation time required to compute the transient response when using the 2-DOF reduced-order model is 7.9 s. Notably, the majority of the computational time is spent on constructing the ROM.

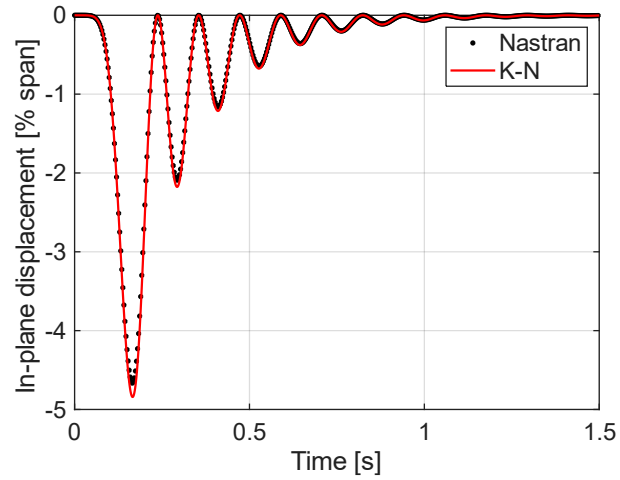

(a)

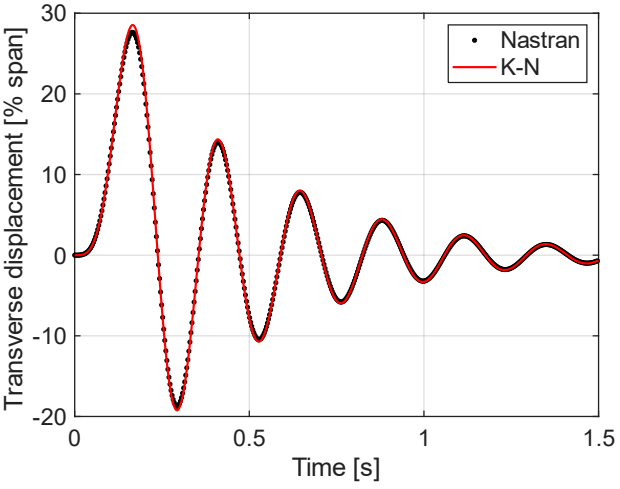

(b)

Figure 4.8: Transient response of the Pazy wing tip when subjected to a 1-cosine perturbation load (a) in-plane displacement, (b) transverse displacement

As shown in Fig. 4.8, it is sufficient to construct the ROM in the initial equilibrium state to obtain a response comparable to that of the full-

order model. The ROM updating procedure discussed in Chapter 3 is not utilised in these analyses. A reduction of 5 orders of magnitude in the model size is achieved through the ROM without a significant loss in solution accuracy. A convergence analysis is conducted to show that the 2-DOF model chosen is adequate for obtaining the transient response, and the addition of further eigenmodes in the reduction basis does not improve the solution further.

Five variants of the ROM are constructed using up to five eigenmode shapes in the reduction basis. Figure 4.9 shows a comparison of the solutions obtained with the various ROMs constructed. The enlarged views of the peak amplitudes for the transverse and in-plane displacements are plotted in Fig. 4.9. It is observed that the 1-DOF model produces a stiffer response with the amplitudes lower by around 0.3%. The solutions obtained using the other ROM variants have differences in the order of 0.01%. Thus, the 2-DOF reduced-order model is considered sufficient for this load case.

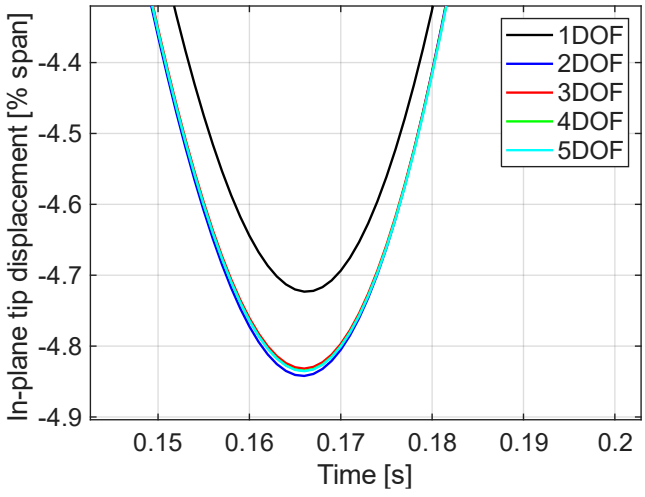

(a)

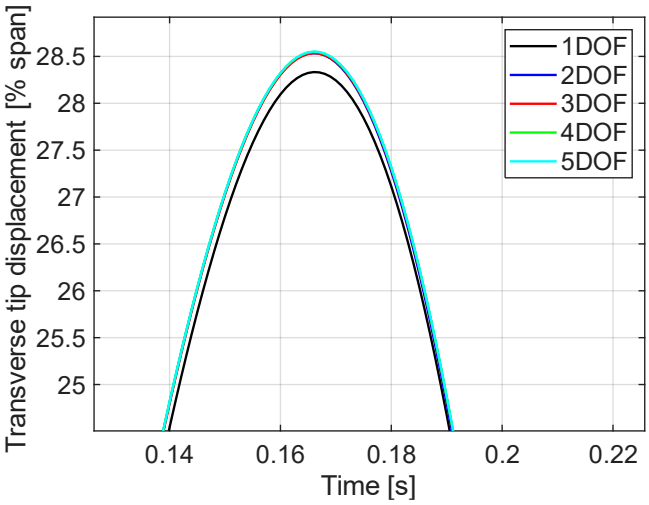

(b)

Figure 4.9: Convergence of the transient response with increasing number of eigenmodes in the reduction basis (a) in-plane displacement, (b) transverse displacement

4.4. CONCLUSIONS

The Pazy wing benchmark model was introduced in this Chapter. The necessary modelling adaptations are discussed, and comparisons are made to the reference Pazy wing model developed at Technion. In general, the model utilised in this work is relatively more flexible than the reference model, as evident from the modal and linear static analyses. Nonlinear static analyses conducted using the K-N method show a good agreement with results obtained from NASTRAN. The effects of geometric nonlinearities are further seen through variations in eigenfrequencies. The structure is initially subjected to nonlinear static displacements obtained under various loading conditions. The system is thereafter linearised, and eigenvalue analyses are conducted. When

tracking the first five eigenfrequencies of the Pazy wing, particularly large variations are observed in the 1st torsion and in-plane bending modes. The large variations in the frequencies and vicinity to other eigenfrequencies indicate potentially enhanced modal interactions when deflections are sufficiently large. Finally, dynamic analyses are conducted where the wing is subjected to large-amplitude perturbations, such that the resultant deflections fall within the geometrically nonlinear domain. The K-N method is found to be highly efficient for these analyses, with simulation times reduced to 7.9 s. This is achievable due to the 5 orders of reduction in the model size obtained from the K-N method. A 2-DOF ROM is found to be sufficient to reproduce the nonlinear dynamic response obtained from the full-order model.

5

NONLINEAR AEROELASTIC RESPONSE OF HIGHLY FLEXIBLE WINGS

The effectiveness of the Koiter-Newton method for various nonlinear static and dynamic problems has been substantiated in Sections 2.3 and 3.3. Application of the K-N method to structural models with a large number of DOFs has also been studied. Regardless of the initial size of the FE model, it is possible to construct a ROM with fewer than 5-DOFs, for the chosen verification cases, using the K-N method with only a marginal loss in solution accuracy (see Section 4.3). The Pazy wing benchmark case, which was previously discussed in Chapter 4, will be the focal point of the current chapter.

The next objective is to develop an aeroelastic model that is suitable for wings undergoing geometrically nonlinear deflection. The requirement of such a model arises due to aeroelastic effects related to geometrical nonlinearities. Earlier studies have demonstrated a reduction in flutter speed due to large wing deflections (Patil et al. , 2001; Patil and Hodges, 2004; Jian and Jinwu, 2009; Arena et al., 2013). In the same studies, computation of dynamic response in the time domain has shown the occurrence of limit cycle oscillations, which are attributed to the nonlinearities in the aeroelastic system. Notably, the majority of these works have utilised structural formulations based on variants of geometrically exact beam theory, which requires transforming an FE model into an equivalent beam model. Recently, development of benchmark models such as the X-HALE (Cesnik et al., 2012) and Pazy wing (Avin et al., 2022), along with experimental studies (Tang and Dowell, 2001), has provided valuable insights into nonlinear aeroelastic phenomena. In this Chapter, the development of a nonlinear aeroelastic model is presented that is compatible with generic FE models and does not rely on the transformation of the geometry to an equivalent beam. The K-N method is utilised to model the nonlinear kinematics. The aeroelastic model is obtained through a combination of the K-N method and the Peters finite-state unsteady thin-airfoil theory (Peters et al., 1994; Peters et al., 1995). The coupling procedure of the generalised displacement variables, in which the ROM is formulated, and the aerodynamic state variables, is elaborated in this Chapter.

The Chapter is further divided into five main parts. Section 5.1 presents the implementation of an aerodynamic model based on Peters theory. Section 5.2 discusses the coupling approach between the aerodynamics model and the full order model. The formulations of numerical models for nonlinear static aeroelastic, flutter and post-flutter

dynamic analyses are presented in Section 5.3. The results of the numerical studies conducted on the Pazy wing are presented in Section 5.4. Finally, the conclusions are discussed in Section 5.5.

5.1. PETERS FINITE-STATE UNSTEADY THIN-AIRFOIL THEORY

The aerodynamic model utilised in the present work is based on the Peters finite-state unsteady thin-airfoil theory (Peters et al., 1994; Peters et al., 1995). Although the method was originally proposed for rotary wings, it is also applicable to fixed-wing aircraft. The model is derived from potential flow theory, which assumes conditions leading to incompressible, irrotational, and inviscid flow, and utilises the thin airfoil assumption, implying that the airfoil thickness is small compared to its chord length. The potential flow theory is well described in textbooks, such as Katz and Plotkin (2001), and will not be discussed further here. One of the focal points of Peters theory is the inclusion of large amplitude motion, which is achieved through the definition of an arbitrary frame of reference with no small angle assumptions. Furthermore, the theory allows for small elastic deformations of the airfoil within a corotational frame of reference.

Peters theory describes the aerodynamic forces acting on a 2-D airfoil with consideration of unsteady effects. The total lift and pitching moments on an airfoil are computed in two parts, comprising circulatory and non-circulatory effects. The non-circulatory component arises due to the apparent inertial effects introduced by the air mass surrounding an airfoil which has non-zero acceleration. The circulatory component refers to the forces generated by the flow of air around an airfoil, ultimately leading to the formation of vortices. The unsteady aerodynamic effects

are included based on the induced flow velocity caused by the shedding of vortices in the wake of the flow. The velocity field near an airfoil comprises an additional velocity component to account for the induced flow. The formulation decouples the computation of loads from the induced flow computation so that, in practice, any wake model can be utilised (Peters et al., 1994).

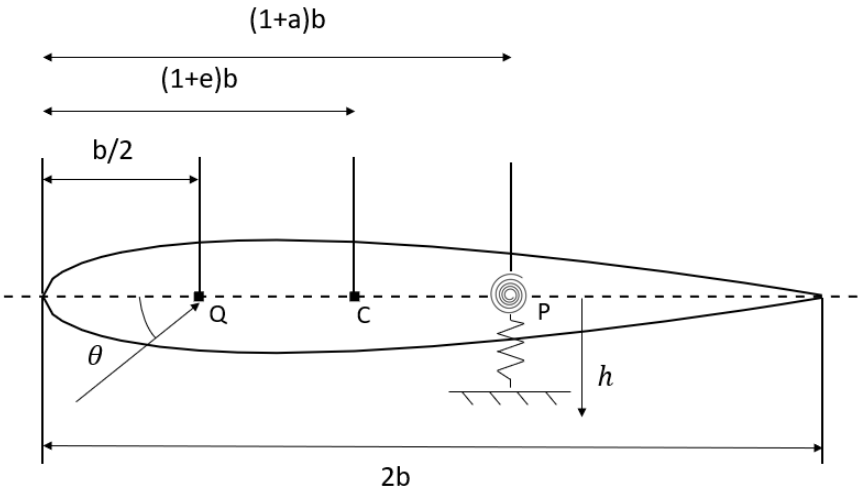

Figure 5.1: Representation of a typical 2-D airfoil section (Hodges and Pierce, 2011)

The aerodynamics model based on Peters theory, discussed further in this Section, follows the description presented by Hodges and Pierce (2011). For this purpose, a typical 2-D airfoil is considered, as shown in Fig. 5.1, which can undergo plunge and pitch motion about a reference point P. The centre of mass is represented by the point C, and Q is the aerodynamic centre, which, according to the thin airfoil theory, is assumed to be at the quarter-chord position. The dimensionless parameters *e* and *a* determine the positions of the points C and P, respectively.

The effective angle of attack α is described as:

$$\alpha = \theta + \frac{\dot{h}}{U} + \frac{b}{U}\left(\frac{1}{2} - a\right)\dot{\theta} - \frac{\lambda_0}{U} \tag{5.1}$$

where θ is the pitch angle, $\dot{h}$ is the plunge velocity, *U* is the air flow velocity, *b* is the semi-chord length, $\dot{\theta}$ is the pitch rate, and λ_0 is the induced flow velocity due to the shed wake.

The lift L_0 and moment M_0 per unit span acting on the reference point are then given by:

$$L_0 = \pi\rho_\infty b^2\left(\ddot{h} + U\dot{\theta} - ba\ddot{\theta}\right) + 2\pi\rho_\infty Ub\left[\dot{h} + U\theta + b\left(\frac{1}{2} - a\right)\dot{\theta} - \lambda_0\right] \tag{5.2}$$

$$M_0 = -\pi\rho_\infty b^3\left[\frac{\ddot{h}}{2} + U\dot{\theta} + b\left(\frac{1}{8} - \frac{a}{2}\right)\ddot{\theta}\right] + L_0\left(\frac{1}{2} + a\right)b \tag{5.3}$$

The induced flow velocity λ_0 is an unknown and is related to the airfoil motion using the approach of Peters et al. (1994). The induced flow velocity is approximated as:

$$\lambda_0 = \frac{1}{2}\sum_{n=1}^{N}\bar{b}_n\,\lambda_n \tag{5.4}$$

where *N* is the number of induced flow states λ_1, λ_2, …., λ_N. The induced flow is expanded as a truncated harmonic function, and the induced flow states refer to the coefficients of this harmonic function. As can be seen

from Eq. 5.4, λ_0 is a weighted average of the induced flow states. The coefficients $\bar{b}$ in Eq. 5.4 are obtained using the following equations:

$$\bar{b}_n = -1^{n-1} \frac{(N+n-1)!}{(N-n-1)!} \frac{1}{(n!)^2}, n \neq N$$
$$\bar{b}_n = -1^{n-1}, n = N \tag{5.5}$$

If $\boldsymbol{\lambda}$ is a vector comprising the induced flow states λ_n, the dynamics related to the induced flow is described as:

$$\bar{\boldsymbol{A}}\,\dot{\boldsymbol{\lambda}} + \frac{U}{b}\boldsymbol{\lambda} = \bar{\boldsymbol{c}}\left[\ddot{h} + U\dot{\theta} + b\left(\frac{1}{2} - a\right)\ddot{\theta}\right] \tag{5.6}$$

The matrices $\bar{\boldsymbol{A}}$ and $\bar{\boldsymbol{c}}$ are Peters constants and are dependent on the number of induced flow states and derived using the following expressions:

$$\bar{\boldsymbol{A}} = \bar{\bar{\boldsymbol{D}}} + \bar{\boldsymbol{d}}\bar{\boldsymbol{b}}' + \bar{\boldsymbol{c}}\bar{\boldsymbol{d}}' + \frac{1}{2}\bar{\boldsymbol{c}}\bar{\boldsymbol{b}}' \tag{5.7}$$

$$\bar{\bar{D}}_{\boldsymbol{nm}} = \begin{cases} \frac{1}{2n}, & n = m+1 \\ -\frac{1}{2n}, & n = m-1 \\ 0, & n \neq m \pm 1 \end{cases} \tag{5.8}$$

$$\bar{d}_n = \begin{cases} \frac{1}{2}, & n = 1 \\ 0, & n \neq 1 \end{cases} \tag{5.9}$$

$$\bar{c}_n = \frac{2}{n} \tag{5.10}$$

Here, Eq. 5.6 relates the aerodynamic state variables to the structural motion. Together with the structural equation of motion, this provides an aeroelastic model which can be solved in the time domain by numerical integration. The initial verification of the implementation of this aerodynamic model is done using the flutter analysis of a 2-D airfoil, where the problem description and reference results are obtained from Hodges and Pierce (2011). The matrices used in the flutter analysis and the results of this verification study are presented in Appendix III.

5.2. COUPLING OF AERODYNAMIC AND STRUCTURAL MODELS

The application of 2-D aerodynamic models to 3-D wings using strip theory has been briefly discussed in Section 1.2. In this Section, the application of the aerodynamic model to the Pazy wing (Avin et al., 2022) is discussed. Since the aerodynamic model assumes a thin airfoil, the lifting surface is approximated as a 2-D surface projection of the wing planform. This surface is then further divided into segments, parallel to the flow, in the spanwise direction. The aerodynamic characteristics of each segment are governed by an airfoil section lying within the borders of the individual strips. The representative aerodynamic lifting surface for the Pazy wing, which has a rectangular planform, is shown in Fig. 5.2 where the shaded region represents one strip. The structural model must be coupled to this aerodynamic lifting surface appropriately in order to transfer the aerodynamic loads to the structure and the structural deformations to the lifting surface. Recall from Section 5.1 that the plunge and pitch motion of only one reference point is considered in the

aerodynamics model. Loads acting on these reference points for each strip must be transferred to the structural finite element nodes, and the structural deformations transferred back to the aerodynamics model. In general, it is common practice in aeroelastic analysis to consider a reference axis along the wing span with condensed structural properties. These FE nodes on the reference axis are utilised as the primary coupling points to the grid points on the aerodynamic surface.

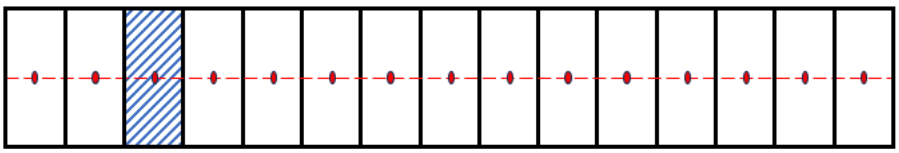

Figure 5.2: Representative aerodynamic lifting surface showing demarcated adjacent strips corresponding to the Pazy wing

These connections can be further enhanced by using rigid body elements to enforce appropriate aerodynamic load distribution. Splining techniques are commonly used to interpolate the forces and displacements over the structural and aerodynamic models, respectively (MSC NASTRAN, 2014).

In the present work, a node-to-node coupling method between the FE and the aerodynamic model is adopted. Due to the limitations imposed by the FE implementation, previously discussed in Chapter 2, the utilisation of rigid body elements for load distribution is excluded. The centre point of each strip, i.e. mid-chord position and spanwise centre of the strip, is assumed to be the reference point for each airfoil section. The FE mesh in the structural model is generated such that FE nodes coincide with the reference point for direct transfer of loads and displacements. The default relation between the aerodynamic coordinate system and the

structural coordinate system is defined so that the following sign convention applies:

$$w_s = -h, \quad \theta_s = \theta \tag{5.11}$$

where w_s represents the structural DOF in the transverse direction and θ_s represents the twist in the structural coordinate system. In the case of the Pazy wing, strips are assumed to lie between two rib sections, which results in a total of 15 strips and, correspondingly, 15 coupling points. This adds a total of 15 x *N* degrees of freedom to the state-space model, where *N* is the number of aerodynamic states assumed in the Peters theory.

There are limitations to applying a 2-D airfoil theory to a finite wing using the strip theory approach. The influence of the flow over one strip is assumed to have no effect on the flow on an adjacent strip. 2-D airfoil theory also assumes infinite span, due to which 3-D effects in the flow at the wing tip are not considered. In a finite wing, air leaks at the tip from a high-pressure region to a low-pressure region, resulting in tip vortices. These tip vortices are responsible for reducing the total lift generated. If these effects are neglected in the aerodynamic model, it leads to an overestimation of the loads acting on the structure. This can be generally resolved by applying a correction factor to the loads. The method described by Riso et al. (2023) for tip loss correction is applied in the present work. The evaluation of the tip loss correction factors for the FE model of the Pazy wing developed in the present work is elaborated in Appendix IV.

5.3. CONSTRUCTION OF NONLINEAR AEROELASTIC MODELS

In this Section, the construction of nonlinear aeroelastic models for various applications is discussed. The focus is on conducting nonlinear static aeroelastic analyses, flutter analyses and simulating post-flutter dynamics in the time domain. Each of these analyses has different requirements for setting up the numerical model. Section 5.3.1 presents the numerical model utilised and the iterative procedure followed for nonlinear static aeroelastic analyses. Section 5.3.2 presents the governing equations for the flutter analyses, which are conducted using the full-order model. Section 5.3.3 focuses on the reduced-order nonlinear dynamic aeroelastic model, which is solved in the time domain.

5.3.1. Iterative process for nonlinear static aeroelastic analyses

The implementation of the aerodynamic model, discussed in Section 5.1, can now be utilised for nonlinear aeroelastic analyses. Due to the consideration of geometric nonlinearities, the displacements are nonlinearly related to the aerodynamic loads. Therefore, it is not possible to obtain a solution from a single inversion of the combined aeroelastic stiffness matrix, unlike in a linear model. Therefore, an iterative process is set up to conduct the nonlinear static aeroelastic analyses. Figure 5.3 shows a flow diagram of the nonlinear aeroelastic process. The reduced order model based on the K-N method (Liang, 2013) is integrated into this approach.

The aeroelastic coupling of the full-order model with the aerodynamics model is achieved using the method described in Section

5.2. The aerodynamic loads are applied to the reference points on the FE model, which are located at the mid-chord positions of the wing sections. In the initial step, the wing twist at all sections is assumed to be zero; therefore, the aerodynamic loads are computed based on the angle of incidence of the airflow with respect to the camber line of the airfoil section. With application of the aerodynamic load $\boldsymbol{F}_{aero,}$ the nonlinear static equation of motion can be written as:

$$\boldsymbol{Ku} + \boldsymbol{Quu} + \boldsymbol{Cuuu} = \boldsymbol{F}_{aero} \tag{5.12}$$

where $\boldsymbol{u}$ is the displacement variable, $\boldsymbol{K}$, $\boldsymbol{Q}$ and $\boldsymbol{C}$ are the stiffness tensors of the full order model. $\boldsymbol{F}_{aero}$ is a sparse vector where the non-zero terms are defined as the total lift and moment for each strip and applied at the nodes corresponding to the reference points. The total lift and moment for the j^{th} strip is computed as:

$$L^j_{total} = L_0 b^j_s W_j, \; M^j_{total} = M_0 b^j_s W_j \tag{5.13}$$

where b^j_s is the length of the strip in the spanwise direction and W_j is the weight factor for tip loss correction computed at the spanwise position of the corresponding coupling point, L_0 and M_0 are as defined in Eqs. 5.2 and 5.3.

The K-N method, previously described in Section 2.1, can be applied to Eq. 5.12 for obtaining the governing equations in the ROM subspace, described as:

$$\bar{\boldsymbol{K}}\boldsymbol{\xi} + \bar{\boldsymbol{Q}}\boldsymbol{\xi\xi} + \bar{\boldsymbol{C}}\boldsymbol{\xi\xi\xi} = \boldsymbol{\phi}_{aero} \tag{5.14}$$

where ξ is the generalised displacement in the ROM subspace, $\overline{\boldsymbol{K}}$, $\overline{\boldsymbol{Q}}$ and $\overline{\boldsymbol{C}}$ are reduced order stiffness tensors and $\boldsymbol{\phi}_{aero}$ is the reduced order aerodynamic force vector.

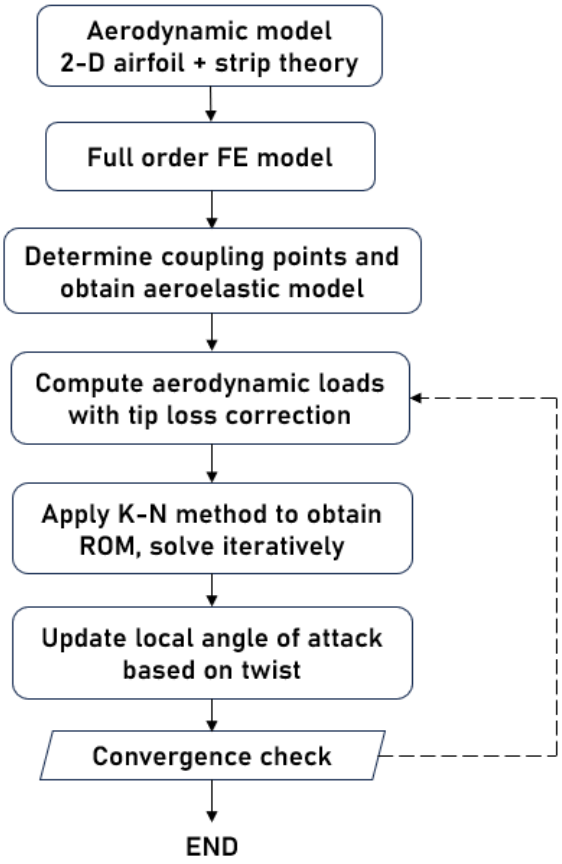

Figure 5.3: Flow diagram for the nonlinear static aeroelastic process

The solution of the nonlinear ROM is obtained iteratively using the Newton-Raphson method. The obtained deformation provides information about the wing twist θ_s which is then used to update the effective angle of attack of the wing. For any given section, the effective

angle of attack is $\alpha = \alpha_r + \theta_s$. Aerodynamic loads are updated with the new effective angle of attack, and the nonlinear static equation is solved again using the K-N method. This process is repeated until a convergence in loads and displacements is observed. A relative tolerance of 0.001 is applied for both loads and displacements in the convergence check. The error is computed with respect to the loads and displacements obtained in the previous iteration.

5.3.2. Flutter analyses of wings with geometrically nonlinear deformation

The flutter phenomenon refers to the state of aeroelastic instability that occurs when aeroelastic modes are coupled in the presence of unsteady aerodynamic forces. A commonly known engineering approach of solving the flutter problem is the *p*-method (Wright and Cooper, 2008). It involves transforming the coupled aeroelastic system into a state-space model, on which an eigenvalue analysis can be performed. In the coupled form, due to the non-symmetric nature of the aerodynamic terms and the presence of damping, complex eigenvalues are obtained. The real parts of these eigenvalues provide information about the decay rate and damping, while the imaginary part provides information about the frequency of damped oscillations. If the real part of the complex eigenvalue becomes positive, then the system becomes unstable (Wright and Cooper, 2008).

The nonlinear flutter characteristics of the Pazy wing have been well investigated numerically and experimentally (Ritter et al., 2024). The studies show that the flutter boundary shifts with increasing angle of attack and wing deflection. The general trend observed is a reduction in the flutter onset and offset speeds with increasing angle of attack. To conduct the flutter analysis, first, the nonlinear static aeroelastic

equilibrium of the wing is computed for the prescribed angle of attack and flow speed. The system is then linearised in the deformed state, and an eigenvalue analysis is conducted using the stiffness, damping and mass matrices obtained in the deformed state. Note that the eigenvalue analyses are conducted using the full-order model. The process can be repeated for various flow speeds to obtain the variation of frequencies and damping with the flow speeds. Commonly used flutter analysis tools employ methodologies for mode tracking to obtain these variations. In the present work, a frequency search is performed within the range of 4 to 40 Hz. The corresponding values of the decay rates for all identified frequencies in the specified range are then extracted.

The aerodynamic stiffness, damping and mass matrices are required to perform the flutter analysis. These are obtained by assembling the coefficients of $[h\ \theta]'$, $\left[\dot{h}\ \dot{\theta}\right]'$ and $\left[\ddot{h}\ \ddot{\theta}\right]'$, respectively, in the Eqs. 5.2 and 5.3 where the superscript prime indicates the transpose of the vectors.

The aerodynamic stiffness $\boldsymbol{k}_{aero}^{j}$ for the j^{th} airfoil section is defined as:

$$\boldsymbol{k}_{aero}^{j} = \begin{bmatrix} 0 & 2\pi\rho b_j U^2 \\ 0 & -2\pi\rho U^2 b_j^2 \left(\frac{1}{2} + a_j\right) \end{bmatrix} \tag{5.15}$$

The aerodynamic damping $\boldsymbol{d}_{aero}^{j}$ for the j^{th} airfoil section is defined as:

$$\boldsymbol{d}_{aero}^{j} = \begin{bmatrix} 2\pi\rho U b_j & 2\pi\rho U b_j^2 (1 - a_j) \\ -2\pi\rho U b_j^2 \left(\frac{1}{2} + a_j\right) & -\pi\rho U b_j^3 a_j (1 - 2a_j) \end{bmatrix} \tag{5.16}$$

Similarly, the corresponding aerodynamic mass matrix $\boldsymbol{m}_{aero}^{j}$ for the j^{th} airfoil section is defined as:

$$\boldsymbol{m}_{aero}^{j} = \begin{bmatrix} \pi\rho b_j^2 & \pi\rho a_j b_j^3 \\ \pi\rho a_j b_j^3 & \pi\rho b_j^4 \left(\frac{1}{8} + a_j^2\right) \end{bmatrix} \tag{5.17}$$

where a_j and b_j are as defined in Fig. 5.1 and the subscript *j* indicates that they may vary for different strips.

The Eqs. 5.15-5.17 are based on the lift and moment per unit span. Therefore, to evaluate the strip-wise contribution of the aerodynamic terms, these are multiplied by the spanwise strip length b_s^j. Furthermore, the effect of the tip loss correction factors is included by multiplying the matrices by the weight factor W_j. It is recalled from Eq. 5.11 that the aerodynamics model follows a different sign convention than the FE model. The aerodynamic terms, therefore, require the application of a coordinate transformation $\boldsymbol{T}$ = [-1 0, 0 1] before assembly into the global matrices. The matrices derived from individual airfoil sections are assembled into global aerodynamic matrices $\boldsymbol{K}_a$, $\boldsymbol{D}_a$ and $\boldsymbol{M}_a$, which represent the aerodynamic stiffness, damping and mass, respectively. These are constructed as sparse matrices of the same size as defined in the FE model, where the non-zero terms correspond to the reference points of each airfoil section. The aerodynamic terms are then added to the structural counterparts $\boldsymbol{K}$, $\boldsymbol{D}$, and $\boldsymbol{M}$, which are obtained from the FE model. Effectively, the linearised aeroelastic equation of motion of the full order model can be defined as:

$$(\boldsymbol{M} + \boldsymbol{M_a})\ddot{\boldsymbol{u}} + (\boldsymbol{D} + \boldsymbol{D_a})\dot{\boldsymbol{u}} + (\boldsymbol{K} + \boldsymbol{K_a})\boldsymbol{u} - \boldsymbol{F}_{aero}(\boldsymbol{\lambda_0}) = \boldsymbol{0} \tag{5.18}$$

where $\boldsymbol{F}_{aero}(\boldsymbol{\lambda_0})$ comprises the components of lift and moment in Eqs. 5.2. and 5.3, which are only dependent on $\boldsymbol{\lambda_0}$, and $\boldsymbol{u}$ is the displacement vector.

To conduct the flutter analyses, Eqs. 5.6 and 5.18 are combined. Further, to set up the eigenvalue problem, the system is transformed into a set of first-order differential equations. To this end, the trivial equation $\boldsymbol{I}\dot{\boldsymbol{u}} - \boldsymbol{I}\dot{\boldsymbol{u}} = \boldsymbol{0}$ is appended to the aeroelastic system, where $\boldsymbol{I}$ is an identity matrix. The system of equations can then be restructured into the form of $\boldsymbol{A}\dot{\boldsymbol{q}} = \boldsymbol{B}\boldsymbol{q}$ where $\boldsymbol{q} = [\boldsymbol{u}\ \dot{\boldsymbol{u}}\ \boldsymbol{\lambda_0}]'$. The assembly of the matrices $\boldsymbol{A}$ and $\boldsymbol{B}$ for the flutter analyses are described further in Appendix V.

5.3.3. Reduced-order nonlinear dynamic aeroelastic model

The flutter analysis performed on the deformed wing under the specified conditions shows a region of flutter instability. While such an analysis is useful for understanding the conditions under which a system becomes unstable, it provides no information on how the system behaves when the flow speed is further increased. The post-flutter dynamic analyses enable us to assess if the aeroelastic system would survive the region of instability. These analyses, when conducted using full order models, can be computationally expensive. This Section presents a reduced order nonlinear dynamic aeroelastic model which utilises a combination of the K-N method and the unsteady aerodynamics model based on Peters theory. Such a coupling has been previously discussed in Section 5.3.1 for nonlinear static aeroelastic analyses; however, this model differs in the following ways:

- The momentum subspace variant of the K-N method (Sinha et al., 2020) is utilised to include inertial and damping terms.

- The induced flow dynamics described by Eq. 5.6 is solved simultaneously with the aeroelastic equations in the time domain.

In the preliminary steps, nonlinear static aeroelastic analyses are conducted for a given combination of flow speed and root angle of attack to obtain the nonlinear wing deformation. The procedure described in Section 5.3.1 is used to obtain the wing deformations. Using the wing deformation as an input, structural ROMs are computed for each deformed equilibrium state. The momentum subspace formulation, discussed in Chapter 3, is utilised for obtaining the structural ROM. Considering Eq. 5.6, a first-order differential equation has been defined for the induced flow variable in accordance with the Peters theory. Therefore, to solve the coupled nonlinear dynamic aeroelastic equation, it is ideal to transform the structural ROM into the form of a first-order differential equation. A transformation to first-order differential equations based on Hamiltonian mechanics has been previously presented by (Sinha et al., 2020). The structural ROM equations are therefore described as:

$$\dot{\boldsymbol{\xi}} = \bar{\boldsymbol{M}}^{-1}\boldsymbol{\pi} \tag{5.19}$$

$$\dot{\boldsymbol{\pi}} = -(\bar{\boldsymbol{K}}\boldsymbol{\xi} + \bar{\boldsymbol{Q}}\boldsymbol{\xi}\boldsymbol{\xi} + \bar{\boldsymbol{C}}\boldsymbol{\xi}\boldsymbol{\xi}\boldsymbol{\xi}) - \bar{\boldsymbol{D}}\bar{\boldsymbol{M}}^{-1}\boldsymbol{\pi} + \boldsymbol{\phi}(t) \tag{5.20}$$

where $\boldsymbol{\pi}$ is the momentum variable and $\boldsymbol{\xi}$ is the generalised displacement variable in the ROM subspace, $\bar{\boldsymbol{M}}$ is the reduced mass matrix, $\bar{\boldsymbol{D}}$ is the reduced damping matrix, $\bar{\boldsymbol{K}}$, $\bar{\boldsymbol{Q}}$ and $\bar{\boldsymbol{C}}$ are the stiffness tensors and $\boldsymbol{\phi}(t)$ is the reduced force vector.

The coupling of the aerodynamic model is performed using the approach discussed in Section 5.2. The sectional aerodynamic stiffness, damping and mass matrices are evaluated using the Eqs. 5.15-5.17,

respectively. The aerodynamic matrices are assembled to form sparse matrices because of the independent aerodynamic strips, which have the same size as the full-order FE model. To combine these with the ROM equations, the reduction method must be applied to these matrices. The total reduced mass matrix is computed using Eq. 3.8. Similarly, the reduced damping matrix is obtained using Eq. 3.12. To reiterate, the total reduced mass $\bar{\boldsymbol{M}}_{tot}$ and damping $\bar{\boldsymbol{D}}_{tot}$ terms are defined as:

$$\bar{\boldsymbol{M}}_{tot} = \bar{\boldsymbol{M}} + \bar{\boldsymbol{M}}_a = (\boldsymbol{\Phi}'(\boldsymbol{M}_a + \boldsymbol{M})\boldsymbol{\Phi})^{-1} \tag{5.21}$$

where $\boldsymbol{\Phi}$ is a basis matrix comprising structural eigenmodes, $\boldsymbol{M}$ is the structural mass matrix and $\boldsymbol{M}_a$ is the aerodynamic mass matrix.

$$\bar{\boldsymbol{D}}_{tot} = \bar{\boldsymbol{D}} + \bar{\boldsymbol{D}}_a = \bar{\boldsymbol{M}}_{tot}(\boldsymbol{\Phi}'(\boldsymbol{D_a} + \boldsymbol{D})\boldsymbol{\Phi})\bar{\boldsymbol{M}}_{tot}^{-1} \tag{5.22}$$

where $\boldsymbol{D}$ is the structural damping and $\boldsymbol{D_a}$ is the aerodynamic damping**.**

Next, the reduced aerodynamic stiffness matrix $\bar{\boldsymbol{K}}_a$ is constructed. A direct approach to this is by utilising Eq. 3.3. Liang (2013) proposed an alternative method for computing the linear component of the reduced-order stiffness matrix. This approach is equivalent to the modal reduction approach that is commonly applied to linear models, and is described as:

$$\bar{\boldsymbol{K}}_a = \boldsymbol{u}'_\alpha \boldsymbol{K}_a \boldsymbol{u}_\alpha \tag{5.23}$$

where $\boldsymbol{K}_a$is the global assembly of the aerodynamic stiffness matrix and $\boldsymbol{u}_\alpha$ is the first-order displacement field obtained from the ROM construction process applied to the structural model. Combining Eq. 5.6 with Eqs. 5.19-5.23, the reduced-order nonlinear aeroelastic model can be constructed as:

$$\begin{bmatrix} \dot{\boldsymbol{\xi}} \\ \dot{\boldsymbol{\pi}} \\ \dot{\boldsymbol{\lambda}}_j \end{bmatrix} \tag{5.24}$$

$$= \begin{bmatrix} (\bar{\boldsymbol{M}} + \bar{\boldsymbol{M}}_{\boldsymbol{a}})^{-1}\boldsymbol{\pi} \\ -\left((\bar{\boldsymbol{K}} + \bar{\boldsymbol{K}}_{\boldsymbol{a}})\boldsymbol{\xi} + \bar{\boldsymbol{Q}}\boldsymbol{\xi}\boldsymbol{\xi} + \bar{\boldsymbol{C}}\boldsymbol{\xi}\boldsymbol{\xi}\boldsymbol{\xi}\right) - (\bar{\boldsymbol{D}}_a + \bar{\boldsymbol{D}})\dot{\boldsymbol{\xi}} + \boldsymbol{\phi}(t) + \boldsymbol{\phi}_{\boldsymbol{a}}(t, \boldsymbol{\lambda}_{\mathbf{0}}) \\ \bar{\boldsymbol{A}}^{-1}\left(\bar{\boldsymbol{c}}\left[\ddot{h} + U\dot{\theta} + b\left(\frac{1}{2} - a\right)\ddot{\theta}\right] - \frac{U}{b}\boldsymbol{\lambda}_j\right) \end{bmatrix}$$

where $\boldsymbol{\lambda_j}$ represents the aerodynamic states of the j^{th} strip on the aerodynamic lifting surface, and *j* varies from 1 to the number of strips defined in the aerodynamics model, as shown in Fig. 5.2. In Eq. 5.24, note the presence of the plunge variable *h,* which is described in the aerodynamic coordinate system. Therefore, the relation defined in Eq. 5.11 between the FE coordinate system and the aerodynamic coordinates system applies here. The procedure to obtain Eq. 5.24 is also described using the flow diagram in Fig. 5.6.

The computation of $\boldsymbol{\phi}(t)$**,** which is the force vector in the ROM subspace, can be done using Eq. 3.13. In a general case of time domain flutter simulation, $\boldsymbol{\phi}(t)$ consists of a perturbation load acting for a short time period and is thereafter zero. In this formulation, due to the presence of an aerodynamic force component, which is a function of the induced flow variable $\boldsymbol{\lambda_0}$, as shown in Eqs. 5.2-5.3, the effective force remains non-zero throughout the simulation time. This term is not directly accounted for in the formation of the aerodynamic stiffness, damping and mass matrices and is therefore retained in Eq. 5.24 as $\boldsymbol{\phi_a}(t, \boldsymbol{\lambda_0})$. The size of the resultant matrices in Eq. 5.24 depends on the number of eigenmodes utilised for generating the structural ROM, and additionally, the number of induced flow states considered in the Peters theory, along with the number of strips.

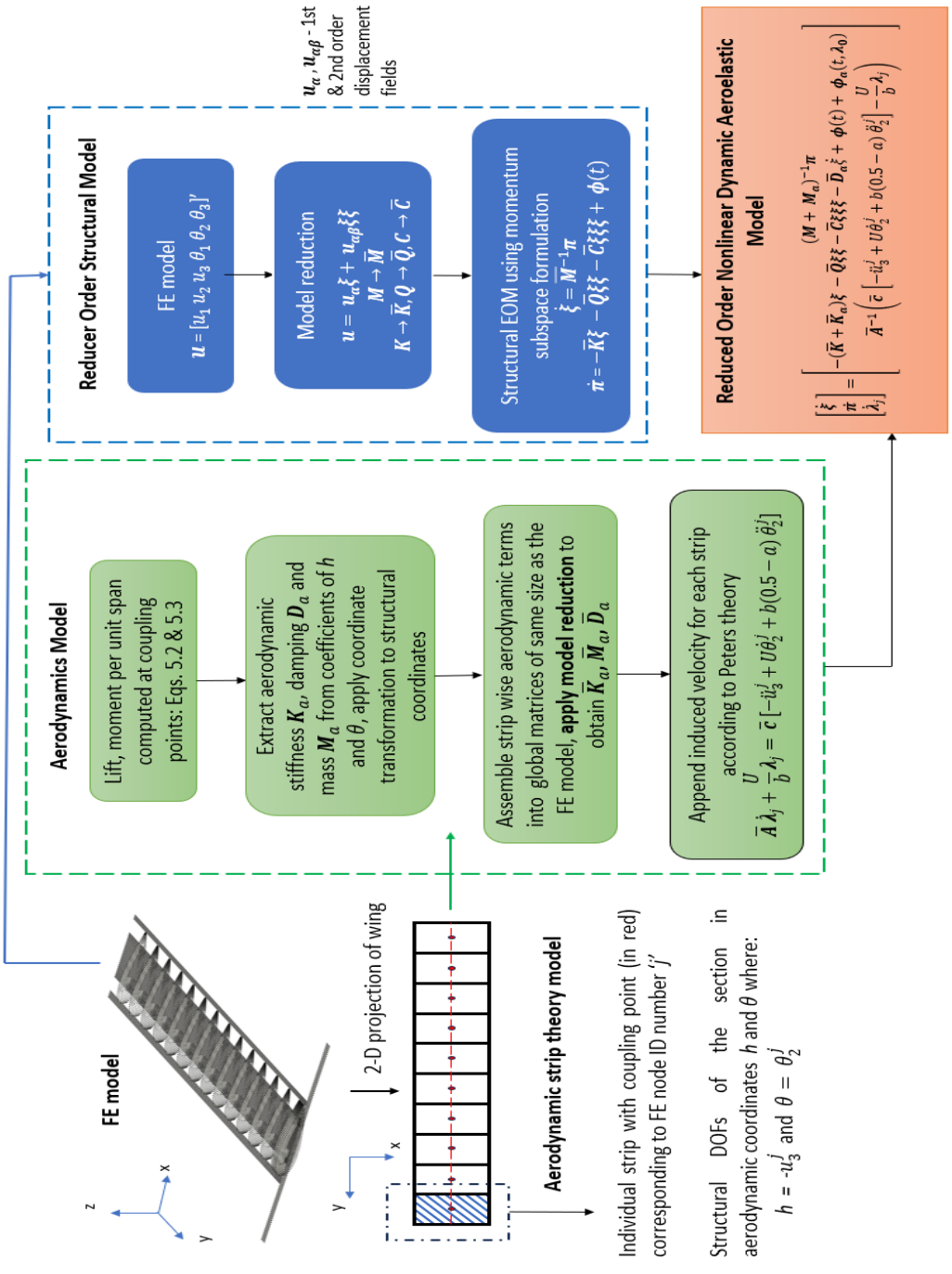

Figure 5.6: Procedure for obtaining the reduced-order nonlinear dynamic aeroelastic model

Equation 5.24 can be solved using a suitable time-integration scheme for first-order nonlinear differential equations to obtain the generalised displacements and velocities. The ODE45 solver in MATLAB, which is commonly utilised, for example by Vio et al. (2007) and Padmanabhan et al. (2017), is employed in the present work. The accelerations are computed using the finite-difference approximation.

5.4. NUMERICAL STUDIES

This section presents the results of the numerical studies conducted using the aeroelastic models described in Section 5.3. The Pazy wing, previously discussed in Section 4.1, is used as the analysis model. First, nonlinear static aeroelastic analyses are conducted. The objective of these analyses is to obtain aeroelastic equilibrium states under various prescribed flow speeds and angles of attack. The results of these analyses are presented in Section 5.4.1. Next, flutter analyses of the deformed wing are conducted to predict the region of instability of the Pazy wing. The results of the flutter analyses are presented in Section 5.4.2. Finally, the post-flutter dynamics of the Pazy wing are investigated, and the results are presented in Section 5.4.3.

5.4.1. Nonlinear static aeroelastic analysis of the Pazy wing

The iterative nonlinear static aeroelastic process is now applied to the Pazy wing, and the results are compared to the linear analyses. In Section 4.1, the modelling strategy of the Pazy wing is discussed, and it is highlighted that due to modelling adaptations related to the conversion from beam elements to shell elements, the structural dimensions differ from the original design. The dimensions of the lifting surface in the aerodynamic model are defined consistent with the original model, i.e. a rectangular surface with a span of 0.55 m and a width of 0.10 m. Three

test cases are chosen for comparison to the linear model, as described in Table 5.1. In the structural solver, six load increments are fixed based on the discussions in Chapter 4, where it is shown that further increase in load increments only marginally improves the accuracy of the solution while significantly increasing the computational time. The follower force effect is considered in these analyses as the aerodynamic loads are pressure forces that act normal to the surface. The tuning coefficients corresponding to the tip loss correction factors for the root angle of attack α_r = 7^0 are computed with consideration of reference UVLM solutions obtained for three flow speeds *U* = 10, 30 and 55 m/s. The computed tuning coefficients are: $\tau_0 = 4.76, \tau_1 = 0.0438$, and $\tau_2 = -0.0011$. For α_r = 5^0, the tuning coefficients discussed in Section 5.2 can be utilised. The nonlinear static aeroelastic analysis results are presented in Fig 5.4.

Table 5.1: Test cases for nonlinear static aeroelastic analyses

Case	**Flow speed *U*** [m/s]	**Angle of attack** [^{0}]
1	30	7
2	50	5
3	55	7

Data from four analyses involving different solvers are compared in the figure: linear analysis using Peters theory, linear analysis using the UVLM tool, nonlinear analysis using the K-N method coupled to the aerodynamics model based on Peters theory and nonlinear analysis in the SOL400 solver of MSC NASTRAN. The loads applied in the NASTRAN analysis are the converged loads obtained from the final iteration of the analysis conducted using the K-N method. A significant

difference is seen between the linear and nonlinear results at larger amplitudes achieved through the conditions specified in Case 3. In Case 1, the maximum tip deflection is approximately 15% of the span, and there is no significant difference between the linear and nonlinear results. In Case 2, the tip deflections exceed 30% of the span; however, the nonlinear transverse displacement differs only by around 4% from the linear results. Comparing the wing twist at the mid-chord position, it is evident that despite the tuning process, some differences exist in the solutions based on the UVLM and Peters theory in the linear case. This is attributed to the different FE formulations used in the two models. The UVLM tool utilises stiffness matrices obtained from MSC NASTRAN. It has previously been demonstrated in Chapter 2, using the high-aspect-ratio wingbox example, that the FE formulation employed in the present work yields different wing twists compared to NASTRAN. Nevertheless, the errors are within a 4% margin for twist estimation. Furthermore, a clear distinction can be made between the linear and nonlinear twists at higher flow speeds.

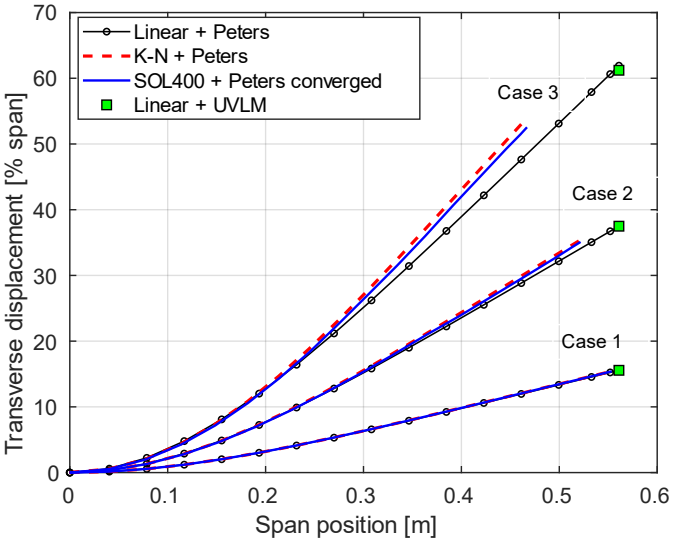

(a)

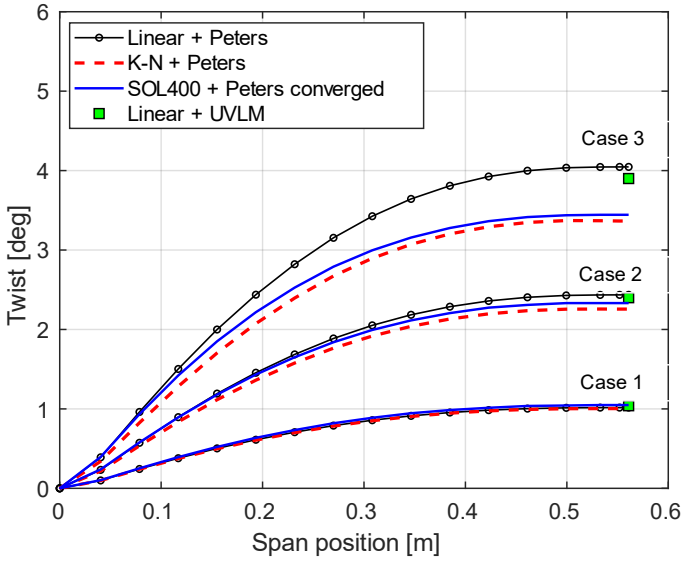

(b)

Figure 5.4: Nonlinear static aeroelastic displacements (a) and twist (b) of the Pazy wing compared to the linear results, cases 1-3 refer to the Table 5.1

5.4.2. Flutter analysis of the Pazy wing

The flutter analysis follows the procedure described in Section 5.3.2. The objective of this analysis is to obtain the flow speeds at which the aeroelastic system becomes unstable. Aeroelastic modal frequencies and decay rates are computed at several flow speeds through eigenvalue analyses. A fixed root angle of attack α_r = 5° is considered in these analyses. Figure 5.5 shows the variation of the frequencies and the decay rate of the first three aeroelastic modes with respect to the flow speeds. As shown in Fig. 5.5(a), the frequency corresponding to the first torsion mode (T1) decreases and approaches the frequency of the second bending mode (OOP2) as the flow speed increases.

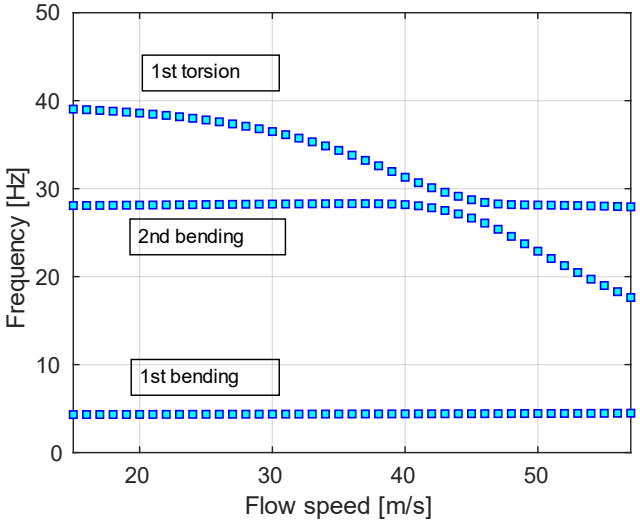

(a)

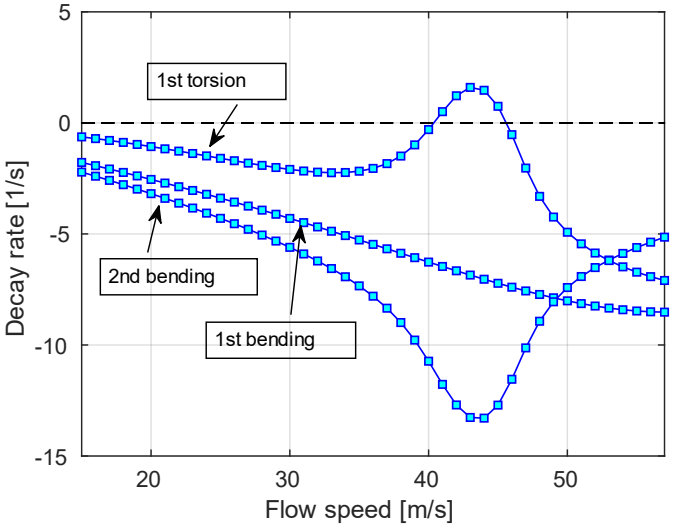

(b)

Figure 5.5: Modal Frequency (a) and decay rate (b) variation of the deformed Pazy wing at the angle of attack 5^0 computed at various flow speeds

A reduction of 21.6% in the frequency of T1 is seen between the flow speeds U = 15 m/s and U = 40 m/s. The frequency of the first bending mode (OOP1) changes by only 3.5% over the entire range of flow speeds considered in the analysis.

Referring to Fig. 5.5(b), it is observed that the decay rate corresponding to the third mode, i.e. the torsion mode, becomes positive at around 40.3 m/s and subsequently, becomes negative again at around 45.5 m/s. This is indicative of a typical hump mode flutter instability. Collective results from the third aeroelastic prediction workshop, presented by Ritter et al. (2024), discuss similar traits observed in the computations done by several researchers. The reference model is observed to have a flutter onset speed of 43 m/s and a flutter offset speed of 48 m/s, as determined during experimental measurements (Drachinsky et al., 2022). As discussed in Chapter 4, some variations from the reference model are expected due to the comparatively lower stiffness of the FE model utilised in the present work.

5.4.3. Post-flutter dynamics of the Pazy wing

This Section presents the results of post-flutter dynamic analyses of the Pazy wing. In Section 5.4.3.1, the problem setup for time domain simulations and the corresponding results are presented. In Section 5.4.3.2, the focus is on the envelope formed by the LCO amplitudes as the flow speed is increased from the flutter onset speed and the bifurcation characteristics of the Pazy wing.

5.4.3.1. Time domain simulations in the region of flutter instability

In Section 5.4.2, using linearised eigenvalue analyses, a region of instability for the Pazy wing was predicted to be between the flow speeds

of 40.3 m/s and 45.5 m/s. The time domain analyses simulate the behaviour of the model within the region of instability. It is noted from the frequency variation plot in Fig. 5.5 and the discussions in Section 5.4.2 that immediately after flutter onset occurs, the frequency of the first torsion mode reaches 30.7 Hz, while the frequency of second bending mode is 28.05 Hz. The proximity of these frequencies indicates enhanced modal interactions and increased likelihood of flutter. It has been shown previously in Section 4.3 that a 1-DOF reduced-order model is capable of capturing the structural dynamic response comparable to that of the full-order model. However, since the instability in this case closely relates to the first torsion mode, as shown in Fig. 5.5(b), the ROM is formulated using the first three eigenmodes to obtain a 3-DOF reduced-order model. In fact, preliminary analyses have shown that the LCO response is not captured if the ROM is formulated without including the third eigenmode in the reduction basis, see Appendix VI.

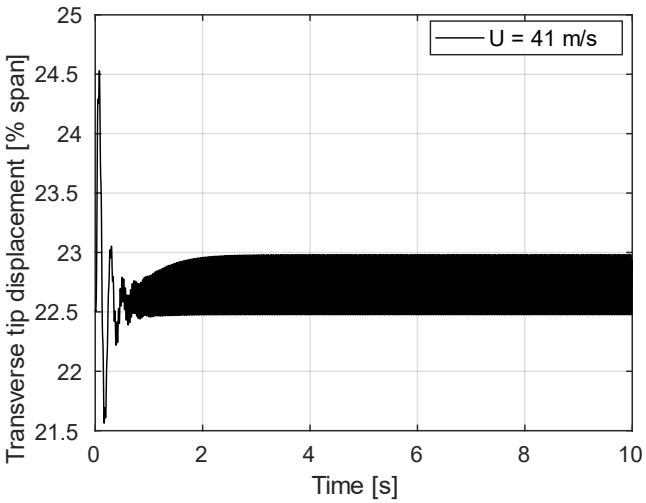

(a)

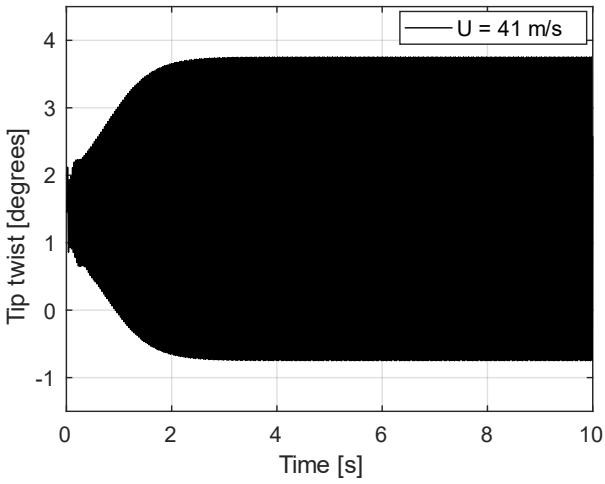

(b)

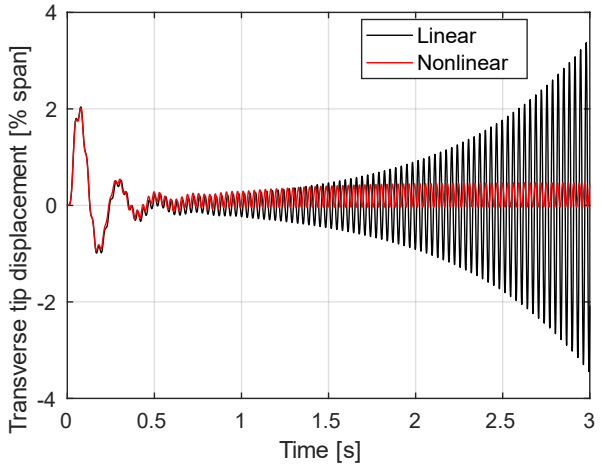

(c)

Figure 5.6: Limit cycle oscillations occurring at *U* = 41 m/s, root angle of attack $\alpha_r = 5^0$, maximum gust velocity w_{max}= 1 m/s: (a) transverse displacements, (b) tip twist, (c) comparison to linear response

The coupling approach for the aerodynamic model with the FE model, as described in Section 5.2.1, is retained for these analyses. Since the wing span is divided into 15 strips and N = 6 induced flow states for each strip are assumed, a total of 90 aerodynamic DOFs are added to the aeroelastic model. Structural damping is not considered in these simulations. Generally, structural damping results in a delayed onset of flutter (Wright and Cooper, 2022). The exclusion of structural damping, therefore, provides a conservative estimate of the flutter speed.

A time domain simulation is first performed at the flow speed U = 41 m/s, which is about 2% beyond the flutter onset speed predicted by the eigenvalue analysis of the deformed wing. Considering the root angle of attack $\alpha_r = 5^0$, the nonlinear static aeroelastic equilibrium is computed using the procedure described in Section 5.3.1. The wing deformation obtained through this analysis is used as the reference position for constructing the structural ROM. The structural ROM is coupled to the aerodynamics as described in Eq. 5.24. The time integration is conducted for a total time of 10 s with a time step of 0.0005 s.

A 1- *cos* perturbation load is applied to the system using a vertical gust velocity w_g, which follows the profile given by:

$$w_g = w_{max}\left(1 - \cos\frac{2\pi t}{T}\right) \tag{5.25}$$

where w_{max} is the peak gust velocity, and T is the time period of oscillation. In this case, the excitation frequency is chosen to be 30 Hz since the second bending and first torsion modes approach this value in the region of the predicted instability.

Figures 5.6 (a), (b) depict the time history of the transverse tip deflection at the mid-chord position of the wing as a % of the wing span. After the excitation peak, the response settles down into a limit cycle oscillation. The dynamic response is superimposed over the nonlinear static aeroelastic equilibrium; thus, it is observed that peak displacements reach approximately 24.5% of the span. However, the transverse displacements at the mid-chord position occurring in the LCO are limited to less than 0.5 % of the span. The tip twist at the mid-chord oscillates between 3.75^0 and -0.75^0. The oscillations in the transverse displacements appear to have an offset from the equilibrium position, which is reflected as an asymmetry in the response. This occurs due to the higher-order stiffness components in the nonlinear structural model. The quadratic stiffness component, which is otherwise approaching zero for an undeformed geometry, attains a finite value for the deformed wing. Since the quadratic stiffness is related to the square of the displacements, regardless of the sign of the displacements, the corresponding restoring force is always in the same direction. Thus, unlike the linear and cubic terms, which follow the sign of the displacements, the quadratic component creates an asymmetry.

The LCO response obtained in these simulations can be attributed purely to the structural nonlinearities, as a linear aerodynamics model has been utilised in these analyses. For comparison, the same analysis is conducted using a linear structural model. Figure 5.6 (c) shows the evolution of the tip displacements as a function of time for the linear model and compares it to the nonlinear response. For clarity in the comparison, the displacements are only shown up to 3 s of simulation time; it is evident that the linear model rapidly undergoes an increase in tip displacements. Simulating beyond the 3 s time results in exponential growth in the tip displacements, indicating the occurrence of a hard flutter.

The symmetry about the equilibrium position in the linear response is also observable, which aligns with the previous discussions about the effect of the quadratic stiffness. The LCO simulation with the described analysis settings requires 5.06 minutes for completion. The utilisation of the 3-DOF structural ROM, obtained from the K-N method, in the aeroelastic model ensures faster simulation times. In comparison, the equivalent beam model of the Pazy wing (discussed in Chapter 2 and Appendix II) comprises 96-DOFs.

5.4.3.2. Envelope of the limit cycle oscillation

The hump mode instability, shown in Fig. 5.7 (b), indicates that when the flow speed is outside the flutter instability boundaries predicted in Section 5.4.2, the aeroelastic system is in a state of stable equilibrium. In this state of equilibrium, external perturbations cause oscillations that eventually damp out. Figure 5.7(a) shows the time histories of the tip transverse displacements at the trailing edge obtained at different flow speeds ranging from U = 39 m/s to 47 m/s. For each flow speed, the initial condition is assumed to be the corresponding nonlinear static aeroelastic equilibrium. In all the cases analysed, the tip-to-tip oscillation magnitude of the maximum transverse deflection is less than 1.3 % while the twist is limited to 2.2^0. In comparison, other studies on the Pazy wing using the geometrically exact beam model have predicted higher LCO amplitudes: up to 1.56 % in transverse displacements (Riso and Cesnik, 2022) and up to 6.2^0 in twist (Pancini dos Santos, 2024). Nevertheless, the numerical model used in the present work is able to capture the expected LCO behaviour arising from nonlinearities within the boundaries of flutter onset and offset, as predicted by the eigenvalue analysis. The bifurcation characteristics of the dynamical system are assessed by considering the maximum and minimum amplitudes of the transverse displacements and

twists attained during the LCO, plotted against the airspeed normalised by the flutter speed.

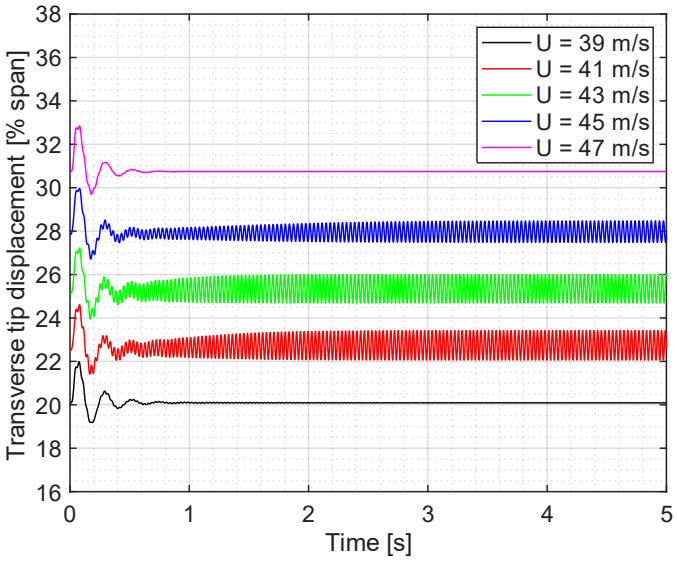

(a)

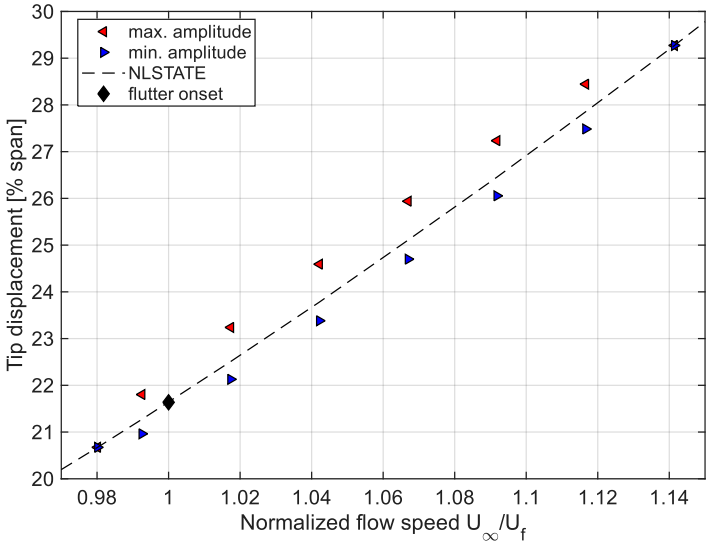

(b)

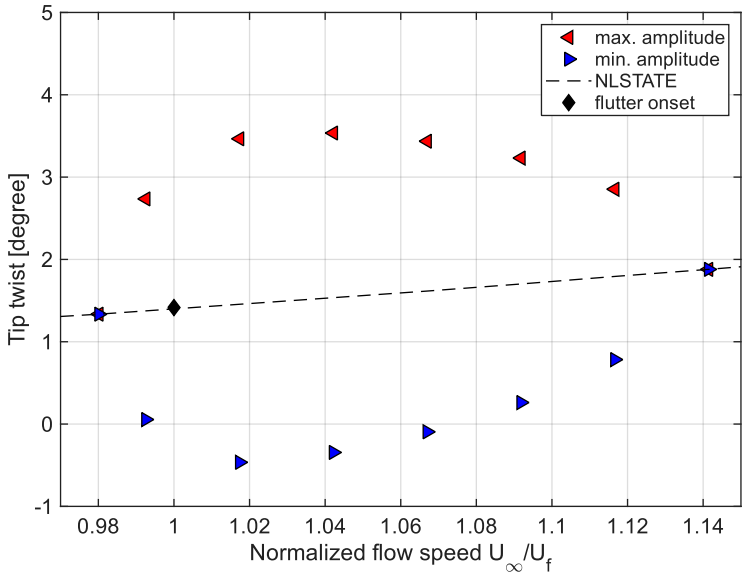

(c)

Figure 5.7: Variation of the maximum LCO amplitudes across the region of instability (a) time histories of the tip displacements at the trailing edge, (b) tip transverse displacements, and (c) tip twist across normalised air flow speeds, NLSTATE: nonlinear static aeroelastic equilibrium

Figure 5.7 (b) and (c) show the variation in amplitudes across the various airflow speeds. The tip transverse displacements and tip twist are plotted against the normalised flow speed. The LCO appears in the time domain analyses before the flutter speed predicted through the eigenvalue analyses. The general trend follows an increase in the LCO amplitudes up to approximately 2% above the flutter speed, and then gradually decreases until the LCO vanishes outside the flutter offset speed. The finite LCO oscillations and the hysteretic effect, which lead to the existence of oscillations below the flutter speed, indicate subcritical

behaviour. However, the model does not exhibit sensitivity to initial conditions or the coexistence of stable states below the bifurcation point, a characteristic typically associated with subcritical bifurcations.

A comparison of the LCO response to different initial gust perturbations is shown in Fig. 5.8. Regardless of the perturbation, the LCO response settles down to the same oscillation amplitude. The main difference observed is a phase difference between the responses. This occurs because the model settles down into the LCO more quickly for larger perturbations and relatively slowly for small perturbations. These results, therefore, are indicative of a supercritical bifurcation. The overall trend observed after the bifurcation occurs, along with the lack of sensitivity to the initial conditions, is in accordance with the results discussed in (Riso and Cesnik, 2022), where the authors conclude that the bifurcation is of a supercritical nature.

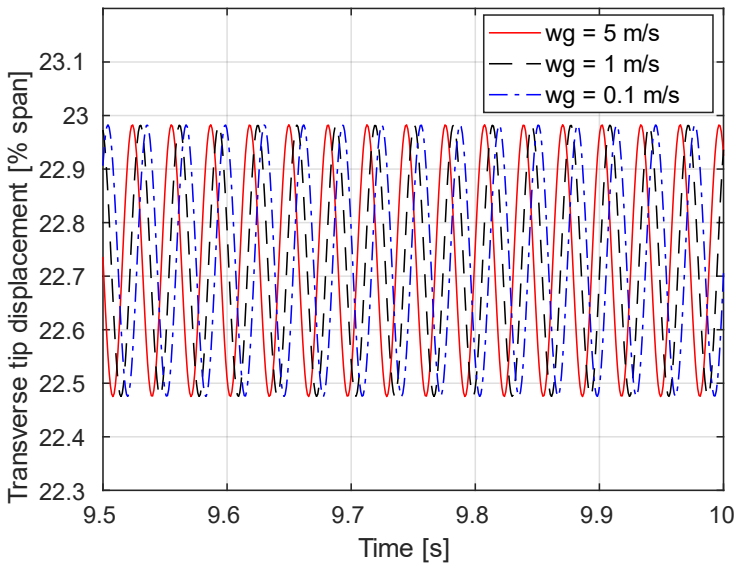

Figure 5.8: Sensitivity of the LCO response to initial gust perturbations, computed below the flutter onset speed, at U= 40 m/s

Table 5.2: Comparison of flutter characteristics of the Pazy wing at $\alpha_r = 5^0$ obtained through: present model, UMNAST (Riso and Cesnik, 2022; Pancini dos Santos et al., 2024) and experiments (Drachinsky et al., 2022)

	Present model	**UMNAST**	**Experiments (up sweep)**
Flutter onset (m/s)	40.3	43.2	43
Flutter offset (m/s)	45.5	47.1	48
Max. transverse displacement (% span)	< 1.3	1.56	1.2
Max. twist (degrees)	$\pm$2.2	$\pm$6.2	< 10.0

In contrast, the experiments performed on the Pazy wing captured a subcritical behaviour where a clear hysteretic effect is observed when sweeping the airspeed in opposite directions (Drachinsky et al., 2022). The authors, however, attributed the subcritical behaviour to aerodynamic nonlinearities due to dynamic stall. The transverse deformations observed in the experiments are relatively small, whereas the tip twist exceeds amplitudes which are conducive to nonlinear aerodynamic effects. In the present model, the wing twist captured during the LCO is comparatively lower, which leaves no possibility of any

influence from aerodynamic nonlinearities. Interestingly, strain data obtained from the experiments were analysed by the authors, and they were also found to be insensitive to the initial conditions tested, despite the hysteretic behaviour occurring, as reported by Drachinsky et al. (2022). For clarity in comparison, Table 5.2 summarises the main results of the nonlinear aeroelastic analyses. Note that during the experiments, the air speed sweep rate does not allow the wing dynamics to settle down into an LCO response; therefore, the maximum displacements and twist during the flutter onset are reported.

5.5. CONCLUSIONS

A numerical framework involving a reduced-order nonlinear aeroelastic model is presented in this Chapter. The numerical model is developed by combining a structural FE model with the low-fidelity aerodynamics model based on Peters finite-state unsteady thin-airfoil theory. A strip theory approach is utilised to couple the 2D aerodynamics approach to the 3D structural model of the Pazy wing. The limitation of the strip theory model pertaining to the overprediction of loads for finite wings is circumvented through the application of a tip loss correction. The corrected model exhibits a maximum error of 0.42% compared to the results obtained from the medium-fidelity UVLM approach. Flutter analysis of the deformed wing is conducted by considering the nonlinear static aeroelastic equilibrium condition for a given angle of attack and air speed as the reference state. The present model predicts a 6.3% lower flutter speed than the prediction from reference experimental studies. Time domain simulations are conducted within the instability margins with the utilisation of the reduced-order aeroelastic model. The K-N method is applied to obtain a structural ROM, which is then coupled to the unsteady aerodynamics model. The time domain simulations show that limit cycle

oscillations occur due to the presence of nonlinearities within the system. Neglecting the structural nonlinearities results in exponential growth in amplitudes, indicating a hard flutter mechanism. The variation in peak LCO amplitudes observed at different air speeds, along with the lack of sensitivity to initial conditions, indicates a supercritical behaviour. In contrast, the experimental studies on the Pazy wing showed a distinct subcritical behaviour which was attributed to aerodynamic nonlinearities due to the considerably larger twist seen in the oscillations. The present model predicts transverse displacements of 1.3%, whereas the reference results are predicted to be in the range of 1-2%. The maximum wing twist during LCO is predicted to be 2.2^0 using the present model, while the reference twist ranges up to 10 degrees. Nevertheless, the model is able to capture the expected LCO response following the onset of flutter. The utilisation of the K-N method has a significant impact on the computational time required for time domain LCO simulations. The numerical model, built on the chosen analysis parameters in the present work, requires up to 5 minutes for time domain simulations. Setting up the ROM is computationally demanding; however, for the presented test case, this is primarily due to the large number of FE nodes considered in the initial model.

6

CONCLUSIONS AND RECOMMENDATIONS

6.1. CONCLUSIONS

The inclusion of geometric nonlinearities in aeroelastic analyses of highly flexible wings is necessary to predict the related nonlinear aeroelastic effects, which are otherwise overlooked when using linear methods. The transition from the well-established linear methods, however, is not a straightforward task due to the accompanying complexities in solving nonlinear aeroelastic systems and the additional computational burden. Notwithstanding the current progress in nonlinear aeroelasticity, the possibility of the existence of unknown nonlinear aeroelastic effects cannot be disregarded. Thus, continued experimental investigations and developments in numerical modelling are necessary to establish further confidence in this field. The primary objective of this dissertation, as stated in Chapter 1, was to develop a reduced-order

nonlinear aeroelastic model suitable for investigating nonlinear aeroelastic effects in subsonic flow and thereby add to the growing understanding of this field. The research conducted to achieve the objectives can be broadly divided into two parts: (1) investigations pertaining to the static and dynamic structural reduced-order models, and (2) coupling of the structural reduced-order model to an aerodynamic model and investigations of the corresponding nonlinear aeroelastic effects. The conclusions drawn from this work are summarised in Sections 6.1.1 and 6.1.2.

6.1.1. Geometrically nonlinear structural model

The dissertation focused on the utilisation of the Koiter-Newton method for modelling the geometrically nonlinear effects. The choice of this method was made due to the following reasons: (1) its effectiveness in modelling nonlinear effects under various boundary conditions has been previously demonstrated through numerical and experimental validation, (2) compatibility of the method with finite element models, and (3) the method offers flexibility in the choice of bases for model reduction. At the beginning of the research, it was discovered that the K-N method shows a higher effectiveness for structures which have nonlinear effects predominantly due to bending-stretching coupling. The application to cantilever structures is, therefore, not directly impactful, as they exhibit a greater influence of nonlinearity due to large rotations, and the ROM does not inherently account for this. One of the objectives was to evaluate whether the ROM can be adapted for cantilevers. To this end, a ROM updating process was developed, which involves modifying the ROM parameters after fixed load increments to account for the changing geometry. The impact of the large rotations is correlated with the change in the reduction bases.

As a first step, the method was applied to nonlinear static analyses of various cantilevered structures constructed using beam and shell elements. The type of the load application was varied in the test cases (concentrated tip loads, distributed loads, follower and non-follower forces) for extensive verification of the method. The magnitudes of the applied loads were chosen to ensure that the deflections were sufficiently large to be within the geometrically nonlinear domain. It was initially observed that the ROM constructed for the undeformed geometry is only accurate for weakly nonlinear systems with a tip deflection of less than 20% of the span. In contrast, when the ROM is updated at fixed intervals by updating the geometry, it is possible to accurately obtain the nonlinear response with tip deflections up to 50% of the span. The drawback of having such an updating process, especially for FE models with a large number of FE nodes, is that the ROM computation time increases significantly. Thus, the utilisation of such an updating process progressively becomes counterproductive in terms of efficiency when the FE model is discretised into a finer mesh. The accuracy, however, was retained, with a maximum error of less than 5% observed in all the investigated verification cases.

In the next step, the updating process was expanded to study the large-amplitude dynamic behaviour of cantilevered structures. In this case, the momentum subspace variant of the K-N method was applied, which utilises an eigenmode-based reduction basis. The key idea here was to build a database of the ROM parameters based on the static analyses, which can be subsequently utilised for dynamic analyses. The approach circumvents the need to reconstruct the ROM as a function of time. The method was applied to various cantilevered structures. Time domain analyses of cantilever beams with application of the ROM updating approach appear to be significantly more beneficial in improving

the accuracy. Nonlinear frequency response curves were constructed for a cantilever sheet for verification against experimental results (Farokhi et al., 2022). It was observed that when the ROM is only constructed in the undeformed state, it is not possible to obtain any frequency-amplitude dependence. However, when the ROM is updated with increasing deflections, the expected hardening effect was captured. Therefore, the ROM without an updating procedure is unsuitable for modelling large amplitude dynamics of cantilevers. The adaptations made by updating the ROM over fixed displacement increments enable the model to capture the expected nonlinear dynamic effects.

The K-N method was next applied to the Pazy wing, which was chosen as the benchmark case for the subsequent analyses. A full order model was constructed in MSC NASTRAN comprising 130,272 DOFs. The purpose of constructing an FE model with a finer mesh, compared to the other test cases shown in Chapters 2 and 3, was to assess how the K-N method performs for larger structural models. Initial investigations into nonlinear static deformations revealed that the K-N method with ROM updates effectively captures the nonlinear static response up to tip deflections of 45% of the span. The nonlinear dynamic response to gust-like perturbations could also be captured well. In this case, ROM updates were not utilised, but the model could still accurately capture the dynamic response up to tip deflections of 28% of the span, with an error of less than 1%. Interestingly, only 3 eigenmodes were sufficient to reproduce the results comparable to the FE solution. This effectively reduced the FE model to a 3-DOF system, a reduction of five orders of magnitude from the full-order model.

Two factors that have an influence on the computational efficiency of the proposed ROM updating method are: (1) number of updates required, and (2) the number of DOFs in the FE model. It is evident from

the verification cases that the number of ROM updates required to maintain accuracy increases as the deflections increase. On the other hand, the effort required to compute the ROM parameters increases for models with larger number of DOFs. Based on the presented studies in Chapters 2 and 4, in the static case, the utilisation of the ROM with the updating procedure is computationally more efficient for moderately large deflections (< 30% tip deflection) and when the number of DOFs in the FE model is in the order of 10^3. It is better suited for cases where repeated analyses are to be performed since the ROM parameters can be stored and reused for subsequent analyses. However, in time domain analyses, the approach showed a greater potential. The nonlinear time domain analysis performed on the Pazy wing in Chapter 4 showed that for moderately large deflections, a reduction in 87% of the simulation time, including the ROM computation time, could be achieved in comparison to the FE solver despite the large number of DOFs in the initial FE model. In general, the results obtained from the structural analyses conducted using the K-N method can be regarded as a baseline for application to cantilever structures undergoing wing-like motion.

6.1.2. Coupling of the structural ROM to the aerodynamics model

With sufficient verification of the K-N method and the constructed FE model of the Pazy wing, the next objective was to construct the reduced-order nonlinear aeroelastic model. The aerodynamics model based on Peters theory was utilised in the nonlinear aeroelastic model. A node-to-node coupling approach was employed to transfer information between the structural and aerodynamic models. The proposed numerical model was validated against reference numerical (Riso and Cesnik, 2022) and experimental studies (Drachinsky et al., 2022)

conducted on the Pazy wing. The following main conclusions can be derived from the obtained results:

(1) The presented model was able to capture the nonlinear static aeroelastic response using a tip loss correction, comparable to frameworks which utilise a full-order FE model and higher fidelity UVLM aerodynamics. However, since the nonlinearity necessitates an iterative process, each iteration requires a ROM reconstruction. This exacerbates the computational time significantly and consequently the process is not beneficial in gaining computational efficiency. The limitation, however, is related to the size of the initial FE model. The ROM construction is more efficient for FE models comprising a smaller number of FE nodes.

(2) The nonlinear flutter speed predicted using the present model is 6.3% lower than the reference experimental results. The underestimation of the flutter speed is attributed to the comparatively lower stiffness in the FE model utilised in the present work. Since flutter speeds are related to the correct estimation of the nonlinear static aeroelastic displacements, the results further affirm the validity of the coupled model.

(3) The framework is able to predict the LCO response following the flutter onset. This is in accordance with the observed behaviour in prior experimental work. Since a linear aerodynamics model is utilised, it can be concluded that the LCO response obtained for the Pazy wing model is purely a consequence of geometric nonlinearity. This is affirmed by the fact that on linearising the structural model, the LCO response changes to a hard flutter. The transverse displacements observed during the LCO are < 1.3% which is somewhat similar to the observations in the experiments. The bifurcation observed in the numerical model appears to be supercritical in nature, characterised by a gradual increase in LCO amplitudes immediately after flutter onset, as well as a lack of sensitivity

to initial conditions. This contradicts the experimental results, which capture a strong hysteretic effect during airspeed sweep, indicating a subcritical bifurcation. However, the subcritical nature observed in the experiments is attributed to dynamic stall effects since the observed wing tip twists are over 10^0. In comparison, the maximum twist response captured in the present model is $\pm 2.2^o$, which is comparatively much lower than the experimental observations and does not exceed the stall limits. Considering the computational effort, the LCO simulations were found to be efficient, with up to 5 minutes required to compute the time domain solutions with 20,000-time steps.

6.2. RECOMMENDATIONS

The studies conducted using the presented framework provide valuable insights into the method's capabilities. Some recommendations for future work are as follows:

- The ROM construction process utilised in the present work is limited by the choice of finite element formulations. Practically, it is more beneficial to combine the ROM construction process with a more comprehensive FE toolbox. This would allow the importability of more element types and, by extension, all compatible FE models without restrictions. The structural solver B2000++, acquired by DLR in 2019, is a potential candidate for pursuing this.

- The nonlinear frequency-amplitude dependency, in this work, is predicted by performing a frequency sweep and conducting a sequence of time domain simulations. It is more efficient to utilise continuation methods. The minor complexity lies in incorporating the ROM updating process into the continuation algorithm. However, this can be achieved by adapting the algorithm to check for displacement

limits and modifying the ROM parameters accordingly. On a related note, predicting bifurcation characteristics in the flutter domain can benefit from the use of continuation methods. In this case, the variations in aerodynamic contributions in the aeroelastic model must be considered.

- The aerodynamic model utilised in this work, although suitable for the chosen investigations, is erroneous in conditions where the deflections exceed the stall limits. As previously discussed, incorporating an appropriate stall model is beneficial for the extended application of the framework.

- The ROM is sensitive to the choice of reduction bases. In the presented studies, the structural ROM is constructed using structural eigenmodes. Another possible choice is the utilisation of the complex aeroelastic modes since these already contain information about the aeroelastic system. Initial studies conducted with ROMs formulated using aeroelastic modes have shown that the LCO response can be captured using such ROMs; however, the deflection behaviour upon airspeed variation was found to be erratic. Whether this is a numerical artefact or a physical error in the model is currently unclear. Nevertheless, in future work, it would be worthwhile to investigate alternative reduction bases for the ROM construction.

Acknowledgements

As I begin to write this section, I am reflecting on the first few weeks when I started my research, already keen to produce results, but still navigating unfamiliar territory. My promotors gently reminded me that the Ph.D. research is a 4-year program and best approached as a long-distance run. I have tried to adhere to their advice throughout this lengthy yet enriching journey, especially on the days when obtaining a solution to the problem statement was seemingly impossible. In retrospect, there are several people whose support has been instrumental in shaping this dissertation, and I am truly grateful to each one of them.

First of all, I would like to thank my promotors Dr. Farbod Alijani and Dr. Roeland De Breuker for their invaluable guidance on my research. I remember the initial phase of our discussions when the research idea was still *semi*-conceptualized. The encouragement I received from them assured me of my decision to pursue the research topic. Even though I could only visit Delft once during my research, the online discussions we had at regular intervals were immensely helpful in ensuring that I remained on track to achieve the research objectives.

I would like to express my sincere gratitude to the late Dr. Mostafa Abdalla who introduced me to the world of reduced-order modelling, nonlinear dynamics and the Koiter-Newton method while I was a Master student at TU Delft back in 2016. Even though I worked only for a short duration with him, his brilliance has left a lasting impression upon me, as I am sure on his other former students and colleagues.

The work was carried out at the premises of DLR, Institute of Aeroelasticity, Germany. I am grateful to Dr. Wolf R. Krüger for the

opportunity to pursue the Ph.D. research while being employed at DLR and for his feedback during the research. I would like to thank Dr. Thomas Klimmek and Matthias Schulze for the helpful discussions related to our department project work. Their support made it a lot easier to balance my Ph.D. research along with other DLR activities. I also greatly appreciate the inputs provided by Dr. Markus Ritter, whose Ph.D. dissertation partly inspired my work. Thanks to Jonathan Hilger for his support in the installation and use of the UVLM code. Thanks also to Hendrik Verdonck for reviewing and correcting the Dutch translation of the dissertation summary. I am grateful to Dr. Vega Handojo for his support in navigating the initial settling down process in Göttingen. He was also for a short time my guitar teacher. Fortunately for me, my dissertation writing skills turned out to be better than my guitar skills. On that note, I would again like to thank Dr. Farbod Alijani, Dr. Roeland De Breuker, Dr. Wolf R. Krüger and all the members of my Ph.D. defence committee for their feedback on the dissertation which has surely improved its readability.

To some of the most important people in my life, mom and dad, you have shaped who I am. The scientific curiosity and resilience that I have required to conduct research was first and foremost nurtured by you. I am forever grateful for your encouragement and support while I pursue a career four thousand miles away from home. To my sisters, Surabhi and Neha, who would have thought that amongst the three of us I would be the one writing a Ph.D. dissertation? You have always been beacons of academic excellence and inspirations for me. To my wife, Priyanka, the completion of this dissertation is undoubtedly a shared success between the two of us. I am truly grateful for your love and support, especially in the last couple of years as we began the wonderful journey of raising our little sunshine together.

Bibliography

Afonso, F., Vale, J., Oliveira, É., Lau, F., & Suleman, A. (2017). A review on non-linear aeroelasticity of high aspect-ratio wings. *Progress in Aerospace Sciences*, *89*, 40-57.

Albano, E., & Rodden, W. P. (1969). A doublet-lattice method for calculating lift distributions on oscillating surfaces in subsonic flows. *AIAA journal*, *7*(2), 279-285.

Alijani, F., & Amabili, M. (2014). Non-linear vibrations of shells: A literature review from 2003 to 2013. *International journal of non-linear mechanics*, *58*, 233-257.

Alvin, K., de la Fuente, H., Haugen, B., and Felippa, C. (1992). Membrane triangles with corner drilling freedoms—I. The EFF element, *Finite Elements in Analysis and Design*, Vol. 12, No. 3-4, pp. 163-187

Amabili, M. (2008). *Nonlinear vibrations and stability of shells and plates*. Cambridge University Press.

Arena, A., Lacarbonara, W., & Marzocca, P. (2013). Nonlinear aeroelastic formulation and post flutter analysis of flexible high-aspect-ratio wings. *Journal of aircraft*, *50*(6), 1748-1764.

Argyris, J. H., Dunne, P. C., & Scharpf, D. W. (1978). On large displacement-small strain analysis of structures with rotational degrees of freedom. *Computer Methods in Applied Mechanics and Engineering*, *14*(3), 401-451.

Avin, O., Raveh, D. E., Drachinsky, A., Ben-Shmuel, Y., & Tur, M. (2022). Experimental aeroelastic benchmark of a very flexible wing. *AIAA Journal*, *60*(3), 1745-1768.

Battini, J. M., & Pacoste, C. (2002). Co-rotational beam elements with warping effects in instability problems. *Computer Methods in Applied Mechanics and Engineering*, 191(17-18), 1755-1789.

Belardinelli, P., Ghatkesar, M. K., Staufer, U., & Alijani, F. (2017). Linear and non-linear vibrations of fluid-filled hollow microcantilevers interacting with small particles. *International Journal of Non-Linear Mechanics*, *93*, 30-40.

Benini, G. R., Belo, E. M., & Marques, F. D. (2004). Numerical model for the simulation of fixed wings aeroelastic response. *Journal of the Brazilian Society of Mechanical Sciences and Engineering*, *26*, 129-136.

Bisplinghoff, R. L., Ashley, H., & Halfman, R. L. (2013). *Aeroelasticity*. Courier Corporation.

Bisshopp, K. E., & Drucker, D. C. (1945). Large deflection of cantilever beams. *Quarterly of applied mathematics*, 3(3), 272-275.

Cesnik, C., Hodges, D. H., & Patil, M.J. (1996). Aeroelastic analysis of composite wings. In *37th structure, structural dynamics and materials conference* (p. 1444).

Cesnik, C.E, & Su, W. (2005). Nonlinear aeroelastic modelling and analysis of fully flexible aircraft. In *46th AIAA/ASME/ASCE/AHS/ASC Structures, Structural Dynamics and Materials Conference* (p. 2169).

Cesnik, C. E., Senatore, P. J., Su, W., Atkins, E. M., & Shearer, C. M. (2012). X-HALE: A very flexible unmanned aerial vehicle for nonlinear aeroelastic tests. *AIAA journal*, 50(12), 2820-2833.

Collar, A. R. (1946). The expanding domain of aeroelasticity. *The Aeronautical Journal*, *50*(428), 613-636.

Conner, M. D., Tang, D. M., Dowell, E. H., & Virgin, L. N. (1997). Nonlinear behavior of a typical airfoil section with control surface freeplay: a numerical and experimental study. *Journal of Fluids and structures*, *11*(1), 89-109.

Crespo da Silva, M. R. M., & Glynn, C. C. (1978a). Nonlinear flexural-flexural-torsional dynamics of inextensional beams. I. Equations of motion. *Journal of Structural Mechanics*, *6*(4), 437-448.

Crespo da Silva, M. R. M., & Glynn, C. C. (1978b). Nonlinear flexural-flexural-torsional dynamics of inextensional beams. II. Forced motions. *Journal of Structural Mechanics*, *6*(4), 449-461.

Crisfield, M. A., Remmers, J. J., & Verhoosel, C. V. (1997). *Non-linear finite element analysis of solids and structures* (Vol. 569). New York: Wiley.

Crisfield, M. A., & Jelenić, G. (1999). Objectivity of strain measures in the geometrically exact three-dimensional beam theory and its finite-element implementation. *Proceedings of the Royal Society of London. Series A: Mathematical, Physical and Engineering Sciences*, 455(1983), 1125-1147.

Demasi, L., & Palacios, A. (2010). A reduced order nonlinear aeroelastic analysis of joined wings based on the proper orthogonal decomposition. In *51st AIAA/ASME/ASCE/AHS/ASC Structures, Structural Dynamics, and Materials Conference 18th AIAA/ASME/AHS Adaptive Structures Conference 12th* (p. 2722).

Dillinger, J. (2014). *Static aeroelastic optimization of composite wings with variable stiffness laminates*. Doctoral dissertation, Delft University of Technology.

Dowell, E. H. (1972). *Panel flutter* (No. NASA-SP-8004).

Drachinsky, A., & Raveh, D. E. (2020). Modal rotations: A modal-based method for large structural deformations of slender bodies. *AIAA Journal*, 58(7), 3159-3173.

Drachinsky, A., & Raveh, D. E. (2022). Nonlinear aeroelastic analysis of highly flexible wings using the modal rotation method. *AIAA Journal*, *60*(5), 3122-3134.

Drachinsky, A., Avin, O., Raveh, D. E., Ben-Shmuel, Y., & Tur, M. (2022). Flutter tests of the Pazy wing. *AIAA Journal*, *60*(9), 5414-5421.

Erickson, L. L. (1990). *Panel methods: An introduction.* NASA Technical Paper (No. A-89266).

Farokhi, H., Xia, Y., & Erturk, A. (2022). Experimentally validated geometrically exact model for extreme nonlinear motions of cantilevers. *Nonlinear dynamics*, *107*(1), 457-475.

Felippa, C. A. (2000). *A systematic approach to the element-independent corotational dynamics of finite elements* (Technical Report CU-CAS-00-03). Center for Aerospace Structures, University of Colorado Boulder.

Fernandez-Escudero, C., Gagnon, M., Laurendeau, E., Prothin, S., Michon, G., & Ross, A. (2019). Comparison of low, medium and high-fidelity numerical methods for unsteady aerodynamics and nonlinear aeroelasticity. *Journal of Fluids and Structures*, *91*, 102744.

Garcea, G., Madeo, A., & Casciaro, R. (2012). The implicit corotational method and its use in the derivation of nonlinear structural models for beams and plates. *Journal of Mechanics of Materials and Structures*, 7(6), 509-538.

Goizueta, N., Wynn, A., Palacios, R., Drachinsky, A., & Raveh, D. E. (2022). Flutter predictions for very flexible wing wind tunnel test. *Journal of Aircraft,* 59(4), 1082-1097.

Gonzalez, P., Barbosa, G., Quesada, Á., Stavorinus, G., Silvestre, F. J., Hilger, J., & Krüger, W. R. (2024). Wind tunnel testing and modal validation of TU-Flex's high aspect-ratio wings. *International Forum on Aeroelasticity and Structural Dynamics IFASD*, Den Haag, Netherlands.

Hilger, J., & Ritter, M. (2021). Nonlinear aeroelastic simulations and stability analysis of the pazy wing aeroelastic benchmark. *Aerospace*, *8*(10), 308.

Hodges, D. H. (1990). A mixed variational formulation based on exact intrinsic equations for dynamics of moving beams. *International journal of solids and structures*, 26(11), 1253-1273.

Hodges, D. H., & Pierce, G. A. (2011). *Introduction to structural dynamics and aeroelasticity* (Vol. 15). Cambridge university press.

Howcroft, C., Calderon, D., Lambert, L., Castellani, M., Cooper, J. E., Lowenberg, M. H., & Neild, S. (2016). Aeroelastic modelling of highly flexible wings. In *15th Dynamics specialists conference* (p. 1798).

Howcroft, C., Cook, R. G., Neild, S. A., Lowenberg, M. H., Cooper, J. E., & Coetzee, E. B. (2018). On the geometrically exact low-order modelling of a flexible beam: formulation and numerical tests. *Proceedings of the Royal Society A: Mathematical, Physical and Engineering Sciences*, *474*(2216).

Idelsohn, S. R., & Cardona, A. (1985). A reduction method for nonlinear structural dynamic analysis. *Computer Methods in Applied Mechanics and Engineering*, 49(3), 253-279.

Jain, S., Tiso, P., Rutzmoser, J. B., & Rixen, D. J. (2017). A quadratic manifold for model order reduction of nonlinear structural dynamics. *Computers & Structures*, 188, 80-94.

Jain, S., & Haller, G. (2022). How to compute invariant manifolds and their reduced dynamics in high-dimensional finite element models. *Nonlinear dynamics*, *107*(2), 1417-1450.

Jian, Z., & Jinwu, X. (2009). Nonlinear aeroelastic response of high-aspect-ratio flexible wings. *Chinese Journal of Aeronautics*, *22*(4), 355-363.

Katz, J., & Plotkin, A. (2001). *Low-speed aerodynamics* (Vol. 13). Cambridge university press.

Kerschen, G., Peeters, M., Golinval, J. C., & Vakakis, A. F. (2009). Nonlinear normal modes, Part I: A useful framework for the structural dynamicist. *Mechanical systems and signal processing*, *23*(1), 170-194.

Koiter, W. T. (1945). On the stability of elastic equilibrium. Doctoral dissertation, *Delft University of Technology*.

Kroo, I. (2001). Drag due to lift: concepts for prediction and reduction. *Annual review of fluid mechanics*, 33(1), 587-617.

Leishman, J. G., & Beddoes, T. S. (1989). A Semi-Empirical model for dynamic stall. *Journal of the American Helicopter society*, *34*(3), 3-17.

Liang, K. (2013). *A Koiter-Newton arclength method for buckling-sensitive structures.* Doctoral dissertation, Delft University of Technology (Netherlands).

Liang, K., Ruess, M., & Abdalla, M.M. (2016). Co-rotational finite element formulation used in the Koiter–Newton method for nonlinear buckling analyses. *Finite Elements in Analysis and Design*, 116, 38-54.

Mahmoodi, S. N., & Jalili, N. (2007). Non-linear vibrations and frequency response analysis of piezoelectrically driven microcantilevers. *International Journal of Non-Linear Mechanics*, *42*(4), 577-587.

Mallett, R. H., & Marcal, P. V. (1968). Finite element analysis of nonlinear structures. *Journal of the structural division, 94*(9), 2081-2106.

Marsh, G. (2010). Airbus A350 XWB update. *Reinforced plastics*, *54*(6), 20-24.

McEwan, M. I., Wright, J. R., Cooper, J. E., & Leung, A. Y. T. (2001). A combined modal/finite element analysis technique for the dynamic response of a non-linear beam to harmonic excitation. *Journal of Sound and Vibration*, *243*(4), 601-624.

Mignolet, M. P., Przekop, A., Rizzi, S. A., & Spottswood, S. M. (2013). A review of indirect/non-intrusive reduced order modeling of nonlinear geometric structures. *Journal of Sound and Vibration*, *332*(10), 2437-2460.

Militello, C., & Felippa, C. A. (1991). The first ANDES elements: 9-dof plate bending triangles. *Computer methods in applied mechanics and engineering*, *93*(2), 217-246.

Moita, G. F., & Crisfield, M. A. (1996). A finite element formulation for 3-D continua using the co-rotational technique. *International Journal for Numerical Methods in Engineering*, 39(22), 3775-3792.

Morsch, F. M., Tolou, N., & Herder, J. L. (2009). Comparison of methods for large deflection analysis of a cantilever beam under free end point load cases. In *International Design Engineering Technical Conferences and Computers and Information in Engineering Conference* (Vol. 49040, pp. 183-191).

Muravyov, A. A., & Rizzi, S. A. (2003). Determination of nonlinear stiffness with application to random vibration of geometrically nonlinear structures. Computers & Structures, 81(15), 1513-1523.

Murua, J. (2012). *Flexible aircraft dynamics with a geometrically-nonlinear description of the unsteady aerodynamics* (Doctoral dissertation, Department of Aeronautics, Imperial College London).

Murua, J., Palacios, R., & Graham, J. M. R. (2012). Applications of the unsteady vortex-lattice method in aircraft aeroelasticity and flight dynamics. *Progress in Aerospace Sciences*, *55*, 46-72.

NASTRAN, MSC (2014). Aeroelastic analysis user's guide. *MSC Software Corporation: Newport Beach, CA, USA*.

NASTRAN, MSC (2018). Nonlinear user's guide. *MSC Software Corporation: Newport Beach, CA, USA*.

Noll, T. E., Brown, J. M., Perez-Davis, M. E., Ishmael, S. D., Tiffany, G. C., & Gaier, M. (2004). Investigation of the Helios prototype aircraft mishap volume I mishap report. *Downloaded on 9th March,2025*.

Oden, J. T. (1967). Numerical formulation of nonlinear elasticity problems. *Journal of the Structural Division*, 93(3), 235-255.

Oran, C., & Kassimali, A. (1976). Large deformations of framed structures under static and dynamic loads. *Computers & structures*, 6(6), 539-547.

Padmanabhan, M. A., & Dowell, E. H. (2017). Calculation of aeroelastic limit cycles due to localized nonlinearity and static preload. *AIAA Journal*, *55*(8), 2762-2772.

Palacios, R., & Cesnik, C.E. (2005). Static nonlinear aeroelasticity of flexible slender wings in compressible flow. In *46th AIAA/ASME/ASCE/AHS/ASC Structures, Structural Dynamics and Materials Conference* (p. 1945).

Palacios, R., Murua, J., & Cook, R. (2010). Structural and aerodynamic models in nonlinear flight dynamics of very flexible aircraft. *AIAA journal*, *48*(11), 2648-2659.

Pancini dos Santos, L. G., Cesnik, C. E., & Marques, F. D. (2024). Effects of Separated-Flow Nonlinearities on the Flutter Behaviour of the Pazy Wing. In *AIAA SCITECH 2024 Forum* (p. 0829).

Pany, C., & Rao, G. V. (2002). Calculation of non-linear fundamental frequency of a cantilever beam using non-linear stiffness. *Journal of sound and vibration*, *256*(4), 787-790.

Patil, M. J., Hodges, D. H., & Cesnik, C. E. (1998). Nonlinear aeroelastic analysis of aircraft with high-aspect-ratio wings. In *39th AIAA/ASME/ASCE/AHS/ASC Structures, Structural Dynamics, and Materials Conference and Exhibit* (p. 1955).

Patil, M. J., Hodges, D. H., & Cesnik, C. E. (1999). Characterizing the effects of geometrical nonlinearities on aeroelastic behaviour of high-aspect ratio wings. In *NASA Conference Publication* (pp. 501-510). NASA.

Patil, M. J., Hodges, D. H., & Cesnik, C. E. (2000). Nonlinear aeroelastic analysis of complete aircraft in subsonic flow. *Journal of Aircraft*, *37*(5), 753-760.

Patil, M. J., Hodges, D. H., & Cesnik, C. E. (2001). Limit-cycle oscillations in high-aspect-ratio wings. *Journal of fluids and structures*, *15*(1), 107-132.

Patil, M. J., & Hodges, D. H. (2004). On the importance of aerodynamic and structural geometrical nonlinearities in aeroelastic behaviour of high-aspect-ratio wings. *Journal of Fluids and Structures*, 19(7), 905-915.

Peters, D. A., Barwey, D., & Su, A. (1994). An integrated airloads-inflow model for use in rotor aeroelasticity and control analysis. *Mathematical and computer modelling*, *19*(3-4), 109-123.

Peters, D. A., Karunamoorthy, S., & Cao, W. M. (1995). Finite state induced flow models. I-Two-dimensional thin airfoil. *Journal of aircraft*, *32*(2), 313-322.

Rankin, C. C., & Brogan, F. A. (1986). An element independent corotational procedure for the treatment of large rotations. *Journal of Pressure Vessel Technology, Vol.* 108, 165-174.

Riso, C., & Cesnik, C. E. (2021). Correlations between UM/NAST nonlinear aeroelastic simulations and the pre-Pazy wing experiment. In *AIAA Scitech 2021 Forum* (p. 1712).

Riso, C., & Cesnik, C. E. (2022). Post-flutter dynamics of the Pazy wing geometrically nonlinear benchmark model. In *International Forum on Aeroelasticity and Structural Dynamics* (pp. 1-18).

Riso, C., & Cesnik, C. E. (2023). Geometrically nonlinear effects in wing aeroelastic dynamics at large deflections. *Journal of Fluids and Structures*, *120*, 103897.

Ritter, M. R. (2019). *An extended modal approach for nonlinear aeroelastic simulations of highly flexible aircraft structures*. Doctoral dissertation, Technische Universitaet Berlin (Germany).

Ritter, M., Cesnik, C. E., & Krüger, W. R. (2015). An enhanced modal approach for large deformation modeling of wing-like structures. In *56th AIAA/ASCE/AHS/ASC Structures, Structural Dynamics, and Materials Conference* (p. 0176).

Ritter, M., Hilger, J., Ribeiro, A., Öngüt, A. E., Righi, M., Raveh, D. E., & Bussamra, F. L. (2024). Collaborative Pazy wing analyses for the third aeroelastic prediction workshop. In *AIAA SciTech 2024 Forum* (p. 0419).

Rosenberg, R. M. (1962). The Normal Modes of Nonlinear n-Degree-of-Freedom Systems. *Journal of Applied Mechanics*, *29*(1), 7.

Shang-Rou, H., Shaw, S. W., & Pierre, C. (1994). Normal modes for large amplitude vibration of a cantilever beam. *International Journal of Solids and Structures*, *31*(14), 1981-2014.

Shaw, S., & Pierre, C. (1991). Non-linear normal modes and invariant manifolds. *Journal of sound and Vibration*, *150*(1), 170-173.

Simo, J. C., & Vu-Quoc, L. (1991). A geometrically-exact rod model incorporating shear and torsion-warping deformation. *International Journal of Solids and Structures*, *27*(3), 371-393.

Sinha, K., Singh, N. K., Abdalla, M. M., De Breuker, R., & Alijani, F. (2020). A momentum subspace method for the model-order reduction in nonlinear structural dynamics: Theory and experiments. *International Journal of Non-Linear Mechanics*, *119*, 103314.

Sodja, J., Werter, N. P., & De Breuker, R. (2021). Aeroelastic demonstrator wing design for maneuver load alleviation under cruise shape constraint. *Journal of Aircraft*, *58*(3), 448-466.

Stanford, B. K., Jacobson, K. E., & Chwalowski, P. (2024). Aeroelastic Analysis of Highly Flexible Wings with Linearized Frequency-Domain Aerodynamics. *Journal of Aircraft*, *61*(2), 365-374.

Su, W., & Cesnik, C. E. (2011). Dynamic response of highly flexible flying wings. *AIAA journal*, *49*(2), 324-339.

Sze, K. Y., Liu, X. H., & Lo, S. H. (2004). Popular benchmark problems for geometric nonlinear analysis of shells. *Finite elements in analysis and design*, *40*(11), 1551-1569.

Tang, D., & Dowell, E. H. (2001). Experimental and theoretical study on aeroelastic response of high-aspect-ratio wings. *AIAA journal*, *39*(8), 1430-1441.

Theodorsen, T. (1935). *General theory of aerodynamic instability and the mechanism of flutter* (No. NACA-TR-496).

Touzé, C., Vizzaccaro, A., & Thomas, O. (2021). Model order reduction methods for geometrically nonlinear structures: a review of nonlinear techniques. *Nonlinear Dynamics*, *105*(2), 1141-1190.

Tran, C. T., & Petot, D. (1980). Semi-empirical model for the dynamic stall of airfoils in view of the application to the calculation of responses of a helicopter blade in forward flight.

Turner, M. J., Dill, E. H., Martin, H. C., & Melosh, R. J. (1960). Large deflections of structures subjected to heating and external loads. *Journal of the Aerospace Sciences*, 27(2), 97-106.

Vio, G. A., Dimitriadis, G., & Cooper, J. E. (2007). Bifurcation analysis and limit cycle oscillation amplitude prediction methods applied to the aeroelastic galloping problem. *Journal of Fluids and Structures*, *23*(7), 983-1011.

Vu-Quoc, L., & Deng, H. (1995). Galerkin projection for geometrically exact sandwich beams allowing for ply drop-off. *Journal of applied mechanics*, *62*(2), 479-488.

Wang, X. Q., Perez, R. A., & Mignolet, M. P. (2013). Nonlinear reduced order modeling of complex wing models. In *54th AIAA/ASME/ASCE/AHS/ASC Structures, Structural Dynamics, and Materials Conference* (p. 1520).

Wempner, G. (1969). Finite elements, finite rotations and small strains of flexible shells. *International Journal of Solids and Structures*, 5(2), 117-153.

Wright, J. R., & Cooper, J. E. (2008). *Introduction to aircraft aeroelasticity and loads* (Vol. 18). John Wiley & Sons.

Xiang, J., Yan, Y., & Li, D. (2014). Recent advance in nonlinear aeroelastic analysis and control of the aircraft. *Chinese journal of aeronautics*, *27*(1), 12-22.

Xie, C., Liu, Y., Yang, C., & Cooper, J. E. (2016). Geometrically nonlinear aeroelastic stability analysis and wind tunnel test validation of a very flexible wing. *Shock and Vibration,* 2016(1), 5090719.

Yoo, W. S., Lee, J. H., Park, S. J., Sohn, J. H., Dmitrochenko, O., & Pogorelov, D. (2003). Large oscillations of a thin cantilever beam: physical experiments and simulation using the absolute nodal coordinate formulation. *Nonlinear Dynamics*, *34*(1), 3-29.

Appendix

I. FE formulation utilised in the structural models

This Section presents the FE formulations utilized in this work. There are two types of elements implemented: (1) a planar beam element with 3-DOF per node and (2) a high-performance triangular shell element with 6-DOF per node (Militello and Felippa, 1991; Alvin et al., 1992). Detailed discussions on the computation of higher-order stiffness tensors has been previously presented by Liang (2013).

A. Beam element

Strain and curvature of a planar beam element in the finite element framework are defined in this section.

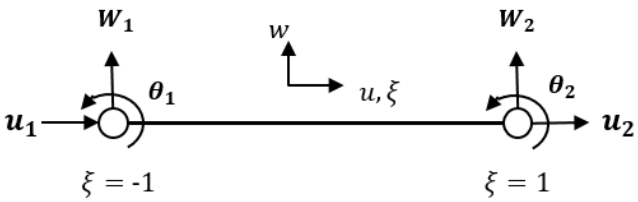

Fig A.1: Element degrees of freedom in the beam element

The strain ε and the curvature χ for this element is defined as:

$$\varepsilon = \frac{(u_2 - u_1)}{L} + \frac{1}{2}\left[\frac{(u_2 - u_1)^2}{L} + \frac{6}{5L^2}(w_1 - w_2)^2 + \frac{2}{15}(\theta_1 - \theta_2)^2 + \frac{1}{5}\theta_1\theta_2 + \frac{1}{5L}(\theta_1 + \theta_2)(w_1 - w_2)\right]$$

$$\chi = -\frac{1}{L^2}\left[3w_1 - 3w_2 - \frac{6w_1 x}{L} + \frac{6w_2 x}{L} + (2L - 3x)\theta_1 + (L - 3x)\theta_2\right]$$

The total strain energy of an element is then:

$$U_{elem} = \frac{1}{2}\,\mathrm{Al}_{elem}\,\varepsilon'\,E\,\varepsilon$$

The higher order derivatives of the strain energy then provide us with the following stiffness tensors required for the ROM computations:

$$L_{ij} = EAl_{elem}\left(\varepsilon\frac{\partial^2\varepsilon}{\partial q_i\,\partial q_j} + \frac{\partial\varepsilon}{\partial q_i}\,\frac{\partial\varepsilon}{\partial q_j}\right)$$

$$Q_{ijk} = \frac{EAl_{elem}}{2}\left(\frac{\partial\varepsilon}{\partial q_j}\,\frac{\partial^2\varepsilon}{\partial q_i\,\partial q_k} + \frac{\partial\varepsilon}{\partial q_i}\,\frac{\partial^2\varepsilon}{\partial q_j\,\partial q_k} + \frac{\partial\varepsilon}{\partial q_k}\,\frac{\partial^2\varepsilon}{\partial q_i\,\partial q_j}\right)$$

$$C_{ijkl} = \frac{EAl_{elem}}{6}\left(\frac{\partial^2\varepsilon}{\partial q_i\,\partial q_l}\,\frac{\partial^2\varepsilon}{\partial q_j\,\partial q_k} + \frac{\partial^2\varepsilon}{\partial q_j\,\partial q_l}\,\frac{\partial^2\varepsilon}{\partial q_i\,\partial q_k} + \frac{\partial^2\varepsilon}{\partial q_k\,\partial q_l}\,\frac{\partial^2\varepsilon}{\partial q_i\,\partial q_j}\right)$$

B. Shell Element

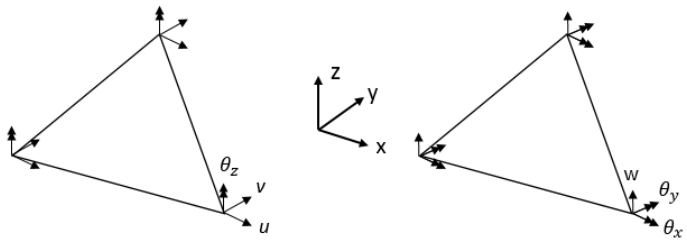

Fig B.1: Element degrees of freedom in the shell element

The nonlinear strain of the shell element is defined as:

$$\varepsilon = \varepsilon_l + \varepsilon_{nl} = (\boldsymbol{B_l} + \frac{1}{2}\boldsymbol{B_{nl}}(\boldsymbol{q}))\boldsymbol{q}$$

$$\boldsymbol{B_l} = \frac{1}{2A}[\boldsymbol{B_1}\,\boldsymbol{B_2}\,\boldsymbol{B_3}],$$

where A is the element area.

Considering that the three nodal coordinates are (x_1, y_1), (x_2, y_2) and (x_3, y_3):

$$x_{ij} = x_i - x_j$$

$$x_{ij} = x_i - x_j$$

$$\mathbf{B}_1 = \begin{bmatrix} y_{23} & 0 & 0 & 0 & 0 & \dfrac{y_{23}(y_{13} - y_{21})}{6} \\ 0 & x_{23} & 0 & 0 & 0 & \dfrac{x_{32}(x_{32} - x_{12})}{6} \\ x_{32} & y_{32} & 0 & 0 & 0 & \dfrac{x_{31}y_{13} - x_{12}y_{21}}{3} \end{bmatrix}$$

$$\mathbf{B}_2 = \begin{bmatrix} y_{31} & 0 & 0 & 0 & 0 & \dfrac{y_{31}(y_{21} - y_{32})}{6} \\ 0 & x_{13} & 0 & 0 & 0 & \dfrac{x_{13}(x_{12} - x_{23})}{6} \\ x_{13} & y_{31} & 0 & 0 & 0 & \dfrac{x_{12}y_{21} - x_{23}y_{32}}{3} \end{bmatrix}$$

$$\mathbf{B}_3 = \begin{bmatrix} y_{12} & 0 & 0 & 0 & 0 & \dfrac{y_{12}(y_{32} - y_{13})}{6} \\ 0 & x_{21} & 0 & 0 & 0 & \dfrac{x_{21}(x_{23} - x_{31})}{6} \\ x_{21} & y_{12} & 0 & 0 & 0 & \dfrac{x_{23}y_{32} - x_{31}y_{13}}{3} \end{bmatrix}$$

The nonlinear strain component can be computed using the $\mathbf{B_{nl}}(\mathbf{q})$ term which is given by:

$$\mathbf{B}_{\mathrm{nl}}(\mathbf{q}) = \begin{bmatrix} \boldsymbol{q}^t\, K_{xx} \\ \boldsymbol{q}^t\, K_{yy} \\ \boldsymbol{q}^t\, K_{xy} \end{bmatrix}$$

$$K_{xx} = \boldsymbol{B}_w^t \boldsymbol{T}_x^t \boldsymbol{T}_x \boldsymbol{B}_w + \boldsymbol{B}_v^t \boldsymbol{T}_x^t \boldsymbol{T}_x \boldsymbol{B}_v$$

$$K_{yy} = \boldsymbol{B}_w^t \boldsymbol{T}_y^t \boldsymbol{T}_y \boldsymbol{B}_w + \boldsymbol{B}_u^t \boldsymbol{T}_y^t \boldsymbol{T}_y \boldsymbol{B}_u$$

$$K_{xx} = \boldsymbol{B}_w^t (\boldsymbol{T}_x^t \boldsymbol{T}_y + \boldsymbol{T}_y^t \boldsymbol{T}_x) \boldsymbol{B}_w$$

Here,

$$\boldsymbol{T}_x = \frac{1}{2A}\,[\, y_{23}\; y_{31}\; y_{12}] \quad \text{and} \quad \boldsymbol{T}_y = \frac{1}{2A}\,[\, x_{32}\; y_{13}\; x_{21}]$$

The other symbols $\boldsymbol{B}_u$, $\boldsymbol{B}_v$, $\boldsymbol{B}_w$ represent 3 x 18 matrices. In $\boldsymbol{B}_u$ the terms at (1,1), (2,7), and (3,13) are 1 and all other terms are zero. In $\boldsymbol{B}_v$ the

terms at (1,2), (2,8), and (3,14) are 1 and all other terms are zero. Similarly, in $\boldsymbol{B}_w$ the terms at (1,3), (2,9), and (3,15) are 1 and all other terms are zero.

The in-plane strain energy is then described using the following equation:

$$U = \frac{1}{2} \mathrm{A}\mathcal{A}_m \left(\varepsilon_{l\alpha} + \varepsilon_{nl\alpha}\right)\left(\varepsilon_{l\beta} + \varepsilon_{nl\beta}\right), \qquad \alpha, \beta \rightarrow 1 \text{ to } 3$$

The stiffness tensors are then obtained as derivatives of the strain energy in a similar manner as described for the beam elements.

The internal force $\boldsymbol{f}$, tangent stiffness $\boldsymbol{L}$, quadratic stiffness $\boldsymbol{Q}$ and cubic stiffness $\boldsymbol{C}$ are derived as derivatives of the strain energy with respect to the displacement.

$$\boldsymbol{f} = A(\boldsymbol{B}_l{}'\boldsymbol{N}_{nl} + \boldsymbol{B}_{nl}{}'\boldsymbol{N})$$

$$\boldsymbol{L} = A\,(\boldsymbol{B}_l{}'\boldsymbol{A}_m\boldsymbol{B}_{nl} + \boldsymbol{B}_{nl}{}'\boldsymbol{A}_m\boldsymbol{B}_l + \boldsymbol{B}_{nl}{}'\boldsymbol{A}_m\boldsymbol{B}_{nl} + \boldsymbol{N}_x\boldsymbol{K}_{xx} + \boldsymbol{N}_y\boldsymbol{K}_{yy} + \boldsymbol{N}_{xy}\boldsymbol{K}_{xy})$$

$$\boldsymbol{N} = \boldsymbol{N}_l + \boldsymbol{N}_{nl} = \boldsymbol{A}_m\boldsymbol{B}_l\boldsymbol{q} + \frac{1}{2}\boldsymbol{A}_m\boldsymbol{B}_{nl}(\boldsymbol{q})\boldsymbol{q}$$

$$\boldsymbol{Q}(\boldsymbol{u}_\alpha, \boldsymbol{u}_\beta) = \frac{A}{2}\,(\boldsymbol{B}'_{nl}(\boldsymbol{u}_\beta)\boldsymbol{A}_m\boldsymbol{B}(\boldsymbol{u}_\alpha)\boldsymbol{u}_\alpha + \boldsymbol{B}'_{nl}(\boldsymbol{u}_\alpha)\boldsymbol{A}_m\boldsymbol{B}(\boldsymbol{u}_\beta)\boldsymbol{u}_\beta + \boldsymbol{B}'\boldsymbol{A}_m\boldsymbol{B}_{nl}(\boldsymbol{u}_\alpha)\boldsymbol{u}_\beta)$$

$$\boldsymbol{C}(\boldsymbol{u}_\alpha, \boldsymbol{u}_\beta, \boldsymbol{u}_\gamma, \boldsymbol{u}_\delta) = \frac{A}{6}\,(\boldsymbol{A}_m\boldsymbol{B}_{nl}(\boldsymbol{u}_\alpha)\boldsymbol{u}_\delta\boldsymbol{B}_{nl}(\boldsymbol{u}_\beta)\boldsymbol{u}_\gamma + \boldsymbol{A}_m\boldsymbol{B}_{nl}(\boldsymbol{u}_\beta)\boldsymbol{u}_\delta\boldsymbol{B}_{nl}(\boldsymbol{u}_\alpha)\boldsymbol{u}_\gamma + \boldsymbol{A}_m\boldsymbol{B}_{nl}(\boldsymbol{u}_\gamma)\boldsymbol{u}_\delta\boldsymbol{B}_{nl}(\boldsymbol{u}_\alpha)\boldsymbol{u}_\beta)$$

II. Equivalent beam properties of the Pazy wing

The equivalent beam model was obtained from the FEM2Stick tool (Riso and Cesnik, 2021), University of Michigan, and shared during the activities of the AePW3. The FE model consists of 16 node points located along the global x-axis, where the x-coordinates are defined as follows:

$\boldsymbol{x}$ = [0.0; 0.0382; 0.0764; 0.1147; 0.1529; 0.1912; 0.2294; 0.2677; 0.3059; 0.3442; 0.3824; 0.4207; 0.4589; 0.4972; 0.5307; 0.5498].

The area of cross-section variation across the elements is defined as follows:

$\boldsymbol{A}$= [9.794×10^{6}; 9.666×10^{6}; 9.647×10^{6}; 9.648×10^{6}; 9.649×10^{6}; 9.650×10^{6}; 9.650×10^{6}; 9.651×10^{6}; 9.6506×10^{6}; 9.649×10^{6}; 9.648×10^{6}; 9.647×10^{6}; 9.65×10^{6}; 9.69×10^{6}; 10.019×10^{6}].

Similarly, the beam inertia has variations in each element and is defined as follows:

$\boldsymbol{I}$ = [5.247; 4.504; 4.478; 4.474; 4.474; 4.474; 4.474; 4.474; 4.474; 4.474; 4.474; 4.476; 4.489; 4.548; 4.770].

An equivalent elastic modulus of 1.0 is utilised.

III. Verification of the aerodynamics model based on Peters theory

The implementation of the aerodynamic model is verified using a 2-D airfoil example presented by Hodges and Pierce (2011). The objective is to perform a stability analysis and predict the flutter speed of the 2-D airfoil. Considering Fig. 5.1, the following airfoil non-dimensional parameters are considered: a = -1/5, e = -1/10, μ = 20, r^2 = 6/25 and σ =

2/5. Here $\mu = m/\rho\pi b^2$, $r^2 = I_\theta/mb^2$, $\sigma = \omega_h/\omega_\theta$, where ω_h and ω_θ are the natural frequencies corresponding to the plunge *h* and pitch θ motions, respectively. The structural motion of such an airfoil is governed by:

$$m\ddot{h} + mbx_\theta\ddot{\theta} + k_h h = -L_0 \tag{A.3.1}$$

$$I_\theta\ddot{\theta} + mbx_\theta\ddot{h} + k_\theta\theta = M_0 \tag{A.3.2}$$

where L_0 is the lift per unit span and M_0 is the moment per unit span at the reference point, k_h is the spring constant corresponding to the plunge motion, k_θ is the spring constant corresponding to the pitch motion, *m* is the mass per unit span and I_θ is the moment of inertia about the reference point.

The aeroelastic system is obtained through the combination of Eq. 5.6 and Eqs A.3.1-A.3.2. Note that the negative sign in the lift in Eq. A.3.1 arises due to the sign convention used in the aerodynamics coordinate system where the plunge motion is positive in the downwards direction. Using the principal of virtual work, it can be shown that the negative sign appears with the generalized aerodynamic forces (Hodges and Pierce, 2011). The moments however, follow the same sign convention in both the structural and the aerodynamic coordinates i.e. nose up is considered as positive moment.

The stability analysis is conducted using the state-space model by transforming the system to a first order ordinary differential equation (ODE) of the form $\boldsymbol{A\dot{q}} = \boldsymbol{Bq}$, where $\boldsymbol{q} = \left[h\ \dot{h}\ \theta\ \dot{\theta}\ \boldsymbol{\lambda}\right]'$ and $\boldsymbol{\lambda}$ comprises the *N* aerodynamic states which are assumed to be 6 in accordance with the

reference analysis (Hodges and Pierce, 2011). In the matrix form, the combined structural equation of motion can be expressed as:

$$\begin{bmatrix} m & mbx_\theta \\ mbx_\theta & I_\theta \end{bmatrix}\begin{bmatrix} \ddot{h} \\ \ddot{\theta} \end{bmatrix} + \begin{bmatrix} k_h & 0 \\ 0 & k_\theta \end{bmatrix}\begin{bmatrix} h \\ \theta \end{bmatrix} = \begin{bmatrix} -L_0 \\ M_0 \end{bmatrix} \tag{A.3.3}$$

To transform the system to a first order ODE, an equation of the form $I\dot{x} - I\dot{x} = 0$ is added to Eq. A.3.3 where I is an identity matrix of size 2 x 2 and $x = [h\ \theta]'$. $\boldsymbol{A}$ and $\boldsymbol{B}$ are obtained by restructuring the matrices defined in the governing equations and defined as follows:

$$\boldsymbol{A} = \begin{bmatrix} \boldsymbol{A_1} & \boldsymbol{A_2} \\ \boldsymbol{A_3} & \boldsymbol{A_4} \end{bmatrix}, \qquad \boldsymbol{B} = \begin{bmatrix} \boldsymbol{B_1} & \boldsymbol{B_2} \\ \boldsymbol{B_3} & \boldsymbol{B_4} \end{bmatrix} \tag{A.3.4}$$

$$\boldsymbol{A_1} = \begin{bmatrix} 1 & 0 & 0 & 0 \\ 0 & m + \pi\rho b^2 & 0 & mbx_\theta - \pi\rho ab^3 \\ 0 & 0 & 1 & 0 \\ 0 & mbx_\theta - \pi\rho ab^3 & 0 & I_\theta + (0.125 + a^2)\pi\rho b^4 \end{bmatrix} \tag{A.3.5}$$

$$\boldsymbol{A_2} = null(4, N) \tag{A.3.6}$$

$\boldsymbol{A_3}$ is a matrix of size N × 4 where the columns are defined as follows:

$$\boldsymbol{A_3}(:,1) = null(N,1), \qquad \boldsymbol{A_3}(:,2) = -\bar{c}, \quad \boldsymbol{A_3}(:,3) = -U\bar{c}, \qquad \boldsymbol{A_3}(:,4) = -(0.5 - a)b\bar{c} \tag{A.3.7}$$

$$\boldsymbol{A_4} = \overline{\boldsymbol{A}} \tag{A.3.8}$$

$\bar{c}$ and $\overline{\boldsymbol{A}}$ are Peters constants as defined in Section 5.1.

$$\boldsymbol{B_1} = \tag{A.3.9}$$

$$\begin{bmatrix} 0 & 1 & 0 & 0 \\ -kh & -2\pi\rho Ub & -2\pi\rho U^2 b & -2\pi\rho b^2 U(1-a) \\ 0 & 0 & 0 & 1 \\ 0 & 2\pi\rho b^2 U(0.5+a) & 2\pi\rho b^2 U^2(0.5+a) - k_\theta & \pi\rho U b^3 a(1-2a) \end{bmatrix}$$

$\boldsymbol{B_2}$ is a matrix of size 4 × *N* where the rows are defined as follows:

$$\boldsymbol{B_2}(1,:) = \boldsymbol{B_2}(3,:) = null(1,N), \tag{A.3.10}$$
$$\boldsymbol{B_2}(2,:) = \pi\rho Ub\overline{\boldsymbol{b}}, \quad \boldsymbol{B_2}(4,:) = -\pi\rho Ub^2(0.5+a)\overline{\boldsymbol{b}}$$

$\boldsymbol{B_3}$ is a null matrix of size *N* × 4. $\boldsymbol{B_4}$ is a diagonal where all elements are -*U*/*b*.

Eigenvalue analysis is conducted on the matrix $\boldsymbol{A^{-1}B}$ which provides a set of complex eigenvalues as output. The real part of the complex eigenvalue Γ represents the decay rate and the imaginary part Ω represents the frequency of oscillation. The eigenvalue analysis is conducted for a range of velocities and the variation of the non-dimensional decay rate $\frac{\Gamma}{\omega_\theta}$ and the normalized frequency $\frac{\Omega}{\omega_\theta}$ is plotted against normalized velocity $U/b\omega_\theta$. Figure A.3.1 shows a comparison between the obtained data to the results presented by Hodges and Pierce (2011). The flutter velocity at which the decay rate becomes positive is around 2.168 m/s which is the same as the predicted flutter speed in the reference. The obtained results verify the implemented aerodynamic model.

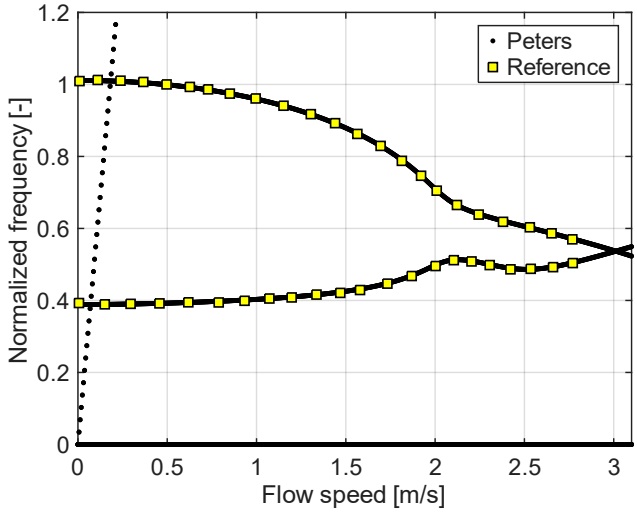

(a)

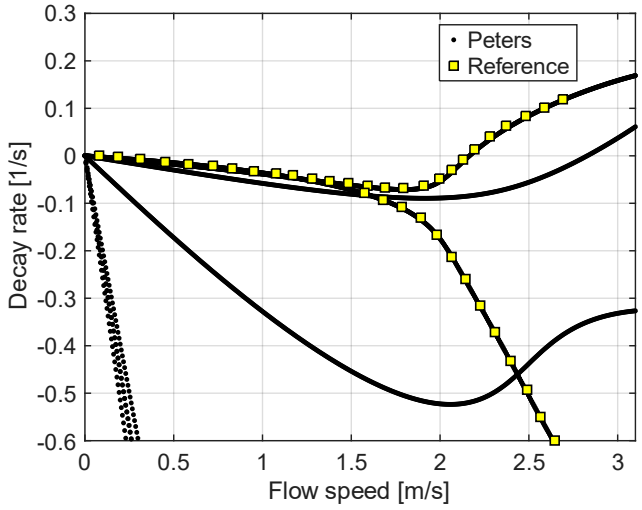

(b)

Figure A.3.1: Modal frequency (a) and decay rate (b) variation with the normalised air flow speed computed for the 2-D airfoil section, comparison to Hodges and Pierce (2011)

IV. Tip loss correction in the strip theory model

The aerodynamic load distribution is corrected using weight factors. These factors are a function of the spanwise position of the load application and a tip loss factor. The weight factor *W* is computed as an exponential function (Riso and Cesnik, 2021) given by:

$$W = 1 - \exp\left[-\tau\left(1 - \frac{s}{l}\right)\right] \tag{A.4.1}$$

where τ is the tip loss factor, *s* is the span-wise position of the reference point, and *l* is the wing span.

The tip loss factor is a function of the root angle of attack α_r and the flow speed *U*. The tip loss factor is computed as:

$$\tau = \tau_0(\alpha_r) + \tau_1(\alpha_r)U + \tau_2(\alpha_r)U^2 \tag{A.4.2}$$

The coefficients τ_0, τ_1, τ_2, which must be individually evaluated for different root angle of attacks, are obtained by tuning their values such that the tip displacements obtained from the 2-D airfoil theory in static aeroelastic analyses match a reference solution. The reference solution can be chosen from a higher fidelity aerodynamics method, which accounts for the 3-D tip effects. The unsteady vortex lattice method (UVLM), which is suitable for large deflection motion and accounts for 3-D effects, is chosen to obtain the reference solution for the present work. The UVLM implementation carried out by Ritter (2019), which is available at the DLR Institute of Aeroelasticity, is utilised to obtain a reference solution.

To discuss the tip loss correction procedure, as an example, the root angle of attack $\alpha_r = 5^0$ is chosen and linear static aeroelastic

analyses are performed for three flow speeds U = 10 m/s, 30 m/s and 50 m/s. The aeroelastic analysis must be conducted in a manner that accounts for the inter-dependency of aerodynamic loads and structural deformations. From Eq. 5.1, it can be seen that in a static loading condition, the local angle of attack is impacted by the pitch angle and wing twist, which is reflected in variations in aerodynamic loading. Since this change is continuous over a load-deflection trajectory until an equilibrium is reached, aerodynamic loads must be adapted accordingly. This can be done using two approaches: (1) the aerodynamic stiffness is appended to the structural stiffness and the aerodynamic forces are computed based on the initial angle of attack of the undeformed wing, or (2) the aerodynamic forces directly take into account the variations in the angle of attack due to the structural deformations while the left-hand side of the equation of motion only comprises the structural stiffness. The first method is used since it involves a single-step computation, while the second approach requires an iterative process to obtain convergence in loads and displacements.

Considering Eqs. 5.2 and 5.3, the coefficients of the terms corresponding to h and θ are utilised to formulate the aerodynamic stiffness matrix in the aerodynamic coordinate system. For j^{th} airfoil section, the aerodynamic stiffness $\boldsymbol{k}_{\boldsymbol{aero}}^{\boldsymbol{j}}$ can be thus expressed as:

$$\boldsymbol{k}_{\boldsymbol{aero}}^{\boldsymbol{j}} = \begin{bmatrix} 0 & 2\pi\rho bU^2 \\ 0 & -2\pi\rho U^2 b^2 \left(\frac{1}{2} + a\right) \end{bmatrix} \tag{A.4.3}$$

The sectional aerodynamic stiffness is multiplied by the strip length in the spanwise direction and is assembled into a global aerodynamic stiffness matrix, where the number of non-zero terms depends on the number of

strips considered in the strip theory model. Additionally, these terms are multiplied by the weight factors *W* since they are essentially components of the lift and moment and also affected by the unaccounted 3D effects. The aerodynamic stiffness is then appended to the structural stiffness with coordinate transformation to obtain an effective aeroelastic stiffness.

Table A.4.1: Comparison of tip displacements obtained from the strip theory model without tip loss correction and from UVLM

Flow speed [m/s]	**Strip theory** **No tip loss correction** **Tip displacement** [m]	**UVLM** **Tip displacement** [m]
10	9.2×10^{-3}	6.1×10^{-3}
30	9.72×10^{-2}	6.17×10^{-2}
50	0.4021	0.2062

In the first step, the weight factors are not considered in the strip theory model, and a uniform load distribution is assumed to compute the wing deformation. A similar analysis of the same structure is conducted using the UVLM tool to obtain the reference solution. Table 5.1 shows a comparison of the tip displacements obtained with the two aerodynamic models.

A considerable difference can be seen in the results obtained from the UVLM and strip theory models when the tip loss correction is not considered, as shown in Table A.4.1. Next, the weight factors are applied in the strip theory model, and the value of τ is iteratively adjusted until the tip displacements obtained are similar to the reference results. The same procedure is followed for all three flow speeds. Referring to Eq. 5.16, we

thus obtain three equations with the three unknown coefficients τ_0, τ_1, and τ_2. In this particular example the values of the coefficients are obtained as: $\tau_0 = 4.7897, \tau_1 = 0.0333$, and $\tau_2 = -7.74 \times 10^{-4}$. Note that these values are specific to the root angle of attack $\alpha_r = 5^0$. If a different angle of attack is chosen the entire procedure must be repeated to obtain new tuning coefficients.

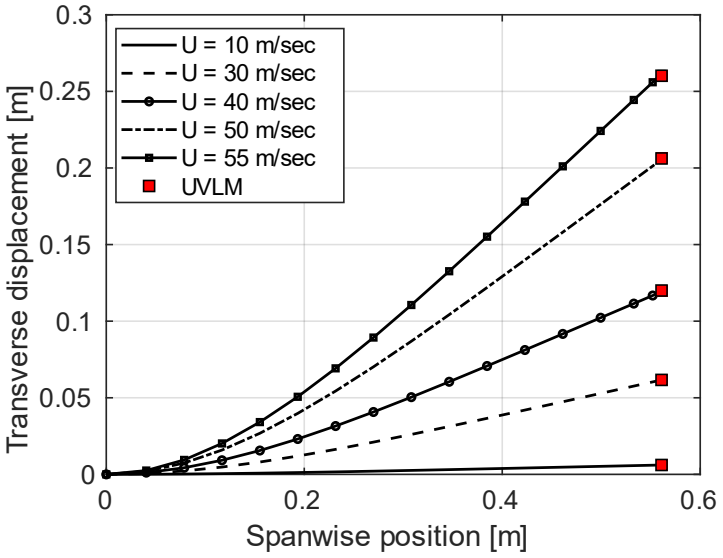

Figure A.4.1: Comparison of transverse tip displacements obtained from the strip theory model considering tip loss correction with respect to reference UVLM results for $\alpha_r = 5^0$

Figure 5.4 shows the transverse displacements obtained from the strip theory model after weight factors are applied. As observed, the tip displacements are well matched with the reference UVLM results. In addition to the three conditions chosen for computing weight factors, additional results are obtained for U = 40 m/s and U = 55 m/s. The tip displacements for these cases show a maximum error of 0.42 % in

comparison to the reference UVLM results even though the flow speed in the second case lies outside the range of solutions to which the tuning coefficients have been fitted. However, increasing flow speeds beyond 55 m/s also progressively increases the error with respect to the reference UVLM solution. Thus, the correction method is suitable within the range of the reference conditions used to obtain the tuning coefficients.

V. Matrix assembly for flutter analysis of 3D wing

The flutter analysis is conducted by transforming the coupled aeroelastic system to the form of a first-order differential equation $\boldsymbol{A\dot{q}} = \boldsymbol{Bq}$ which comprises the structural and aerodynamic state variables $[\boldsymbol{u}\ \dot{\boldsymbol{u}}\ \boldsymbol{\lambda}]'$ and *u* consists of the translation and rotation DOFs of the FE model. For the description of the matrices, it is assumed that the FE model has *n* DOFs and the *N* aerodynamic states are considered from the Peters aerodynamics model for all coupling points in total. For simplicity in the description, the matrices $\boldsymbol{A}$ and $\boldsymbol{B}$, which are of size (2*n*+*N)* x (2*n*+*N),* are subdivided as follows:

$$\boldsymbol{A} = \begin{bmatrix} \boldsymbol{A_1} & \boldsymbol{A_2} & \boldsymbol{A_3} \\ \boldsymbol{A_4} & \boldsymbol{A_5} & \boldsymbol{A_6} \\ \boldsymbol{A_7} & \boldsymbol{A_8} & \boldsymbol{A_9} \end{bmatrix} \tag{A.5.1}$$

$$\boldsymbol{B} = \begin{bmatrix} \boldsymbol{B_1} & \boldsymbol{B_2} & \boldsymbol{B_3} \\ \boldsymbol{B_4} & \boldsymbol{B_5} & \boldsymbol{B_6} \\ \boldsymbol{B_7} & \boldsymbol{B_8} & \boldsymbol{B_9} \end{bmatrix} \tag{A.5.2}$$

$$\boldsymbol{A_1} = \boldsymbol{I_n}, \qquad \boldsymbol{A_2} = null(n,n), \qquad \boldsymbol{A_3} = null(n,N) \tag{A.5.3}$$

where $\boldsymbol{I_n}$ is an identity matrix of size *n* x *n*.

$$\boldsymbol{A_4} = null(n,n), \qquad \boldsymbol{A_5} = \boldsymbol{M_e}, \qquad \boldsymbol{A_6} = null(n,N) \tag{A.5.4}$$

$\boldsymbol{A_7}$, $\boldsymbol{A_8}$ and $\boldsymbol{A_9}$ contain terms corresponding to the induced flow from the aerodynamics model. $\boldsymbol{A_7}$ and $\boldsymbol{A_8}$ are sparse matrices of size *N* x *n,* where the non-zero terms correspond to the DOFs of the coupling points and $\boldsymbol{A_9}$ has a size *N* x *N*. Considering *id1* to be the DOFs for the plunge motion at the coupling point and *id2* to be the DOFs for twist motion at the coupling points, the following relations are established for each coupling point:

$$\boldsymbol{A_7}(:, id2) = -U\bar{\boldsymbol{c}} \tag{A.5.5}$$

$$\boldsymbol{A_8}(:, id1) = \bar{\boldsymbol{c}} \tag{A.5.6}$$

$$\boldsymbol{A_8}(:, id2) = -b(0.5 - a)\bar{\boldsymbol{c}} \tag{A.5.7}$$

$$\boldsymbol{A_9}(:, 1{:}N) = \bar{\boldsymbol{A}} \tag{A.5.8}$$

$$\boldsymbol{B_1} = null(n,n), \qquad \boldsymbol{B_2} = \boldsymbol{I_n}, \qquad \boldsymbol{B_3} = null(n,N) \tag{A.5.9}$$

$$\boldsymbol{B_4} = -\boldsymbol{K_e}, \qquad \boldsymbol{B_5} = -\boldsymbol{D_e} \tag{A.5.10}$$

The sub-matrix $\boldsymbol{B_6}$ consists of the terms related to the induced velocity in the lift and moment expressions, which are defined for each coupling point as:

$$\boldsymbol{B_6}(id1, :) = -\pi\rho U b\bar{\boldsymbol{b}} \tag{A.5.11}$$

$$\boldsymbol{B_6}(id2,:) = -\pi\rho U b^2 \overline{\boldsymbol{b}}\,(0.5+a) \tag{A.5.12}$$

$$\boldsymbol{B_7} = null(N,n), \qquad \boldsymbol{B_8} = null(N,n) \tag{A.5.13}$$

$$\boldsymbol{B_9} = -\frac{U}{b}\boldsymbol{I}_N \tag{A.5.14}$$

VI. Influence of the choice of eigenmodes on the LCO simulations

It is discussed in the Section 5.4.3, that without the inclusion of the third eigenmode (1st torsion mode) of the Pazy wing in the model reduction basis, the LCO response cannot be captured. The results presented in Fig. A.6.1 show that when third eigenmode is excluded in the ROM construction process, regardless of the addition of further eigenmodes, the LCO response cannot captured. Results of three analyses are presented where the structural ROM was constructed to be 4, 7, and 11-DOF models, however, without the inclusion of the third eigenmode. Since the instability in the aeroelastic system is related to the third eigenmode, its absence in the ROM construction process results in an aeroelastic model that always returns to its stable equilibrium position after a perturbation is applied.

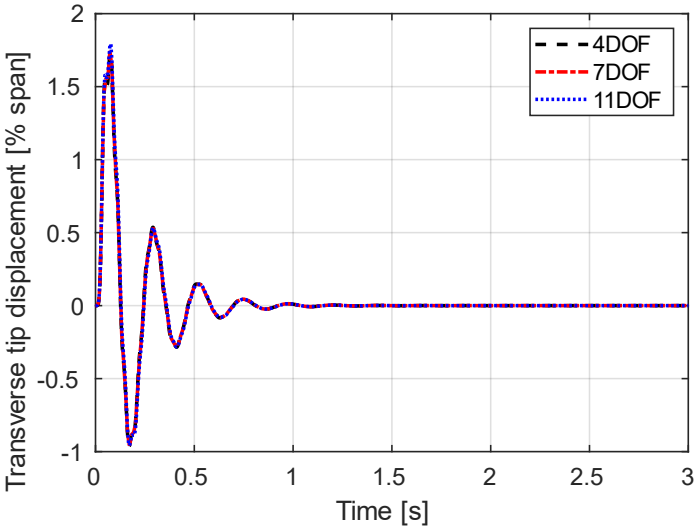

Figure A.6.1: Comparison of time domain aeroelastic response of the Pazy wing to gust perturbation for structural models with various DOFs (constructed without consideration of the third eigenmode)

Curriculum Vitae

Kautuk SINHA

27-01-1990 Born in Jamshedpur, India

EDUCATION

2020-2026 Ph.D. Candidate
Delft University of Technology
Delft, the Netherlands

Thesis: A reduced-order nonlinear aeroelastic framework for wings undergoing large deflections

Promotors: Prof. dr. ir. R. De Breuker
Dr. F. Alijani

2015-2017 Master of Science in Aerospace Engineering
Delft University of Technology
Delft, the Netherlands

2009-2013 Bachelor of Education in Mechanical Engineering
Manipal Institute of Technology
Manipal, India

WORK EXPERIENCE

2018 – now Researcher
German Aerospace Centre
Institute of Aeroelasticity
Göttingen, Germany

List of Publications

Journals

- Sinha, K., Alijani, F., Krüger, W. R., & De Breuker, R. A reduced-order nonlinear dynamic aeroelastic formulation for post-flutter analysis of wings undergoing large deflections. (*under preparation*)

- Sinha, K., Alijani, F., Krüger, W. R., & De Breuker, R. (2025). Nonlinear dynamics of wing-like structures using a momentum subspace-based Koiter-Newton reduction. *Journal of Sound and Vibration*, *596*, 118747.

- Sinha, K., Alijani, F., Krüger, W. R., & De Breuker, R. (2023). Koiter–Newton based model reduction for large deflection analysis of wing structures. *AIAA Journal*, *61*(8), 3608-3617.

Conferences

- Sinha, K., Alijani, F., Krüger, W. R., & De Breuker, R. (2025). Efficient Nonlinear Dynamic Analyses of Aircraft Structural Components with Various Boundary Conditions Using the Koiter-Newton Model Reduction. In *AIAA SciTech 2025 Forum* (p. 0420).

- Sinha, K., Alijani, F., Krüger, W. R., & De Breuker, R. (2024). Nonlinear dynamic response of a Pazy wing variant using the Koiter-Newton model reduction. In *International Forum on Aeroelasticity and Structural Dynamics 2024.*